



AFRL-AFOSR-VA-TR-2016-0309

Predictive simulation of material failure using peridynamics-
advanced constitutive modeling, verification, and validation

Harry Millwater
University of Texas at San Antonio
One Utsa Circle
San Antonio, TX 78249-1130

08/31/2016
Final Report

<p>DISTRIBUTION A: Distribution approved for public release.</p>

Air Force Research Laboratory
AF Office Of Scientific Research (AFOSR)/RTA1

REPORT DOCUMENTATION PAGE				<i>Form Approved</i> <i>OMB No. 0704-0188</i>	
<p>The public reporting burden for this collection of information is estimated to average 1 hour per response, including the time for reviewing instructions, searching existing data sources, gathering and maintaining the data needed, and completing and reviewing the collection of information. Send comments regarding this burden estimate or any other aspect of this collection of information, including suggestions for reducing the burden, to the Department of Defense, Executive Service Directorate (0704-0188). Respondents should be aware that notwithstanding any other provision of law, no person shall be subject to any penalty for failing to comply with a collection of information if it does not display a currently valid OMB control number.</p> <p>PLEASE DO NOT RETURN YOUR FORM TO THE ABOVE ORGANIZATION.</p>					
1. REPORT DATE (DD-MM-YYYY)		2. REPORT TYPE		3. DATES COVERED (From - To)	
4. TITLE AND SUBTITLE				5a. CONTRACT NUMBER	
				5b. GRANT NUMBER	
				5c. PROGRAM ELEMENT NUMBER	
6. AUTHOR(S)				5d. PROJECT NUMBER	
				5e. TASK NUMBER	
				5f. WORK UNIT NUMBER	
7. PERFORMING ORGANIZATION NAME(S) AND ADDRESS(ES)				8. PERFORMING ORGANIZATION REPORT NUMBER	
9. SPONSORING/MONITORING AGENCY NAME(S) AND ADDRESS(ES)				10. SPONSOR/MONITOR'S ACRONYM(S)	
				11. SPONSOR/MONITOR'S REPORT NUMBER(S)	
12. DISTRIBUTION/AVAILABILITY STATEMENT					
13. SUPPLEMENTARY NOTES					
14. ABSTRACT					
15. SUBJECT TERMS					
16. SECURITY CLASSIFICATION OF:			17. LIMITATION OF ABSTRACT	18. NUMBER OF PAGES	19a. NAME OF RESPONSIBLE PERSON
a. REPORT	b. ABSTRACT	c. THIS PAGE			19b. TELEPHONE NUMBER (Include area code)

INSTRUCTIONS FOR COMPLETING SF 298

1. REPORT DATE. Full publication date, including day, month, if available. Must cite at least the year and be Year 2000 compliant, e.g. 30-06-1998; xx-06-1998; xx-xx-1998.

2. REPORT TYPE. State the type of report, such as final, technical, interim, memorandum, master's thesis, progress, quarterly, research, special, group study, etc.

3. DATES COVERED. Indicate the time during which the work was performed and the report was written, e.g., Jun 1997 - Jun 1998; 1-10 Jun 1996; May - Nov 1998; Nov 1998.

4. TITLE. Enter title and subtitle with volume number and part number, if applicable. On classified documents, enter the title classification in parentheses.

5a. CONTRACT NUMBER. Enter all contract numbers as they appear in the report, e.g. F33615-86-C-5169.

5b. GRANT NUMBER. Enter all grant numbers as they appear in the report, e.g. AFOSR-82-1234.

5c. PROGRAM ELEMENT NUMBER. Enter all program element numbers as they appear in the report, e.g. 61101A.

5d. PROJECT NUMBER. Enter all project numbers as they appear in the report, e.g. 1F665702D1257; ILIR.

5e. TASK NUMBER. Enter all task numbers as they appear in the report, e.g. 05; RF0330201; T4112.

5f. WORK UNIT NUMBER. Enter all work unit numbers as they appear in the report, e.g. 001; AFAPL30480105.

6. AUTHOR(S). Enter name(s) of person(s) responsible for writing the report, performing the research, or credited with the content of the report. The form of entry is the last name, first name, middle initial, and additional qualifiers separated by commas, e.g. Smith, Richard, J, Jr.

7. PERFORMING ORGANIZATION NAME(S) AND ADDRESS(ES). Self-explanatory.

8. PERFORMING ORGANIZATION REPORT NUMBER. Enter all unique alphanumeric report numbers assigned by the performing organization, e.g. BRL-1234; AFWL-TR-85-4017-Vol-21-PT-2.

9. SPONSORING/MONITORING AGENCY NAME(S) AND ADDRESS(ES). Enter the name and address of the organization(s) financially responsible for and monitoring the work.

10. SPONSOR/MONITOR'S ACRONYM(S). Enter, if available, e.g. BRL, ARDEC, NADC.

11. SPONSOR/MONITOR'S REPORT NUMBER(S). Enter report number as assigned by the sponsoring/monitoring agency, if available, e.g. BRL-TR-829; -215.

12. DISTRIBUTION/AVAILABILITY STATEMENT. Use agency-mandated availability statements to indicate the public availability or distribution limitations of the report. If additional limitations/ restrictions or special markings are indicated, follow agency authorization procedures, e.g. RD/FRD, PROPIN, ITAR, etc. Include copyright information.

13. SUPPLEMENTARY NOTES. Enter information not included elsewhere such as: prepared in cooperation with; translation of; report supersedes; old edition number, etc.

14. ABSTRACT. A brief (approximately 200 words) factual summary of the most significant information.

15. SUBJECT TERMS. Key words or phrases identifying major concepts in the report.

16. SECURITY CLASSIFICATION. Enter security classification in accordance with security classification regulations, e.g. U, C, S, etc. If this form contains classified information, stamp classification level on the top and bottom of this page.

17. LIMITATION OF ABSTRACT. This block must be completed to assign a distribution limitation to the abstract. Enter UU (Unclassified Unlimited) or SAR (Same as Report). An entry in this block is necessary if the abstract is to be limited.

Predictive simulation of material failure using peridynamics-advanced constitutive modeling, verification, and validation

John T. Foster and James O'Grady

March 31, 2016

Abstract

Peridynamics is a nonlocal formulation of continuum mechanics in which forces are calculated as integral functions of displacement fields rather than spatial derivatives. The peridynamic model has major advantages over classical continuum mechanics when displacements are discontinuous, such as in the case of material failure. While multiple peridynamic material models capture the behavior of solid materials, not all structures are conveniently analyzed as solids. Finite Element Analysis often uses 1D and 2D elements to model thin features that would otherwise require a great number of 3D elements, but peridynamic thin features remain underdeveloped despite great interest in the engineering community. This work develops nonordinary state-based peridynamic models for the simulation of thin features. Beginning from an example nonordinary state-based model, lower dimensional peridynamic models of plates, beams, and shells are developed and validated against classical models. These peridynamic models are extended to incorporate brittle and plastic material failure, compounding the peridynamic advantages of discontinuity handling with the computational simplicity of reduced-dimension features. These models will allow peridynamic modeling of complex structures such as aircraft skin that may experience damage from internal forces or external impacts.

TABLE OF CONTENTS

Acknowledgements	iv
Abstract	v
List of Tables	ix
List of Figures	x
Chapter 1: Introduction	1
1.1 Scope	1
1.2 Outline	2
Chapter 2: Literature Review	3
2.1 PDE-Based Failure Modeling	3
2.2 Peridynamic Modeling	9
2.3 Other Nonlocal Elasticity Models	13
2.4 Thin Features	14
2.4.1 Peridynamic Models	15
Chapter 3: Classical Background	18
3.1 Euler-Bernoulli Beam Theory	18
3.2 Kirchhoff-Love Plate Theory	21
Chapter 4: Peridynamics Background	24
4.1 Peridynamic States	24
4.2 State-based Models	25
4.3 Bond-based peridynamics	28
4.4 Important Peridynamic Models	29

4.4.1	Bond-based Elastic Solid	29
4.4.2	State-based Elastic Solid	32
4.4.3	Correspondence Models	33
Chapter 5:	Model Development	36
5.1	Bond Pair Material Model	36
5.2	Bond Pair Beam in Bending	37
5.2.1	Energy Equivalence	37
5.2.2	Relation to Eringen Nonlocality	39
5.2.3	Weighting function and inelasticity	41
5.3	Bond Pair Plate in Bending	45
5.3.1	Energy Equivalence	45
5.3.2	Combining Bending and Extension Models	48
5.4	Extension to arbitrary Poisson ratio	50
Chapter 6:	Numerical Simulation	53
6.1	Discretized Bond Pair Beam	54
6.2	Discretized Bond Pair Plate	55
6.3	Numerical Model Extensions	57
6.3.1	Curved Shapes	57
6.3.2	Irregular Discretization	58
6.3.3	Extended Discretization	62
6.4	“Boundary” Conditions	63
6.5	Numerical Solution Method	65
6.6	Results	67
6.6.1	Straight Beam Results	67
6.6.2	Flat Plate Results	75
6.6.3	Irregular Discretization Results	82

6.6.4 Curved Surface Results	85
Chapter 7: Conclusion	88
Appendix A: Fréchet Derivative	91
A.1 Definition	91
A.2 Bond-Pair Force	91
A.3 Isotropic Bending Correction	92
Appendix B: Notation	94
Bibliography	98
Vita	

LIST OF TABLES

Table 3.1	Common Beam End Conditions	21
Table 4.1	Common State Operation Nomenclature	25
Table 4.2	Peridynamic Equivalents of Classical Concepts	28
Table B.1	Peridynamic Notation	94
Table B.1	Continued	95
Table B.1	Continued	96
Table B.1	Continued	97

LIST OF FIGURES

Figure 2.1	XFEM includes discontinuous enrichment basis functions	4
Figure 2.2	XFEM models enrich nodes around a discontinuity	5
Figure 2.3	Comparison of domains of influence for FEM and RKPM	6
Figure 2.4	A peridynamic body Ω	10
Figure 2.5	Peridynamic model of an airplane impacting a concrete structure	11
Figure 2.6	Silling's illustration of course-graining in time	12
Figure 2.7	Tearing a peridynamic membrane	15
Figure 2.8	A peridynamic cylinder uses several nodes through its thickness	16
Figure 2.9	Taylor and Steigmann plate transverse displacement	17
Figure 2.10	Taylor and Steigmann plate cracking	17
Figure 3.1	Infinitesimal Beam Slice	19
Figure 3.2	Small deformation in an Euler beam	19
Figure 4.1	Deformation tensor vs. deformation vector state	24
Figure 4.2	The body Ω deformed by the deformation state $\underline{\mathbf{Y}}$	26
Figure 4.3	Illustration of the three types of peridynamic models	27
Figure 4.4	Bond-based models can describe a variety of material behaviors	29
Figure 5.1	Illustration of a bond pair model that resists angular deformation	36
Figure 5.2	Deformation and force vector states	36
Figure 5.3	A continuous peridynamic beam with horizon δ	37
Figure 5.4	Euler beam moment contribution	42
Figure 5.5	Bond-pair moment contribution	42
Figure 5.6	Weight function for a beam of rectangular cross-section	43
Figure 5.7	Weight function for an I-beam	44

Figure 5.8	Illustration of a bond pair on a plate.	46
Figure 5.9	The Hybrid Model Combines Bending and Extension Components	49
Figure 5.10	Bending Deformation Decomposed into Isotropic and Deviatoric Portions	51
Figure 6.1	Translating Continuum Peridynamics to a Discrete Domain	53
Figure 6.2	Discretized peridynamic plate with illustrated bond pair	56
Figure 6.3	Virtual Points Allow Straight Pairs on Curved Surfaces	57
Figure 6.4	Virtual Points Take the Displacement of Nearby Real Points	57
Figure 6.5	Virtual Points Pair Up Unpaired Neighbors	58
Figure 6.6	Barycentric interpolation is based on the relative areas of sub triangles	60
Figure 6.7	Barycentric estimate and error for plane interpolation	61
Figure 6.8	Barycentric estimate and error for quadratic surface	61
Figure 6.9	Barycentric estimate improves with denser discretization	62
Figure 6.10	The boundary of a peridynamic model is a region of nonzero thickness	63
Figure 6.11	The uniform-load elastic beam is accurately modeled with few nodes	67
Figure 6.12	Simply Supported Beam with Point Load	68
Figure 6.13	Simply Supported Beam with Point Moment at Center	68
Figure 6.14	The clamped condition requires finer discretization	69
Figure 6.15	The clamped condition requires a smaller horizon	70
Figure 6.16	Uniformly Loaded Cantilever Beam	70
Figure 6.17	The elastic perfectly-plastic beam requires finer discretization	71
Figure 6.18	The need for fine discretization is even more apparent when representing residual plastic deformation	72
Figure 6.19	Accurately modeling residual plastic deformation also requires a small hori- zon	73
Figure 6.20	A brittle beam with prescribed center displacement	74
Figure 6.21	The Bond-Pair Model Converges on Accurate Plate Deflection with Smaller Horizons	76

Figure 6.22	Horizon Must Include Sufficient Nodes	77
Figure 6.23	The Bond-Pair Model Converges on Accurate Plate Deflection with Finer Discretization	78
Figure 6.24	The Combined Model Accurately Captures the Influence of In-Plane Tension	78
Figure 6.25	The Extended Model Matches for Arbitrary Poisson's Ratio	79
Figure 6.26	Simple Double Torsion Setup	79
Figure 6.27	Crack Progression in Double Torsion Brittle Plate	80
Figure 6.28	Crack Progression in Single Torsion Brittle Plate	81
Figure 6.29	Irregular Beam	82
Figure 6.30	Regular Plate Discretization	83
Figure 6.31	Irregular Plate Discretization	83
Figure 6.32	Virtual Points Allow for Irregular Discretizations	84
Figure 6.33	Proving Ring Setup	85
Figure 6.34	A Beam-based Proving Ring in Varying Discretizations	86
Figure 6.35	Horizon Convergence in the Beam-based Proving Ring	86
Figure 6.36	Discretization of a 3D Proving Ring	87
Figure 6.37	Plate-based Proving Ring	87

Chapter 1: INTRODUCTION

The final goal of many mechanical engineering analyses is the prediction and description of material failure. Even when some amount of material failure is acceptable, conservative engineering models can indicate safe conditions by which failure may be avoided. Within these operation envelopes, a wide variety of well-developed analysis techniques are available to predict material behavior. Outside the envelope, the onset of failure may be predicted and replacement/repair indicated, but the actual progression of material failure is unknown. Because these envelopes conservatively restrict operation, absolute avoidance of material failure may require tradeoffs such as: reduced operational life, expensive inspection and repair regimes, increased down-time, and reduced performance in other areas. Material models that accurately predict failure progression can extend the operational envelope without reducing reliability. Other problems, such as those related to impact, penetration, and blast resistance, necessarily involve material failure and cannot be accurately modeled without simulating failure progression. Without reliable means for modeling failure progression, these problems can be tackled only by means of extensive (and expensive) testing programs. While some extrapolation from test results is possible, many conditions of interest are difficult, expensive, and/or dangerous to create and to observe. For these reasons, accurate and reliable models for the progression of failure for various materials and conditions has long been and remains a major focus of engineering research.

1.1 Scope

This dissertation presents a nonlocal equivalent to an Euler-Bernoulli beam, along with a methodology for representing non-uniform cross-sections, plastic behavior, and failure. Unlike many continuum beam theories that derive new equations of motion (such as fourth order PDE's) from the three-dimensional elastic constitutive model, or even introduce new equations of motion without reference to any solid constitutive model, the new model is not derived from prior ordinary peridynamic models based on bond extension, but is a material model that directly resists bending defor-

mation while maintaining the same conservation of momentum equation as the three-dimensional model. In other words, bending is a fundamental mode of deformation to this model, which resists it at the constitutive level. This beam model is demonstrated to be equivalent to Eringen's nonlocal elasticity for small peridynamic horizons.

The one-dimensional beam model is then extended to two dimensions to model the bending behavior of flat Kirchhoff-Love plates. The resulting 1-parameter model is constrained to a Poisson ratio $\nu = 1/3$. By introducing an *isotropic bending-state*, the model is extended to any valid Poisson ratio. The model is combined with an extension-based model to capture the effect of in-plane forces on bending behavior, resulting in a flat shell model that is easily discretized to model simple shapes. Introducing the concept of virtual points results in a discretized model that is more practically applicable and able to model non-uniform distributions of peridynamic points, as might result from a meshing software. Using virtual points also allows the simulation of curved shells, greatly expanding the class of problems that can be approached with this model. Because many analyses of interest are partly or wholly comprised of these types of features, their development is an important addition to the capabilities of peridynamic analysis.

1.2 Outline

Chapter 2 of this dissertation reviews the literature for material modeling, focussing on the most prominent PDE-based material failure modeling techniques, alternative nonlocal models, peridynamics, and thin feature modeling. Chapter 3 gives a short background on Euler beams and Kirchhoff plates. Chapter 4 provides necessary background information on peridynamic models. Chapter 5 develops the new bond-pair and bond-multiple peridynamic bending models. Chapter 6 translates the continuum model into a useful discrete form and extends that discrete model to handle curved and irregular shapes. The results of these discrete models are compared to analytical and classical solutions for simple models in section 6.6. Conclusions and avenues for future development are laid out in chapter 7.

Chapter 2: LITERATURE REVIEW

2.1 PDE-Based Failure Modeling

Because material failure is an important part of many problems, there are several computational methods that attempt to simulate progressing material failure. Most of these methods start with the partial differential equations for conservation of momentum found in classical continuum mechanics, then extend those models to account for failure situations that are poorly modeled by the classical equations.

One of the most popular is the eXtended Finite Element Method (XFEM), an excellent overview of which can be found in [28] by Fries and Belytschko. Traditional finite elements use polynomial basis functions to describe unknown fields over an element. As a result, fields such as displacement always vary continuously across an element; discontinuities within an element are poorly approximated even by high-order polynomials. When they are allowed at all, discontinuities can only arise between elements, and are therefore very mesh-dependent; worse, to model a moving or evolving discontinuity requires continual remeshing around the advancing crack tip, adding greatly to the computational complexity of the problem. The finite elements in an XFEM model are “extended” or enriched by adding basis functions that are discontinuous or that are continuous but have discontinuous derivatives. In the case of crack growth, this extension comes in the form of discontinuous basis functions that reflect the discontinuous displacement field at a crack. In 1982, Arnold [2] developed a mathematical basis for using discontinuous finite elements and an interior penalty method. This method allows modeling problems with very high gradients (as at boundaries) and greatly reduces the importance of meshing and the need for remeshing. While initially demonstrated for high-gradient heat and fluid flow problems, the method of adding discontinuities within an element had strong potential for failure problems resulting in discontinuous displacements. Instead of remeshing along an expected crack path, a process that would require continual remeshing, the predicted direction of crack growth is used to choose discontinuous basis functions

consistent with a crack along that path.

The use of discontinuous basis functions (such as fig. 2.1) to model crack progression through an element was first developed by Belytschko and Black in [6] to model straight and gently curving cracks with less remeshing. The discontinuous function in fig. 2.1 will look familiar. As the transverse displacement field around the tip of a Mode I crack,

$$v(x, y) = \frac{K_I}{2\mu} \sqrt{\frac{r}{2\mu}} \cos\left(\frac{\theta}{2}\right) \left[\kappa - 1 + 2 \sin^2\left(\frac{\theta}{2}\right) \right], \quad (2.1)$$

eq. (2.1) and the other crack-tip displacement fields are a natural choice of basis functions. Longer cracks would require remeshing, but at the root of the crack rather than the tip. Root remeshing represents a major improvement over tip remeshing because it needs to be performed far less frequently. Additionally, the path of the advancing crack can travel at any angle rather than following the angle of a mesh edge. The practice was then extended by Moës et al. in [49] to use different

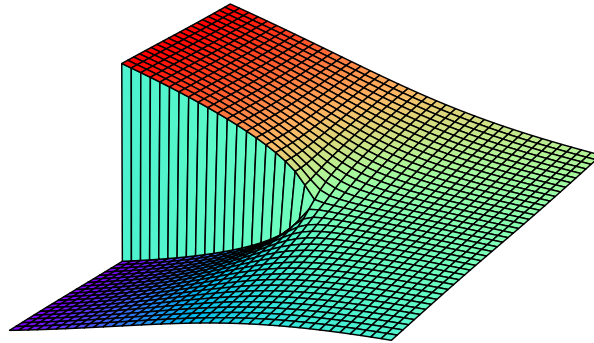


Figure 2.1: XFEM includes discontinuous enrichment basis functions

discontinuous basis functions for cracks and crack tips. Adding a Haar function to model discontinuous displacements far from the crack tip allowed cracks to pass through several elements, enabling the modeling of cracks with greater length and curvature without remeshing.

As with traditional finite element methods, XFEM is mesh-based and uses traditional finite element basis functions. The elements are enriched extrinsically by adding discontinuous basis functions to the existing basis functions using the Partition of Unity concept described by Melenk and Babuška in [44]. The enrichment functions can capture arbitrary discontinuities in both the parameter being modeled and in its gradient, but the location of the discontinuities must be predicted so that the appropriate enrichment functions can be used. In [49], crack direction was predicted by locating the maximum circumferential stress. There are other options for predicting a crack's direction of travel, but they do not generally predict the formation of a crack where none existed before. Elements are enriched locally as illustrated in fig. 2.2 rather than globally, to capture local phenomena like crack growth. In some elements, every node is enriched, while in others, only some nodes are enriched. Some choices of enrichment functions cause difficulties in the partially enriched “blending” elements, a problem for which a variety of fixes are available depending on the situation.

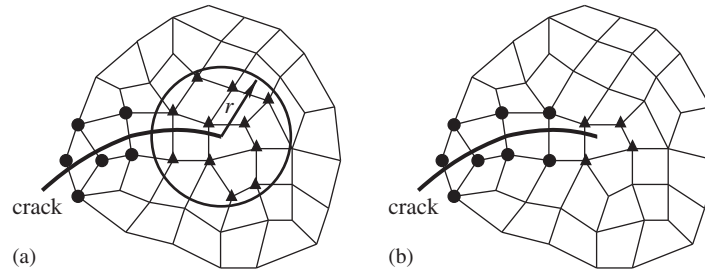


Figure 2.2: XFEM models enrich nodes around a discontinuity [28]

More recently, Sauerland and Fries applied XFEM to two phase flow problems [62], including standard dam-breaking and rising droplet problems. Holl et al. [32] used XFEM in the multi scale modeling of crack propagation, including multiple interacting cracks. Mohammadnejad and Khoei [50] and Hunsweck et al. [33] modeled using XFEM the combination of fluid and fracture behavior found in hydraulic fracturing, a topic of considerable recent interest.

A second common method of modeling material failure is the Reproducing Kernel Particle Method (RKPM), developed by Liu et al. [40]. Mesh-based models track the connections between

points in a deforming material, which can become problematic when large deformations deform the mesh and even cause it to intersect itself. RKPM is a “mesh-free” method that tracks material properties by their values at selected points. Mesh-free methods are advantageous for modeling large deformation in fluids and solids because they do not track connections between points. Between material points, properties are interpolated from their values at nearby points by way of integration with a kernel function. The difference in domains between RKPM and XFEM can be seen in fig. 2.3. The key to the RKPM lies in this kernel function; by using window functions from wavelet

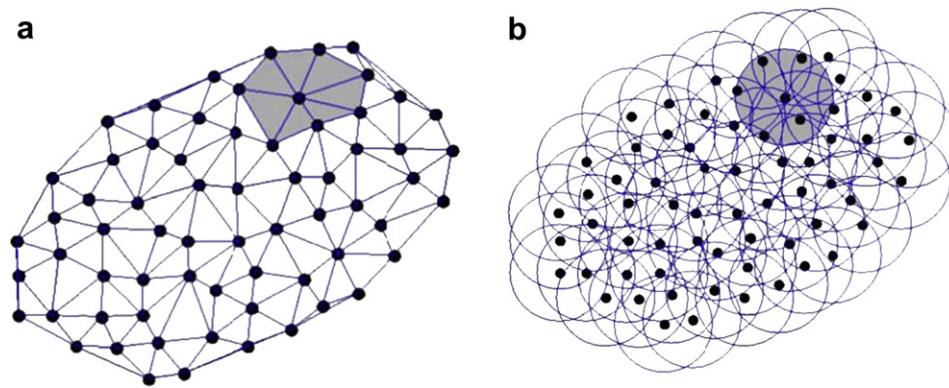


Figure 2.3: Comparison of domains of influence for a)FEM and b)RKPM, by Guan et al. [31]

analysis, a “reproducing” kernel guarantees that integrals of interpolated properties reproduce the integral of the continuous property field. The “reproducing” kernel makes the RKPM a Partition of Unity method like XFEM, and is a major advantage of RKPM relative to other particle methods. It is computationally expensive to perform the necessary shape-function integration, however. The integration is typically performed on a background grid, raising concern over whether it is truly “mesh-free”.

In its original formulation, the RKPM successfully handles large deformations that would cause unacceptable distortion in Finite Element models. A semi-Lagrangian version implemented by Guan et al. in [30] allows for recalculation of the support function. This allows damage in the form of severing the relationship between points that have been pulled too far apart. Recent applications of the RKPM include the work of Guan et al. on fragment-impact problems [31] and analysis of non-linear wave equations by Cheng and Kim Meow [13]. The RKPM has also been used by Xie

and Wang [82] to analyze coupled hydro-mechanical behavior. Wu et al. have coupled RKPM and FEM in their recent work on fragmentation and debris evolution [81].

Other methods of modeling failure include multiple finite element techniques and particle methods. Finite element methods incorporating “element death” remove from consideration elements that meet particular criteria and are perhaps the simplest way of modeling material failure.

Cohesive zone elements, proposed by Ortiz et al. [56], use element level information to detect the onset of plasticity (material instability) and add suitable deformation modes to model shear banding. The additional deformation modes allow cohesive zone elements to capture the more complex displacements associated with plastic shear bands. Other cohesive zone elements developed by Needleman [53] model crack growth, but Foulk et al. [27] note that this requires very fine meshes or prior knowledge of the crack path. They are useful for cases such as composite delamination or debonding, where the crack follows a known surface. Fang et al. propose in [23] a method of augmenting the cohesive zone model to work in concert with XFEM-type elements to model both arbitrary and known crack paths. More recently, McGarry et al. [43] and Máirtín et al. [41] developed a cohesive zone model to account for crack closure, including crack surface tractions.

Particle methods of modeling failure include the Smooth Particle Hydrodynamic (SPH) method, reviewed by Monaghan in [51], in which a kernel (commonly a cubic spline) is used to create a smooth interpolation of actual quantities. Unlike the wavelet basis functions of RKPM, which can be made to reproduce a polynomial field of any order, cubic splines only perfectly reproduce constant fields. Developed for fluids, Springel notes in [71] that it is often used in astrophysics problems, where many fluid problems are encountered and even “solid” bodies deform under their own gravity. It can also predict elastic behavior and has been extended with failure models by Benz and Asphaug in [7] by adding an evolving damage parameter. Particle methods like SPH handle fragmentation very well, and are used in a variety of problems with material interfaces, high strains, and multiphase and multi-physics aspects. Because cubic spline kernels do not reproduce a Partition of Unity, property interpolation does not accurately reproduce the continuum

field. Additionally, elastic SPH models do not conserve angular momentum, and in cases require artificial viscosities or artificial stresses to avoid numerical instability.

The Material Point Method, developed by Sulsky and Schreyer in [72], tracks points in both Eulerian and Lagrangian meshes. The advantage of using both meshes is an ability to handle obstacles and boundary conditions without difficulty at large deformations. Wieckowski notes that the downside to using both meshes is continual remeshing and added computational expense [80]. Despite this expense, the material point method was extended to model cracks by Nairn in [52], then further enhanced by Sadeghirad et al. in [60] to improve stability when modeling massive deformations. The Lattice Discrete Particle Method was developed by Cusatis et al. [14, 15] to model concrete. Unlike perviously mentioned particle methods, the particles in LDPM represent actual particles of aggregate and the cement between them, with volume as well as mass. It fills a volume with variously-sized particles generated from a probability density function based on aggregate size. The relationships between these particles form tetrahedrons (the lattice) that fill the volume and allow multi-particle interaction. As with finite element models, displacement between particle centers is linearized to compute strains, stresses, and forces. Failure occurs at predefined surfaces between particles and can include various failure modes. The LDPM is capable of accurately modeling many failure conditions in concrete, including the impact of specimen size on effective material behavior. These are only a few of the myriad of models that attempt to model the progression of material failure.

All of these methods are used to solve a partial differential equation for conservation of momentum in a continuum. Because they are based on continuum PDEs, they do not naturally develop discontinuous displacements such as cracks. The PDEs that govern these methods are ill-defined at the surface of a crack, so cracks must be inserted within or between elements after discretization. This results in crack propagation that is discretization-dependent as well as computationally expensive and potentially unstable. Although progress in addressing these issues continues, much of the difficulty is essentially tied to the undefined nature of derivative equations at discontinuous displacements. By abandoning the use of displacement derivatives, peridynamics offers an alternative

way to address discontinuous displacements.

2.2 Peridynamic Modeling

The term *peridynamic* was coined by Silling to describe the new formulation of continuum mechanics he developed in [64]. From the Greek roots *peri* and *dyna* meaning *near* and *force* respectively, it alludes to the nonlocal force exerted by nearby points. In contrast to the nonlocal continuum mechanics models of Kröner, Eringen and Edelen [21, 22, 36], which formulate behavior as an integral function of strain (itself a spatial derivative of displacement), the peridynamic model casts material behavior at a point as an *integral equation of the surrounding displacement* rather than the classical *differential* equation. Because peridynamic models do not include spatial displacement derivatives, discontinuous displacements can arise naturally and can be analyzed without first discretizing the problem or applying special heuristics. In classical continuum mechanics, linear momentum is conserved according to the local eq. (2.2),

$$\rho(\mathbf{x})\ddot{\mathbf{u}}(\mathbf{x}) = \nabla \cdot \mathbf{P}(\mathbf{x}) + \mathbf{b}(\mathbf{x}) , \quad (2.2)$$

in which ρ is the density, $\ddot{\mathbf{u}}$ is the second time derivative of displacement, \mathbf{P} is the transpose of the First Piola Kirchhoff stress tensor, and \mathbf{b} is the body force density, all of which are functions of position \mathbf{x} and of time. Because \mathbf{P} is defined in terms of the deformation gradient, it is clear that eq. (2.2) is undefined for discontinuous displacements. In fact, traditional models require even the first spatial derivative of displacement to be continuous. Strongly nonlocal models (including peridynamics) replace the divergence-of-stress term with an integral functional,

$$\rho(\mathbf{x})\ddot{\mathbf{u}}(\mathbf{x}) = \int_{\Omega} \mathbf{f}(\mathbf{x}, \mathbf{q}) dV_{\mathbf{q}} + \mathbf{b}(\mathbf{x}) , \quad (2.3)$$

so that, instead of the divergence of stress, we have the integral of a “force” function \mathbf{f} of the position vector \mathbf{x} and the position vector \mathbf{q} of a point within the body domain Ω . This force

function may depend on \mathbf{x} , \mathbf{q} , their deformed positions, the original and deformed positions of other points in Ω , history, etc. It is common for \mathbf{f} to be defined as 0 for any pair of points initially further than δ apart. The points within δ of a point \mathbf{x} are the *neighborhood* of \mathbf{x} and are denoted in fig. 2.4 by \mathcal{H} . By including the behavior of nearby material, these models introduce an inherent

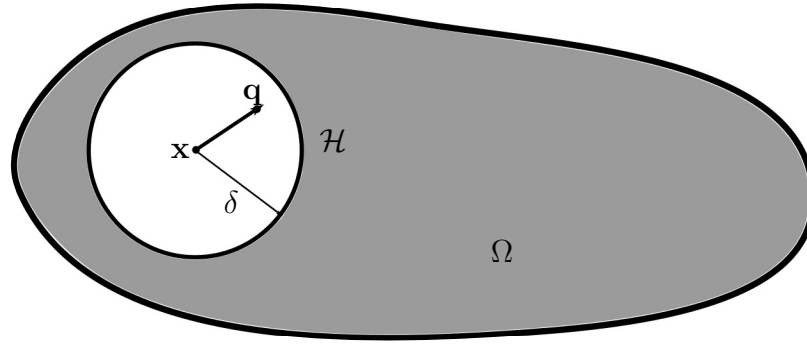


Figure 2.4: A peridynamic body Ω

length scale to the model. This length scale is theoretically determined by material properties, though choice of length scale is sometimes limited by computational demands.

Constitutive modeling of a wide variety of materials is accomplished by choosing the appropriate form for the force function. The form of the simplest such function is a peridynamic “bond” between two points that is modeled by a pairwise force function. While the simplest force functions recreate a one-parameter linear elastic solid material, other force functions can be used to model a wide variety of material behaviors, some of which will be outlined here. Most simulation of material behavior uses an equation of motion reformulated for a discretized model. The typical discretization is a mesh-free numerical method in which there are no geometrical connectivities between various nodes.

A force function can be restricted to being pairwise (depending solely on the displacement of the two points \mathbf{x} and \mathbf{q}), and still model complex and varied behavior. By including a damage parameter that sets the force contribution of “damaged” bonds to 0, Silling and Askari [68] were able to model a brittle material with natural crack formation, propagation, and branching. Other examples of damage propagation include impacts against brittle structures as in fig. 2.5 modeled by Demmie and Silling [17] and fracturing of thermally-stressed glass modeled by Kilic

and Madenci [35]. Modeling progressive fracture, including crack branching, is a major advantage

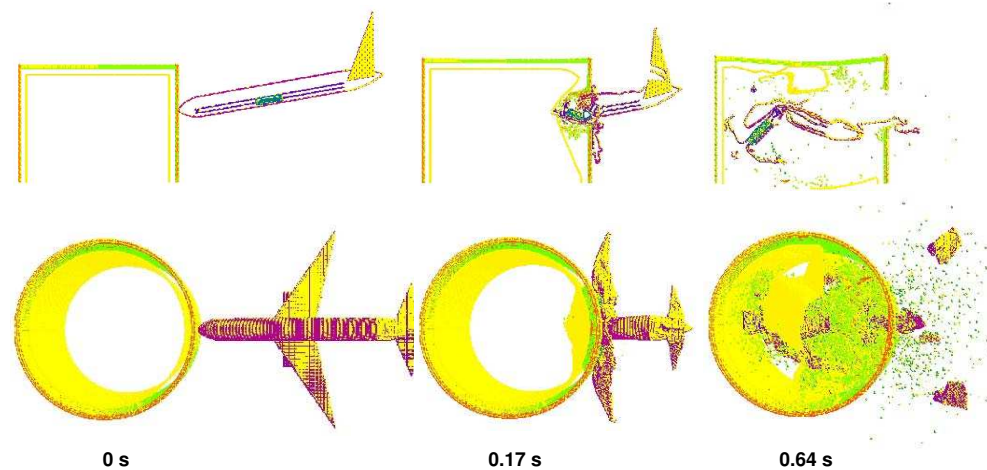


Figure 2.5: Peridynamic model of an airplane impacting a concrete structure [17]

of peridynamic formulations. Using a piecewise force function, Dayal and Bhattacharya [16] were able to model phase transformation in 1D and 2D without an additional constitutive law; the transformations arose and propagated naturally as a dynamic instability, a result of the force function used. Peridynamic models have also been used to analyze composite laminates. In [83], Xu et al. designate peridynamic bonds as fiber or matrix bonds with different force functions to model damage in composite laminates. Kilic et al. model fiber, matrix, and interfacial bonds in [34] to capture stacking order effects on damage propagation. Bobaru [8] applied the peridynamic model to nano fiber networks, at a scale where long-range forces are very apparent. In the same paper he created a Representative Volume Element (RVE) for random networks of nano fibers, laying the ground work for peridynamic multi-scale modeling. Also related to multi-scale peridynamic modeling is work by Silling on model coarsening [65], fig. 2.6. An example of a multi-scale peridynamic simulation can be found in [3], by Askari et al.

Concrete is a nearly standard example material in which nonlocal behavior is easily observed, and modeling the damage accumulation and proceeding discontinuity propagation has long been the goal of nonlocal models developed by Bažant and Pijaudier-Cabot [5] among others, significantly predating peridynamics. In [29], Gerstle et al. use rotational degrees of freedom to create a concrete material model, capable of describing a linear elastic material with any Poisson ratio,

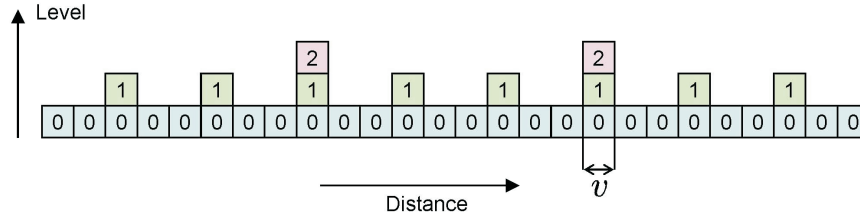


Figure 2.6: Silling's illustration of course-graining in time from [65].

that also handles material failure. Peridynamic models are not limited to force-displacement relationships; the theory has also been applied to diffusion processes and multiphysics problems. Peridynamic models can simulate heat transfer [9] and diffusion [10].

Mathematical analyses of simplified cases have also been fruitful. Weckner [78] determined analytical solutions to the infinite bar problem. Emmerlick and Zimmerman proved solution existence and uniqueness in the simplest case of the peridynamic bar [20]. Mikata found additional analytical solutions for the bar problem [46]. In 3D, Weckner constructed Green's functions for an infinite peridynamic solid in [79]. All of this work was done with peridynamic models limited to pairwise force functions.

Other than Gerstle's aforementioned micropolar peridynamic model, the pairwise force function limits 3D solid materials to a Poisson ratio of $\nu = 1/4$. To model additional material behavior, Silling et al. generalized the underlying peridynamic concept of bonds and forces and introduced state-based peridynamic models in [66]. By freeing the force function from the pairwise restriction, state-based models allow the force relationship between two points to depend on the collective behavior of all nearby material. Using the concept of a deformation vector-state allows for the construction of correspondence models that can recreate any classical constitutive model. These correspondence models use the deformation state to approximate the deformation gradient tensor, then use the deformation gradient tensor to calculate force contributions. State-based models were used by Foster et al. to simulate viscoplasticity and hardening in [26], and rate dependent failure in [25], with others, via an energy criterion. Mitchell describes state-based models for plasticity in [47] and viscoelasticity in [48]. A non-ordinary state-based model was used by Warren et al. to simulate fracture in [77]. More recently, Tupek et al. have incorporated the idea of peridynamic

damage into a Johnson-Cook based damage state that accumulates with plastic strain [75].

2.3 Other Nonlocal Elasticity Models

The peridynamic formulation of continuum mechanics is neither the only nor the first nonlocal model. Nonlocal elasticity generally allows for forces at a point that are dependent on the material configuration of an entire body, rather than the configuration at that point [22]. While long-range forces are obvious at the molecular model, material at larger scales is conventionally modeled as though internal forces are local or contact forces [36]. The result of such approximation is accurate for deformations that are homogeneous, but introduces some inaccuracy for inhomogeneous deformations like the propagation of waves with short wavelengths. One way to distinguish between homogeneous and inhomogeneous deformations is to incorporate higher-order gradients of deformation. While stress in classical elasticity is a function of the (first) gradient of deformation, Eringen's formulation of a nonlocal modulus in [21] approximates a weighted sum of the first and second order gradients. This introduces a length scale to the model and has the effect of smearing out local deformation inhomogeneities over the surrounding material, while maintaining the conventional result for homogeneous deformations.

Previous work in the nonlocal mechanics of beams is motivated by the observed stiffening of nanoscale cantilevers. Challamel and Wang demonstrate in [12] that Eringen nonlocal elasticity cannot reproduce the scale stiffening, but that stiffening does result from other gradient-elastic models and models incorporating nonlocal curvature. Because all of these models incorporate higher-order gradients of deformation, they impose stronger continuity requirements than classical elasticity, and are unsuitable for discontinuous displacements. Because the gradients are evaluated locally, gradient models are called *weakly nonlocal*. Recent work by Paolo et al. [57] develops a displacement-based beam in which relative axial displacement, shear displacement, and rotation of non-adjacent beam segments are resisted by three kinds of nonlocal spring, whose stiffnesses can be tuned to the expected material behavior. With the appropriate nonlocal stiffnesses, their model reproduces the nanoscale cantilever stiffening effect.

Similarly, Duan and Wang [19] applied Eringen-type elasticity to the quasi-1D problem of axisymmetric bending in nanoscale plates. Pradhan and Murmu [58] extended the concept to buckling in single-layered graphed sheets, a fully 2D problem. Later, Ansari et al. [1] modeled the vibration of single-layered graphed sheets using Eringen-type elasticity.

Nonlocal effects have also been incorporated into many of the modeling techniques previously discussed. Bažant and Chang incorporated nonlocal strain-softening into a finite element model in [4]. Any interpolating particle method will exhibit some measure of nonlocality, but some explicitly model nonlocal phenomena. Vignjevic et al. used SPH to model nonlocal strain-softening in [76], and in [11], Burghardt et al. developed a material point method that incorporates nonlocal plasticity.

2.4 Thin Features

Many engineering analyses concern shapes that have one dimension much greater than another; numerical modeling the behavior of these shapes can be a considerable challenge for methods designed for 3D solids. In finite element models, for example, calculations can become unstable or too stiff when individual elements become long and thin. To avoid such elements while maintaining model fidelity requires a very large number of solid elements. By making some assumptions about the behavior along the thin direction, many such shapes can be modeled as 1D beams or 2D plates or shells without great loss of accuracy. A comprehensive review of the classical continuum mechanics associated with thin features by Reddy [59] also includes a section on the finite element analysis of plates and shells. Material failure in classical thin features is modeled using the same techniques as in solids. Dolbow et al. use XFEM in [18] to model fracture in plates. Li et al. use a variant of RKPM in [37] to model plastic deformation in shells. More recently, Xu et al. have applied XFEM to plate plasticity problems [84], and Memar Ardestani et al. have used RKPM to model functionally graded plates [45]. Other authors use cohesive zone elements [38] or SPH [42] to study failure in thin features.

2.4.1 Peridynamic Models

Reduced dimension thin features such as bars [20,46,69,78], plates [35], and membranes [70] have been modeled using peridynamics, but these models are used for in-plane or membrane forces as shown in fig. 2.7. Because traditional peridynamic models exert forces in the direction of the bonds

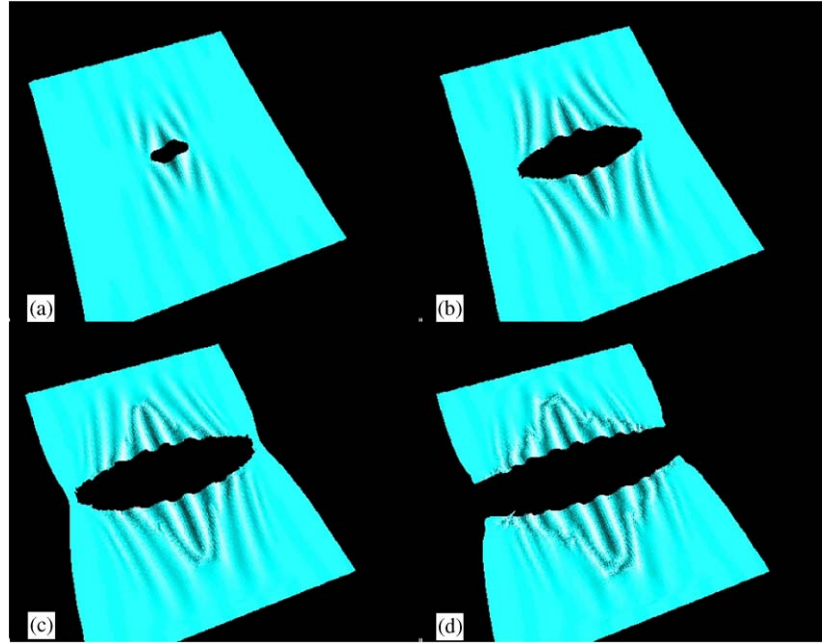


Figure 2.7: Tearing a peridynamic membrane [70]

between points, they are not well-suited for bending problems of thin shapes, in which force and displacement are both nearly perpendicular to bonds connecting material points at separate points on a surface. Just as with solid finite elements, most peridynamic models of thin features like the tubes in fig. 2.8 have included several nodes through the thickness of a thin part to capture bending behavior. Also as with solid finite elements, this leads to very fine discretization of thin features, even when the expected behavior is quite simple. This greatly increases the computational expense of modeling parts with thin features.

A recent paper by Taylor and Steigmann [73] partially addresses this issue by starting with mathematical analysis of the continuous 3D bond-based peridynamic solid model of a thin plate. By using a continuous model, they avoid the difficulties associated with discretizing thin fea-

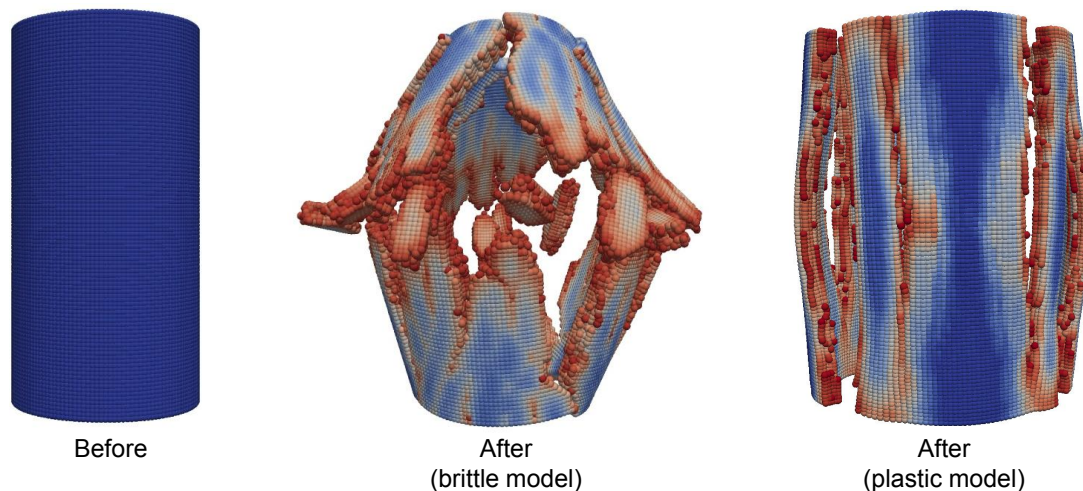


Figure 2.8: A peridynamic cylinder uses several nodes through its thickness in [39]

tures. Applying asymptotic analysis to the continuous model, they reduce a 3D solid model to 2 dimensions. The asymptotic reduction is accomplished by the addition of degrees of freedom for the derivative of displacement with respect to the through thickness direction. By making the through-thickness derivative of displacement vector an independent variable, the resulting flat model includes a measure of angular deformation that allows resistance to bending. Using a simple bond-stretch damage criterion, the Taylor and Steigmann's reduced model was able to capture the out-of-plane displacement (fig. 2.9) associated with crack propagation behavior (fig. 2.10) in a pre-cracked plate under tension loading. In general, however, the asymptotic reduction model encounters difficulty when nonlinear behaviors like damage are implemented. The use of a bond-stretch criterion as implemented is only appropriate when deformation is dominated by in-plane tension, as failure caused by bending will not be captured. Because of its basis in the 3D bond-based solid model, Taylor and Steigmann's model is limited to a Poisson's ratio of $\frac{1}{3}$. While it is possible that future analysis will extend the asymptotic reduction to state-based model, allowing for arbitrary Poisson's ratios, there are significant mathematical hurdles that will have to be overcome.

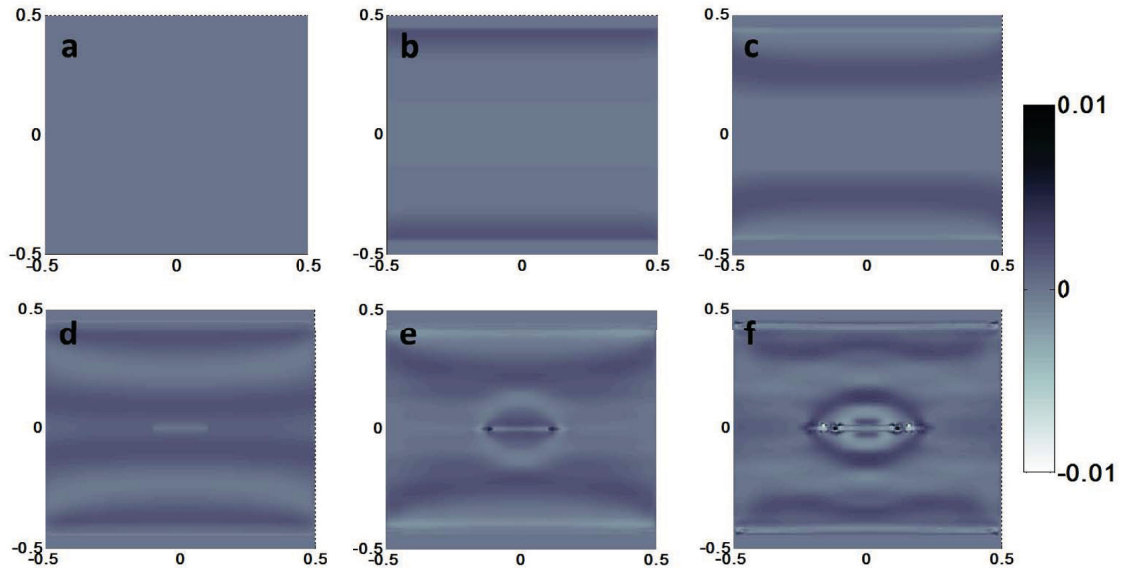


Figure 2.9: Taylor and Steigmann's asymptotic reduction allows for bending resistance in a 2D plate in tension [73]

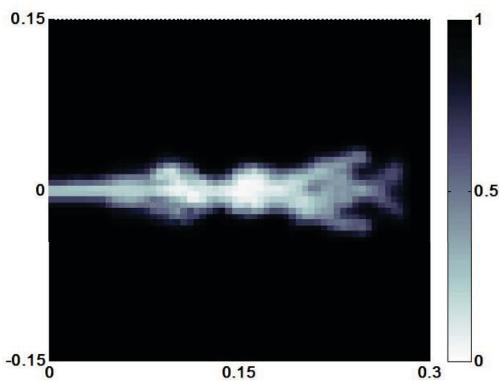


Figure 2.10: Taylor and Steigmann's crack propagation for fig. 2.9 plot f [73]

Chapter 3: CLASSICAL BACKGROUND

3.1 Euler-Bernoulli Beam Theory

The simplest representation of bending behavior is found in the Euler-Bernoulli beam equation,

$$\frac{d^2}{dx^2} \left(EI \frac{d^2 v}{dx^2} \right) = q, \quad (3.1)$$

which describes the transverse deflection of long-slender beams. Equation (3.1) is for a beam in the \hat{x} direction, whose displacement v is perpendicular to \hat{x} and parallel to the distributed load q acting on the beam. While it is only applicable to small deformations and rotations, there are many problems that can be easily and usefully simplified by the application of Euler beams.

It is important to note that eq. (3.1) is not a constitutive equation; it does not relate stress and strain for a material. Instead, it is derived from the constitutive equation for a linearly-elastic material and some assumptions about the deformation. Euler-Bernoulli beam theory is much simpler than a 3D analysis of a beam as a solid material, but it requires the following assumptions to be met:

- Slenderness: the length of the beam should be 20 times its other dimensions
- Loaded transversely, no axial loads or torques
- Small deformations and rotations
- Plane cross-sections of the beam remain plane under deformation
- Initially straight, and symmetric about the plane of bending

First, we take a infinitesimal slice of a beam as depicted in fig. 3.1. Because we will want to compare to this model later, we use a different y -coordinate direction than many presentations. We use this infinitesimal slice to derive the relationship between load, shear, and moment.

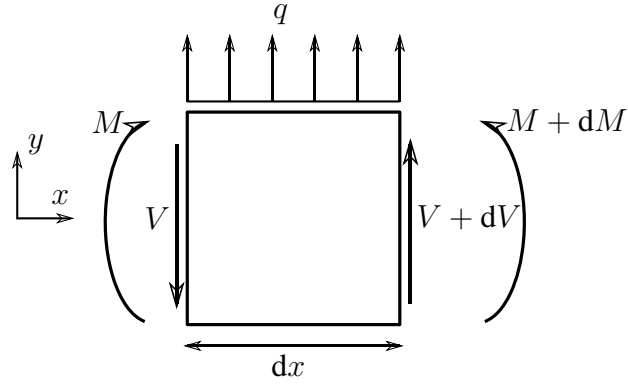


Figure 3.1: Infinitesimal Beam Slice

A force balance demonstrates that the x-derivative of internal shear force is the applied load.

$$V = V + q \, dx + dV \implies \frac{dV}{dx} = -q. \quad (3.2)$$

The moment balance can be performed about any point, but it is simplest to use the right side.

$$M - V \, dx + q \, dx \frac{dx}{2} = M + dM \implies \frac{dM}{dx} = -V + \mathcal{O}(dx). \quad (3.3)$$

Next, we will use the deformation assumptions to frame the bending as a simple arc from which

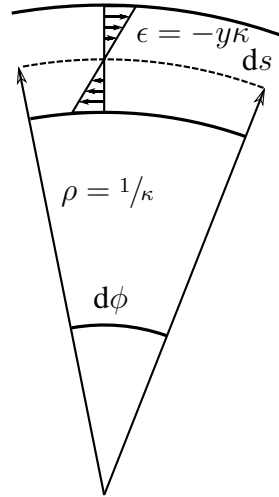


Figure 3.2: Small deformation in an Euler beam

we can deduce a relationship between the transverse displacement of a beam section and its angle

and radius of curvature to be

$$\frac{1}{\rho} \approx \frac{d\phi}{dx} \approx \frac{d^2v}{dx^2} = \kappa. \quad (3.4)$$

The radius of curvature, ρ is the radius of the arc formed by the beam's neutral axis, which does not change in length as the beam bends. We use this same arc to find the strain in material that is at a distance y from the neutral axis. In a linearly elastic material, the resulting stress is proportional to Young's modulus E . To find the bending moment that results from that stress profile, we integrate the moment contribution through the beam.

$$M_{\text{resisted}} = \int_{\text{bottom}}^{\text{top}} y\sigma dA = \int_{\text{bottom}}^{\text{top}} y^2 E\kappa dA. \quad (3.5)$$

In equilibrium, the moment resisted will be equal and opposite to the moment applied

$$\kappa = \frac{M_{\text{applied}}}{E \int_{\text{bottom}}^{\text{top}} y^2 dA}. \quad (3.6)$$

The integral in the denominator is the bending resistance of the beam's shape, called its second moment of area, about the neutral axis. The second moment of area is generally represented by I . By combining eqs. (3.2) to (3.4) and (3.6), we reproduce eq. (3.1), the Euler-Bernoulli beam equation. If the Young's modulus and beam cross section are constant throughout the beam, the equation can be further simplified to

$$EI \frac{d^4v}{dx^4} = q.$$

Obviously, to solve for the deformed position we will require 4 constraints from boundary conditions. The nature of the constraints is determined by the support configuration. The most common end conditions are listed table 3.1. Other end constraints, such

Table 3.1: Common Beam End Conditions

End Condition	Constraint 1	Constraint 2
End Load	$v''' = \pm F$	$v'' = 0$
End Torque	$v''' = 0$	$v'' = \pm \tau$
Simply Supported	$v'' = 0$	$v = v_{\text{support}}$
Clamped	$v' = v'_{\text{clamp}}$	$v = v_{\text{clamp}}$

3.2 Kirchhoff-Love Plate Theory

Like Euler-Bernoulli beam theory, Kirchhoff-Love Plate theory begins by making simplifying assumptions about the plate and its deformation.

- Slenderness: the length and width of the plate should be 20 times its thickness
- Loaded transversely, no in-plane loads or torques
- Small deformations and rotations
- Straight lines normal to the plate remain normal to the center plane of the plate under deformation
- Initially flat

These assumptions allow us to simplify our strain-displacement relationships and formulate our curvatures and strains in terms of the transverse displacement w ;

$$\kappa_x = \frac{\partial^2 w}{\partial x^2}, \quad \kappa_y = \frac{\partial^2 w}{\partial y^2}, \quad \kappa_{xy} = \frac{\partial^2 w}{\partial x \partial y},$$

$$\varepsilon_x = -z\kappa_x, \quad \varepsilon_y = -z\kappa_y, \quad \gamma_{xy} = -2z\kappa_{xy}.$$

To find the stresses at any point, we apply Hooke's law and find

$$\begin{aligned}\sigma_x &= -\frac{Ez}{1-\nu^2} (\kappa_x + \nu\kappa_y) , \\ \sigma_y &= -\frac{Ez}{1-\nu^2} (\kappa_y + \nu\kappa_x) , \\ \tau_{xy} &= -\frac{Ez}{1+\nu} \kappa_{xy} .\end{aligned}$$

As with the beam, these stresses can be integrated over the thickness of the plate to determine the resulting moments.

$$\begin{aligned}M_x &= \int_{-t/2}^{t/2} z\sigma_x dz = -D (\kappa_x + \nu\kappa_y) , \\ M_y &= \int_{-t/2}^{t/2} z\sigma_y dz = -D (\kappa_y + \nu\kappa_x) , \\ M_{xy} &= \int_{-t/2}^{t/2} z\tau_{xy} dz = -D (1-\nu) \kappa_{xy} ,\end{aligned}$$

with

$$D = \frac{Et^3}{12(1-\nu^2)}$$

as the flexural rigidity. Note that a beam of unit width would have a second moment of area $I = \frac{t^3}{12}$, so the flexural rigidity of a plate is greater by a factor of $\frac{1}{1-\nu^2}$. The difference between the values reflects the fact that, when a plate is bent in one direction, poisson ratio effects promote curvature in the opposite direction at a right angle. Constraining this saddle-shaped (or *anticlastic*) bending increases the stiffness or rigidity of the plate.

Constructing the governing equation is more complicated than for beams because, instead of shear V and moment M on an infinitesimal section, we have shears V_x and V_y and moments M_x , M_y , and M_{xy} . Balancing forces gives us

$$\frac{\partial V_x}{\partial x} + \frac{\partial V_y}{\partial y} = p ,$$

for transverse pressure p . Balancing moments gives

$$\begin{aligned}\text{about } x : \quad & \frac{\partial M_{xy}}{\partial x} + \frac{\partial M_y}{\partial y} - V_y = 0 , \\ \text{about } y : \quad & \frac{\partial M_{xy}}{\partial y} + \frac{\partial M_x}{\partial x} - V_x = 0 .\end{aligned}$$

Combining the force and moment balance equations generates the governing equation

$$\frac{\partial^4 w}{\partial x^4} + 2 \frac{\partial^4 w}{\partial x^2 \partial y^2} + \frac{\partial^4 w}{\partial y^4} = \frac{p}{D} .$$

As with the beam case, we will need to apply boundary conditions in order to find the deformed configuration.

Chapter 4: PERIDYNAMICS BACKGROUND

4.1 Peridynamic States

Introduced by Silling et al. in 2007 [66], peridynamic states are functions of the behavior of the continuum points surrounding each location. As is appropriate for a theory based on force-carrying bonds, states often operate on vectors. The most common states are scalar-states and vector-states which are scalar and vector valued, respectively. As a matter of convention, scalar states are usually denoted by lowercase letters (e.g. a , b), while vector states are denoted by uppercase letters (e.g. \underline{A} , \underline{B}). A state that operates on vectors and is itself vector valued naturally brings to mind a two-point tensor such as the deformation gradient; unlike a second order tensor, which can only map vectors linearly to other vectors, vector-states can produce nonlinear, discontinuous, or even noninvertible mappings. This difference is illustrated in fig. 4.1.

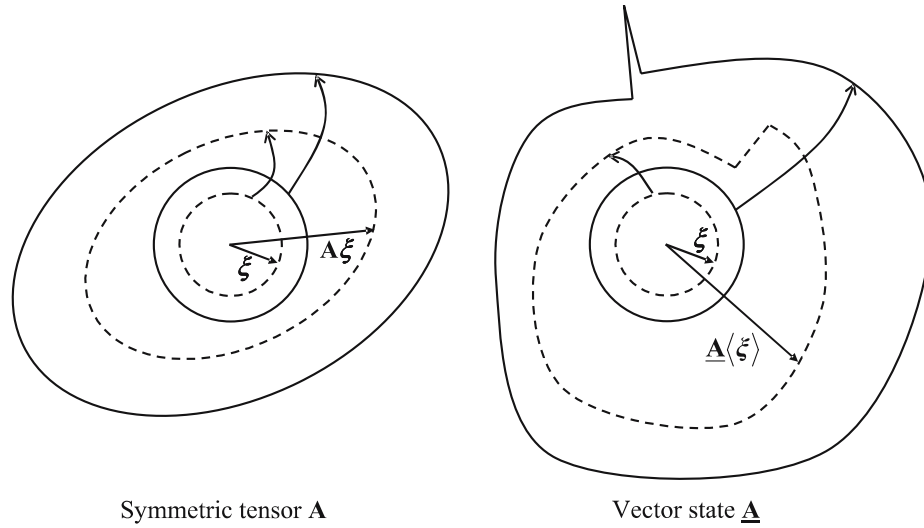


Figure 4.1: The deformation tensor linearly maps spheres to ellipsoids, while a vector state can map spheres nonlinearly to complex and even discontinuous shapes [66]

The mathematical properties of states and several related operators are defined in [66]. Important properties of states are magnitude and direction, while important operations include the addition and composition of states, inner and tensor products, and the Fréchet derivative of a func-

Table 4.1: Common State Operation Nomenclature

Operation	Notation	Meaning
Addition	$(\underline{a} + \underline{b})\langle \xi \rangle$	$\underline{a}\langle \xi \rangle + \underline{b}\langle \xi \rangle$
Multiplication	$(\underline{a} \underline{b})\langle \xi \rangle$	$\underline{a}\langle \xi \rangle \underline{b}\langle \xi \rangle$
Scalar Product	$(\underline{\mathbf{A}} \cdot \underline{\mathbf{B}})\langle \xi \rangle$	$\underline{\mathbf{A}}\langle \xi \rangle \cdot \underline{\mathbf{B}}\langle \xi \rangle$
Composition	$(\underline{\mathbf{A}} \circ \underline{\mathbf{B}})\langle \xi \rangle$	$\underline{\mathbf{A}}\langle \underline{\mathbf{B}}\langle \xi \rangle \rangle$
Dot Product	$\underline{\mathbf{A}} \bullet \underline{\mathbf{B}}$	$\int_{\mathcal{H}} \underline{\mathbf{A}}\langle \xi \rangle \cdot \underline{\mathbf{B}}\langle \xi \rangle$
	$\underline{a} \bullet \underline{b}$	$\int_{\mathcal{H}} \underline{a}\langle \xi \rangle \underline{b}\langle \xi \rangle$
Vector Norm	$ \underline{\mathbf{A}} \langle \xi \rangle$	$ \underline{\mathbf{A}}\langle \xi \rangle $
State Norm	$\ \underline{\mathbf{A}}\ $	$\sqrt{\underline{\mathbf{A}} \bullet \underline{\mathbf{B}}}$
Fréchet Derivative	$\nabla f(\underline{\mathbf{A}})$	$\frac{\partial f}{\partial \underline{\mathbf{A}}}$
	$\Psi(\underline{\mathbf{A}}, \underline{\mathbf{B}})_{\underline{\mathbf{A}}}$	$\frac{\partial \Psi}{\partial \underline{\mathbf{A}}}$

tion with respect to a state. While some of these operations are intuitive, the nomenclature may not be. Refer to table 4.1 for the notation of common state operations. For a more rigorous definition and examples of the Fréchet derivative, see appendix A.

4.2 State-based Models

Conservation of linear momentum in the *state-based* peridynamic formulation results in the equation of motion

$$\rho(\mathbf{x})\ddot{\mathbf{u}}(\mathbf{x}) = \int_{\Omega} (\underline{\mathbf{T}}[\mathbf{x}]\langle \mathbf{q} - \mathbf{x} \rangle - \underline{\mathbf{T}}[\mathbf{q}]\langle \mathbf{x} - \mathbf{q} \rangle) dV_{\mathbf{q}} + \mathbf{b}(\mathbf{x}), \quad (4.1)$$

in which $\underline{\mathbf{T}}[\]\langle \ \rangle$ is a *force vector-state* that maps the vector in angle brackets, $\langle \ \rangle$, originating at the point in square brackets, $[\]$, to a force vector acting on that point. The deformed image of the vector $(\mathbf{q} - \mathbf{x})$ is defined as the *deformation vector-state*, usually denoted $\underline{\mathbf{Y}}$ and formulated

$$\underline{\mathbf{Y}}[\mathbf{x}]\langle \mathbf{q} - \mathbf{x} \rangle = (\mathbf{q} - \mathbf{x}) + (\mathbf{u}(\mathbf{q}) - \mathbf{u}(\mathbf{x})) \quad (4.2)$$

for a displacement field \mathbf{u} . Just as stress and strain are work conjugate, so too are the force and deformation vector states for hyperelastic materials.

State-based models include surrounding material behavior illustrated in fig. 4.2 in the force function between each pair of continuum points. It is common for the formulation of the force state $\underline{\mathbf{T}}$ to be scaled by a weighting function, commonly represented by ω , that makes explicit the region in which the force relationship between points is nonzero. Perhaps the simplest and most common weight function is eq. (5.8), representing a constant nonzero value for bonds shorter than the peridynamic horizon δ .

$$\omega(\boldsymbol{\xi}) = \begin{cases} 1 & \text{if } |\boldsymbol{\xi}| \leq \delta, \\ 0 & \text{if } |\boldsymbol{\xi}| > \delta. \end{cases} \quad (4.3)$$

Many evaluations of forces, energies, and other states at a given point are reduced from being integrals over the entire body to being integrals over that point's neighborhood \mathcal{H} . This is particularly useful when trying to apply peridynamic models to real-world problems, especially when using computer models. If the force state $\underline{\mathbf{T}}$ is always in the same direction as the deformation state

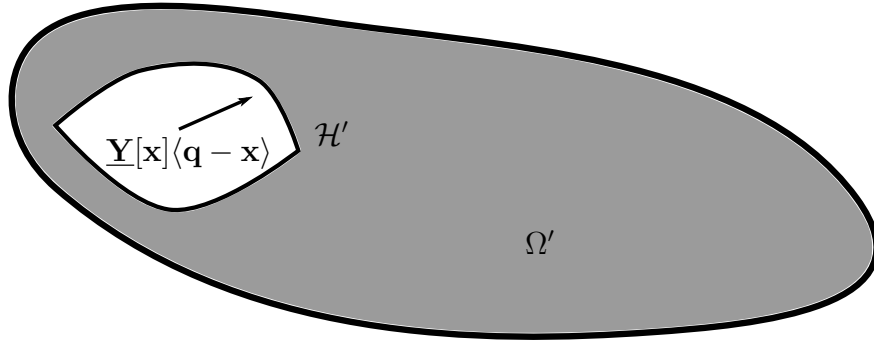


Figure 4.2: The body Ω deformed by the deformation state $\underline{\mathbf{Y}}$

$\underline{\mathbf{Y}}$, then the force exerted by a “bond” between points is in the same direction as the deformed bond, and the model is called *ordinary*. Ordinary state-based models can reproduce linear elastic materials with arbitrary Poisson ratios by separating dilatory and deviatoric deformations and the energy corresponding to each. They can also model a variety of elastic and inelastic behaviors.

There is no requirement that force states be in the same direction as their associated deforma-

tion states, and models in which they are not in the same direction are called *nonordinary*. Some additional care is needed to ensure that angular momentum is conserved in a *nonordinary* state-based model, but they are still perfectly legitimate. Silling et al. demonstrates the possibility of such models in [67], but very little work has touched on their use. Foster et al. [26] and Warren et al. [77] show that some correspondence models, which approximate the deformation gradient and use it to calculate bond forces, result in non-ordinary state-based constitutive models for finite deformations. Bond-based, ordinary state-based, and nonordinary state-based models are illustrated in fig. 4.3.

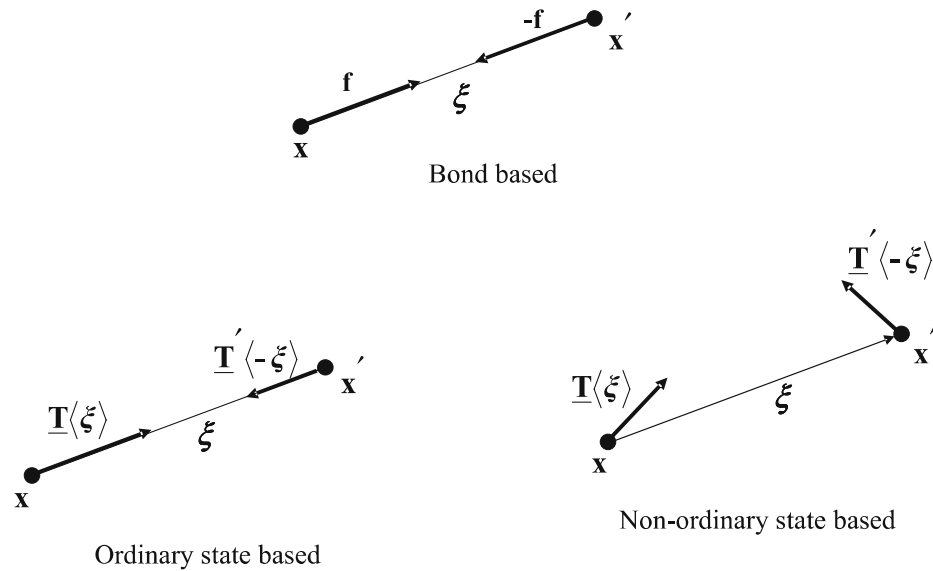


Figure 4.3: Illustration of the three types of peridynamic models, from specific to general [66]

It should be clear that many of the concepts of classical continuum mechanics have direct equivalents in peridynamic modeling. Table 4.2 lays out some of the simplest parallels between classical and peridynamic formulations.

Table 4.2: Peridynamic Equivalents of Classical Concepts

Concept	Classical	Peridynamic
Kinematics	\mathbf{F}	$\underline{\mathbf{Y}}$
Linear Momentum	$\nabla \cdot \boldsymbol{\sigma}$	$\int_{\Omega} (\underline{\mathbf{T}}[\mathbf{x}]\langle \mathbf{q} - \mathbf{x} \rangle - \underline{\mathbf{T}}[\mathbf{q}]\langle \mathbf{x} - \mathbf{q} \rangle) dV_{\mathbf{q}}$
Angular Momentum	$\boldsymbol{\sigma} = \boldsymbol{\sigma}^T$	$\int_{\Omega} \underline{\mathbf{Y}}[\mathbf{x}]\langle \mathbf{q} - \mathbf{x} \rangle \times \underline{\mathbf{T}}[\mathbf{x}]\langle \mathbf{q} - \mathbf{x} \rangle dV_{\mathbf{q}} = 0$
Constitutive Law	$\boldsymbol{\sigma} = \boldsymbol{\sigma}(\boldsymbol{\epsilon})$	$\underline{\mathbf{T}} = \underline{\mathbf{T}}(\underline{\mathbf{Y}})$
Stress Power	$\dot{\boldsymbol{\epsilon}} \boldsymbol{\sigma}$	$\underline{\mathbf{T}} \bullet \dot{\underline{\mathbf{Y}}}$

4.3 Bond-based peridynamics

If the force state $\underline{\mathbf{T}}[\mathbf{x}]\langle \boldsymbol{\xi} \rangle$ depends only on the deformed positions of the points at the end of the bond $\boldsymbol{\xi}$, then the model is called *bond-based*. In *bond-based* peridynamic models, each pair of points is treated separately, without consideration of the behavior of other points. This makes bond-based models much simpler computationally than general state-based models, and reduces the equation of motion to

$$\rho(\mathbf{x})\ddot{\mathbf{u}}(\mathbf{x}) = \int_{\Omega} \mathbf{f}(\mathbf{u}(\mathbf{q}) - \mathbf{u}(\mathbf{x}), \mathbf{q} - \mathbf{x}) dV_{\mathbf{q}} + \mathbf{b}(\mathbf{x}). \quad (4.4)$$

By choosing an appropriate function \mathbf{f} , this model can reproduce the results of linear elasticity for solid materials with a Poisson ration $\nu = 1/4$ and 2-dimensional materials with a Poisson ration $\nu = 1/3$. It can also be used to investigate a range of nonlinear behaviors by changing the force function (examples in fig. 4.4). To conserve momentum in a bond-based model, it is only necessary that \mathbf{f} satisfy

$$\mathbf{f}(\mathbf{u}(\mathbf{q}) - \mathbf{u}(\mathbf{x}), \mathbf{q} - \mathbf{x}) = -\mathbf{f}(\mathbf{u}(\mathbf{x}) - \mathbf{u}(\mathbf{q}), \mathbf{x} - \mathbf{q}), \quad (4.5)$$

i.e. the forces exerted at the opposite ends of the bond between \mathbf{x} and \mathbf{q} must be equal and opposite. The first peridynamic models were all bond-based, and provide useful insight into many complex material failure phenomenon despite their limitations.

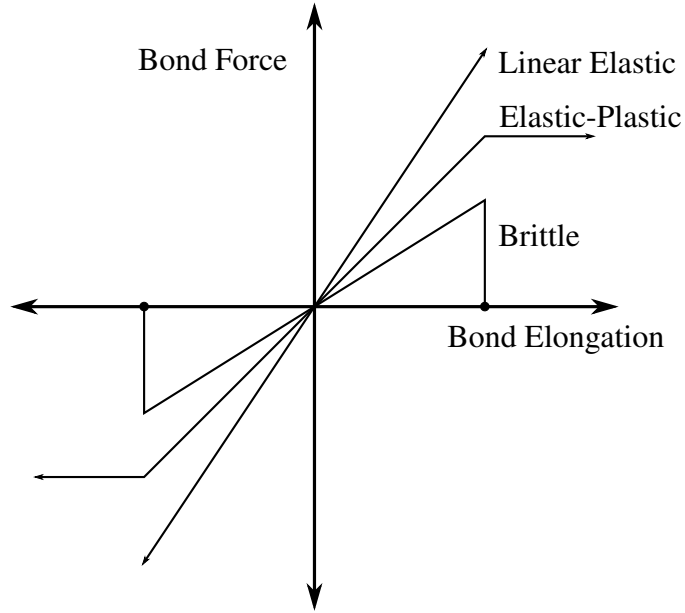


Figure 4.4: Bond-based models can describe a variety of material behaviors

4.4 Important Peridynamic Models

Though they cover only a small portion of the behaviors modeled with peridynamics, these few examples should serve to illustrate the form and analysis of peridynamic material models.

4.4.1 Bond-based Elastic Solid

The simplest peridynamic model treats each bond as a linear spring between two points. In the bond-based formulation, there is no interaction between different bonds, so the force function is

$$\mathbf{f}(\mathbf{u}(\mathbf{q}) - \mathbf{u}(\mathbf{x}), \mathbf{q} - \mathbf{x}) = \omega(|\mathbf{q} - \mathbf{x}|) c s [(\mathbf{q} + \mathbf{u}(\mathbf{q})) - (\mathbf{x} + \mathbf{u}(\mathbf{x}))], \quad (4.6)$$

with weighting function ω , spring constant c , and the stretch s defined by

$$s = |(\mathbf{q} + \mathbf{u}(\mathbf{q})) - (\mathbf{x} + \mathbf{u}(\mathbf{x}))| - |\mathbf{q} - \mathbf{x}|. \quad (4.7)$$

For a deformation gradient \mathbf{F} representing small uniform displacements, i.e. $\nabla \mathbf{u} \ll 1$, the stretch of bond $\boldsymbol{\xi} = \mathbf{q} - \mathbf{x}$ is

$$s = |\mathbf{F}\boldsymbol{\xi}| - |\boldsymbol{\xi}| = \frac{\epsilon_{ij}\xi_i\xi_j}{|\boldsymbol{\xi}|}.$$

For reasons that will become clear in the discussion of the next model, we calibrate the spring constant c following the approach of [66], by comparing the energy to that of a classical solid under purely deviatoric deformation, so that $\epsilon_{ij} = \epsilon_{ij}^d$. The energy of this spring will be in units of energy per volume squared, so that integration over all the springs at a point gives energy per unit volume,

$$\begin{aligned} w &= \frac{c s^2}{2}, \\ W &= \frac{c}{2} \int_{\mathcal{H}} \omega(|\boldsymbol{\xi}|) \left(\frac{\epsilon_{ij}^d \xi_i \xi_j}{|\boldsymbol{\xi}|} \right) \left(\frac{\epsilon_{kl}^d \xi_k \xi_l}{|\boldsymbol{\xi}|} \right) dV_{\boldsymbol{\xi}}, \\ &= \frac{c}{2} \epsilon_{ij}^d \epsilon_{kl}^d \int_{\mathcal{H}} \frac{\omega(|\boldsymbol{\xi}|)}{|\boldsymbol{\xi}|^2} \xi_i \xi_j \xi_k \xi_l. \end{aligned} \quad (4.8)$$

Because ω depends only on $|\boldsymbol{\xi}|$, we can rewrite this integral in spherical coordinates as

$$W = \frac{c}{2} \epsilon_{ij}^d \epsilon_{kl}^d \int_0^\delta \frac{\omega(r)}{r^2} \int_0^{2\pi} \int_0^\pi (\xi_i \xi_j \xi_k \xi_l) r^2 \sin(\phi) d\phi d\theta dr.$$

Recognizing that $\xi_1 = r \sin \phi \cos \theta$, $\xi_2 = r \sin \phi \sin \theta$, $\xi_3 = r \cos \phi$, we can see that configurations of $[i, j, k, l]$ with an odd number of any index result in integrals with an odd number of one or more of $\cos \theta$, $\sin \theta$, $\cos \phi$, and therefor are equal to 0. For the remaining configurations,

$$\int_0^\delta \frac{\omega(r)}{r^2} \int_0^{2\pi} \int_0^\pi (r^4 \sin^4 \phi \cos^2 \theta \sin^2 \theta) r^2 \sin(\phi) d\phi d\theta dr = \frac{4\pi}{15} \int_0^\delta \omega(r) r^4 dr.$$

This leaves only configurations such as $[1, 1, 3, 3]$, $[1, 2, 1, 2]$ and $[3, 2, 2, 3]$, which we can indicate by $(\delta_{ik}\delta_{jl} + \delta_{il}\delta_{jk} + \delta_{ij}\delta_{kl})$. Additionally, any combination with $i = j$ or $k = l$ results in terms ϵ_{ii}^d

or ϵ_{kk}^d . Such terms sum to 0 in deviatoric deformation, leaving only $(\delta_{ik}\delta_{jl} + \delta_{il}\delta_{jk})$.

$$\begin{aligned} W &= \frac{c}{2} \epsilon_{ij}^d \epsilon_{kl}^d \frac{4\pi}{15} \int_0^\delta \omega(r) r^4 dr (\delta_{ik}\delta_{jl} + \delta_{il}\delta_{jk}), \\ &= c \epsilon_{ij}^d \epsilon_{ij}^d \frac{4\pi}{15} \int_0^\delta \omega(r) r^4 dr, \\ &= \frac{c}{15} \epsilon_{ij}^d \epsilon_{ij}^d m. \end{aligned}$$

To force the result to be independent of the horizon δ , we normalize the expression by

$$m = \int_{\mathcal{H}} \omega(|\xi|) |\xi|^2 = 4\pi \int_0^\delta \omega(r) r^4 dr. \quad (4.9)$$

By comparing to the classical strain energy density $\Omega = \mu \epsilon_{ij}^d \epsilon_{ij}^d$ for shear modulus μ , we can determine the appropriate bond stiffness,

$$c = \frac{15}{m} \mu.$$

Applying a purely dilational deformation to the same model is far easier. With dilation θ_{3D} , the stretch of a bond in any direction is

$$s = \frac{\theta_{3D}}{3} r,$$

and the corresponding energy is

$$\begin{aligned} W &= \frac{c}{2} \int_{\mathcal{H}} \omega(|\xi|) \frac{\theta_{3D}^2}{9} r^2 dV_\xi, \\ &= \frac{c}{18} \frac{\theta_{3D}^2}{9} \int_0^\delta \omega(r) \int_0^{2\pi} \int_0^\pi r^2 r^2 \sin(\phi) d\phi d\theta dr, \\ &= \frac{c}{18} \theta_{3D}^2 m, \\ &= \frac{15}{9} \mu \frac{\theta_{3D}^2}{2}. \end{aligned} \quad (4.10)$$

This shows that the model based on bond-stretch has a bulk modulus that is $1/5$ of its shear modulus, indicating a Poisson's ratio of $1/4$.

A nearly identical analysis can be performed on a simpler 2D version of the same model, departing after eq. (4.8). Applying a purely deviatoric in-plane shear to such a model, and comparing the resulting energy to that of a classical plate with thickness t gives us

$$c = \frac{8 \mu t}{m_{2D}}, \quad m_{2D} = \int_{\mathcal{H}_{2D}} \omega(|\boldsymbol{\xi}|) |\boldsymbol{\xi}|^2 dV_{\boldsymbol{\xi}}.$$

Applying a planar dilation deformation to a 2D plate results in strain energy consistent with a Poisson's ratio of $1/3$ rather than the value of $1/4$ found for the 3D solid.

4.4.2 State-based Elastic Solid

The state-based linear isotropic peridynamic solid material model is both important and illustrative. Developed in [66], it uses many of the important characteristics of peridynamic states to model a linearly-elastic material with any valid Poisson's ratio. The extension state \underline{e} is exactly the same as the stretch s in eq. (4.7). Classical material models dealing with metal plasticity often separate deformation into dilation and deviation components. Similarly, the extension state can be decomposed into isotropic and deviatoric extension states. Using m from eq. (4.9) as above for normalization the dilation state is defined

$$\theta_{3D} = \frac{3}{m} \int_{\mathcal{H}} \omega(\boldsymbol{\xi}) |\boldsymbol{\xi}| \underline{e} dV_{\boldsymbol{\xi}}. \quad (4.11)$$

The isotropic and deviatoric extension states are defined in turn

$$\underline{e}^i = \frac{\theta_{3D} |\boldsymbol{\xi}|}{3}, \quad \underline{e}^d = \underline{e} - \underline{e}^i. \quad (4.12)$$

If the energy associated with dilation is set to

$$W^i = \frac{k \theta_{3D}^2}{2},$$

then the corresponding force state is

$$\underline{t} = \frac{3k\theta_{3D}}{m}\omega(\underline{\xi})|\underline{\xi}|.$$

We saw in the analysis of the bond-based model the necessary bond stiffness to match the energy associated with purely deviatoric deformation. The two can be combined for eq. (4.13), a force state that clearly indicates the separate responses to dilation and deviatoric deformation:

$$\underline{t} = \frac{3k\theta_{3D}}{m}\omega(\underline{\xi})|\underline{\xi}| + \frac{15\mu}{m}\omega(\underline{\xi})\underline{e}^d. \quad (4.13)$$

A quick examination shows that, in the case that the dilation θ_{3D} is not constant, the force at either end of a bond will not satisfy eq. (4.5). Thus such a model is not possible in a bond-based framework without significant modification.

4.4.3 Correspondence Models

One way to create a peridynamic material model is to start from a material model in classical dynamics. Classical models based on the deformation gradient have the advantage of decades of development and tens of thousands of hours of testing, and they enjoy widespread use in the continuum mechanics community. Peridynamic *correspondence* models use the relative positions of a points neighbors to determine $\bar{\mathbf{F}}(\underline{\mathbf{Y}})$, a nonlocal approximation of the deformation gradient \mathbf{F} .

$$\bar{\mathbf{F}}(\underline{\mathbf{Y}}) = \left[\int_{\mathcal{H}} \omega(|\underline{\xi}|)(\underline{\mathbf{Y}}\langle\underline{\xi}\rangle \otimes \underline{\xi}) dV_{\underline{\xi}} \right] \mathbf{K}^{-1}, \quad (4.14)$$

with the shape tensor \mathbf{K} defined by

$$\mathbf{K} = \int_{\mathcal{H}} \omega(|\boldsymbol{\xi}|)(\boldsymbol{\xi} \otimes \boldsymbol{\xi}) dV_{\boldsymbol{\xi}} .$$

When \mathbf{F} is constant, $\bar{\mathbf{F}}(\underline{\mathbf{Y}})$ is exactly equal to \mathbf{F} . If the classical model in question is hyperelastic with energy density $\Omega(\mathbf{F})$, it is a simple matter to force the peridynamic model to have identical energy by defining

$$W(\underline{\mathbf{Y}}) = \Omega(\bar{\mathbf{F}}(\underline{\mathbf{Y}})) , \quad (4.15)$$

and find the force vector state by taking the Fréchet derivative of W with respect to $\underline{\mathbf{Y}}$. Alternately, the classical continuum model can be applied to find the first Piola-Kirchhoff stress \mathbf{P} associated with $\bar{\mathbf{F}}$:

$$\mathbf{P} = \frac{\partial \Omega(\bar{\mathbf{F}})}{\partial \bar{\mathbf{F}}} . \quad (4.16)$$

The resulting force state is calculated from the stress according to

$$\underline{\mathbf{T}}(\boldsymbol{\xi}) = \omega(\boldsymbol{\xi}) \mathbf{P} \mathbf{K}^{-1} \boldsymbol{\xi} . \quad (4.17)$$

For homogenous deformations, the result is a peridynamic model that exactly reproduces the classical model without ever taking a derivative. For problems with very inhomogenous (on the scale of the peridynamic horizon) deformations, the peridynamic model will exhibit scale effects not seen in the classical model, acting to smooth out the effect of short-scale deformations. For discontinuous deformations, the classical model cannot be evaluated at all, but the peridynamic correspondence model will have no such problem. It may be necessary however to revisit the choice of model or implement some damage condition.

All three of these models are based on solid materials. In such materials, the fundamental deformation mode is stretch or extension. Consider instead a thin beam deflecting under transverse load; at the scale of the whole beam, the deflection behavior is the result of bending deformation. To model the beam with a solid material model, it is necessary to use a much smaller scale - one

in which the beam can be seen to stretch on one side and compress on the other. Alternatively, in a model whose fundamental mode of deformation is bending, the same beam could be modeled at the same scale as its behavior.

Chapter 5: MODEL DEVELOPMENT

5.1 Bond Pair Material Model

Consider the material model illustrated in fig. 5.1 in which every bond-vector originating from a point is connected by a rotational spring to its opposite originating from that same point. If we call

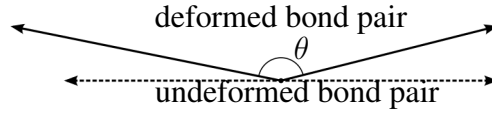


Figure 5.1: Illustration of a bond pair model that resists angular deformation

the deformed angle between these bonds θ , and choose the potential energy of that spring to be $w(\xi) = \omega(\xi)\alpha[1 + \cos(\theta)]$ for the bond pair ξ and $-\xi$, we can recover the non-ordinary force state proposed by Silling in [66] by taking the Fréchet derivative. For the derivation and a description of the Fréchet derivative see appendix A.

$$\begin{aligned} \underline{\mathbf{T}}\langle\xi\rangle &= \nabla w(\underline{\mathbf{Y}}\langle\xi\rangle) , \\ &= \omega(\xi) \frac{-\alpha}{|\underline{\mathbf{Y}}\langle\xi\rangle| |\underline{\mathbf{Y}}\langle\xi\rangle|} \times \left[\frac{\underline{\mathbf{Y}}\langle\xi\rangle}{|\underline{\mathbf{Y}}\langle\xi\rangle|} \times \frac{\underline{\mathbf{Y}}\langle-\xi\rangle}{|\underline{\mathbf{Y}}\langle-\xi\rangle|} \right] . \end{aligned} \quad (5.1)$$

Though it looks complex, eq. (5.1) indicates a bond force perpendicular to the deformed bond and in the plane containing both the deformed bond and its partner as illustrated in fig. 5.2. The force magnitude is proportional to the sine of the angle between the bonds divided by the length of the deformed bond. This response is consistent with the idea of a rotational spring between bonds as

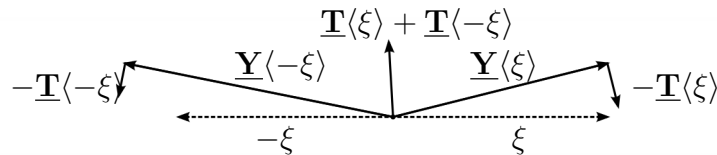


Figure 5.2: Deformation and force vector states

long as the change in angle is small. Because the potential energy and force states are functions

of *pairs* of peridynamic bonds, we will call this formulation a *bond-pair model*. Other choices for the bond-pair potential function, such as $w = (\pi - \theta)^2$, are also possible, but result in more mathematically complex analysis.

5.2 Bond Pair Beam in Bending

The simplest application of our bond-pair based peridynamic model is that of fig. 5.3, a beam in transverse bending. Much of the material in this section can also be found in [54].

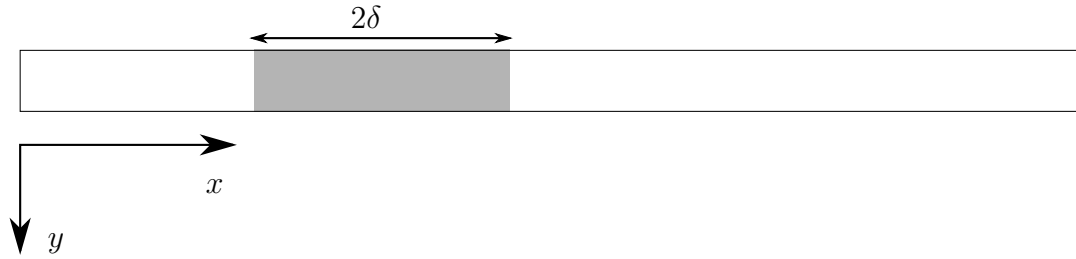


Figure 5.3: A continuous peridynamic beam with horizon δ

5.2.1 Energy Equivalence

To determine an appropriate choice of α for eq. (5.1), we desire our peridynamic model to have an equivalent strain energy density to a classical Euler-Bernoulli beam in the *local limit*, i.e. when the nonlocal length scale vanishes. We will begin with the assumptions from Euler beam theory: the length of the beam is much greater than thickness, vertical displacements are small, and rotations are small. For small vertical displacements (i.e. $\sin \theta \approx \theta$) we have

$$\theta(\underline{\mathbf{Y}}\langle\xi\rangle, \underline{\mathbf{Y}}\langle-\xi\rangle) \approx \pi - \frac{v(x+\xi) - 2v(x) + v(x-\xi)}{\xi}, \quad (5.2)$$

where v is the vertical displacement of material point. Momentarily assuming that v is continuous and using a Taylor series to expand the right-hand-side of eq. (5.2)

$$\begin{aligned}\theta(\underline{\mathbf{Y}}\langle\xi\rangle, \underline{\mathbf{Y}}\langle-\xi\rangle) &\approx \pi - \xi \frac{\partial^2 v}{\partial x^2} + \mathcal{O}(\xi^3), \\ &\approx \pi - \xi \kappa + \mathcal{O}(\xi^3),\end{aligned}\tag{5.3}$$

with

$$\kappa = \frac{\partial^2 v}{\partial x^2}.$$

Substituting eq. (5.3) into the equation for the strain energy density of a single bond-pair,

$$\begin{aligned}w(\xi) &= \omega(\xi) \alpha [1 + \cos(\theta(\underline{\mathbf{Y}}\langle\xi\rangle, \underline{\mathbf{Y}}\langle-\xi\rangle))] , \\ &\approx \omega(\xi) \alpha \frac{\xi^2}{2} (\kappa)^2 + \mathcal{O}(\xi^4).\end{aligned}$$

If we use a weighting function $\omega(\xi) = \omega(|\xi|)$ and assume that the ω plays the role of a localization kernel, i.e. $\omega = 0 \ \forall \ \xi > \delta$, the resulting strain energy density, W , for any material point in the peridynamic beam is

$$W = \frac{\alpha}{2} \kappa^2 \int_{-\delta}^{\delta} \omega(\xi) \xi^2 d\xi + \mathcal{O}(\delta^5).$$

Equating W with the classical Euler-Bernoulli beam strain-energy density, Ω , and taking the limit as $\delta \rightarrow 0$ we can solve for α

$$\begin{aligned}\lim_{\delta \rightarrow 0} W &= \Omega, \\ \frac{\alpha}{2} m \kappa^2 &= \frac{EI}{2} \kappa^2, \\ \alpha &= \frac{EI}{m},\end{aligned}\tag{5.4}$$

with

$$m = \int_{-\delta}^{\delta} \omega(\xi) \xi^2 d\xi.$$

While this demonstrates the model's equivalence to a linearly-elastic Euler beam, if we keep an additional term from the Taylor series approximation of eq. (5.2), we recover a slightly more complex expressions for change in angle that is demonstrated in 5.2.2 to reproduce an Euler beam governed by Eringen's model of nonlocal elasticity.

5.2.2 Relation to Eringen Nonlocality

If we keep an additional term from the Taylor series approximation of eq. (5.2), we recover a slightly more complex expressions for change in angle

$$\theta(\underline{\mathbf{Y}}(\xi), \underline{\mathbf{Y}}(-\xi)) \approx \arctan \left(\pi - \xi \frac{\partial^2 v}{\partial x^2} - \frac{\xi^3}{12} \frac{\partial^4 v}{\partial x^4} + \mathcal{O}(\xi^5) \right),$$

and for the strain energy (again substituting $\kappa = v''$ for readability),

$$W \approx \int_{-\delta}^{\delta} \omega(\xi) \alpha \left(\frac{\xi^2}{2} \kappa^2 + \frac{\xi^4}{12} \kappa \kappa'' - \frac{3\xi^4}{8} \kappa^4 + \mathcal{O}(\xi^6) \right) d\xi.$$

As the horizon δ becomes small, higher-order ξ terms become relatively less important, and $\xi^4 \kappa^4$ is dominated by $\xi^2 \kappa^2$ for large κ and by $\xi^4 \kappa \kappa''$ for small κ . The remaining terms can be rearranged,

$$W \approx \int_{-\delta}^{\delta} \omega(\xi) \alpha \frac{\xi^2}{2} \kappa \left(\kappa + \frac{\xi^2}{6} \kappa'' \right) d\xi,$$

in a manner strongly suggesting an alternative bending resistance term. We can picture a bending resistance based on the bond length and proportional to the nonlocal curvature $\bar{\kappa} = (\kappa + \frac{\xi^2}{6} \kappa'')$, so that

$$\begin{aligned} \bar{\kappa} &= \left(\kappa + \frac{\xi^2}{6} \kappa'' \right) \implies \\ W &\approx \int_{-\delta}^{\delta} \omega(\xi) \alpha \frac{\xi^2}{2} \kappa \bar{\kappa} d\xi. \end{aligned} \tag{5.5}$$

The same analysis can be taken further to obtain higher-order energy terms with even powers of ξ and even order derivatives of κ . Not all of these higher-order terms can be separated into the product of a local curvature and nonlocal bending resistance.

Eringen's model for nonlocal elasticity in [21] begins with a nonlocal modulus (denoted here as $K(|\mathbf{x}' - \mathbf{x}|, \tau)$) that relates the nonlocal stress \mathbf{t} at a point to the classical (local) stress $\boldsymbol{\sigma}$ in the nearby material through the integral

$$\mathbf{t} = \int_{\mathbf{V}} K(|\mathbf{x}' - \mathbf{x}|, \tau) \boldsymbol{\sigma}(\mathbf{x}') dv(\mathbf{x}').$$

In the local limit these relationships take the form of higher-order gradients. Using a 1-dimensional decaying exponential nonlocal modulus $K(|x|, \tau) = \frac{1}{\tau l} e^{-\frac{|x|}{\tau l}}$ results in a relationship between t_{1D} and σ_{1D} ,

$$\left(1 - (\tau l)^2 \frac{\partial^2}{\partial x^2}\right) t_{1D} = \sigma_{1D},$$

in which (τl) is a scale-based material parameter. For well-behaved t_{1D} and σ_{1D} and small values of σ_{1D}'''' and $(\tau l)^2$, we can see that this relationship could be reformulated as

$$t_{1D} = \left(1 + (\tau l)^2 \frac{\partial^2}{\partial x^2}\right) \sigma_{1D}.$$

If we consider the results of the previous section and let $dM = y\sigma dA$ and $\sigma = Ey\kappa$, the contribution to moment resulting from Eringen's nonlocal elasticity in a fiber at y

$$Ey^2(\kappa + (\tau l)^2 \kappa''), \tag{5.6}$$

and the resulting strain energy

$$\int_{-\frac{t}{2}}^{\frac{t}{2}} b(y) E \frac{y^2}{2} \kappa(\kappa + (\tau l)^2 \kappa'') dy,$$

bear a striking resemblance to eq. (5.5). In fact, by carefully choosing peridynamic parameter values, the results can be made identical. For a rectangular beam of width b and thickness t , choosing

$$\omega(\xi) = |\xi|b, \quad \delta = \tau l\sqrt{3}, \quad \alpha = \frac{Ebt^3}{54(\tau l)^4},$$

results in

$$W \approx Eb \frac{t^3}{12} \frac{\kappa}{2} (\kappa + \tau^2 l^2 \kappa''),$$

the same result for both models.

The similarity between eqs. (5.5) and (5.6) is not accidental; Eringen's gradient elasticity is the solution to the integral formulation of the nonlocal stress integral equation just as the peridynamic energy is an integral function of nonlocal displacements. It is therefore unsurprising that, like Eringen's nonlocal elasticity [12], this peridynamic bending model fails to predict the stiffening associated with nanoscale cantilevers. Instead, the advantage of peridynamic models is their natural handling of discontinuities.

5.2.3 Weighting function and inelasticity

The weighting function $\omega(\xi)$ describes the relative contribution of each bond-pair, and can be defined according to physical or mathematical considerations. While any function $\omega(\xi)$ that produces a convergent integral for m will reproduce an elastic Euler beam, a physically meaningful choice of ω will allow us to extend our model to certain inelastic behaviors. Consider a classical Euler-Bernoulli beam in bending with curvature κ . Fibers running parallel to the neutral axis of the beam are stretched in proportion to their distance from the neutral axis, with strain $\epsilon = y\kappa$. If the fibers are linearly elastic, then the axial stress at each location is $\sigma = E\epsilon = Ey\kappa$, and the contribution to supported moment $dM = \kappa Ey^2 dA$. By comparing the formulations for the moments carried by the Euler beam in fig. 5.4 and those of the bond-pair beam in fig. 5.5, we see some definite parallels.

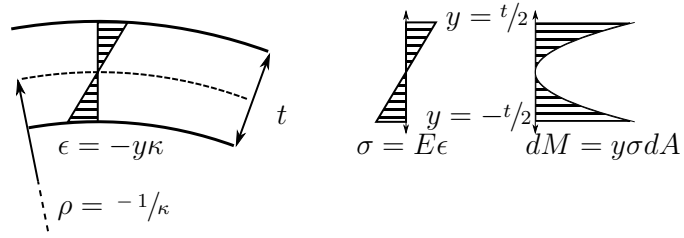


Figure 5.4: Euler beam moment contribution

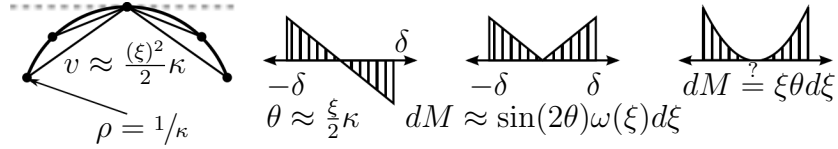


Figure 5.5: Bond-pair moment contribution

$$M_E = \int_{-\frac{t}{2}}^{\frac{t}{2}} \sigma y dA = \int_{-\frac{t}{2}}^{\frac{t}{2}} E \kappa y^2 b(y) dy, \quad (5.7a)$$

$$\begin{aligned} M_{PD} &= \int_{-\delta}^{\delta} \underline{\mathbf{T}}(\xi) \xi d\xi, \\ &= \int_{-\delta}^{\delta} \alpha \frac{\sin(\Delta\theta)}{|\xi|} \xi \omega(\xi) d\xi \approx \int_{-\delta}^{\delta} \alpha \kappa |\xi| \omega(\xi) d\xi. \end{aligned} \quad (5.7b)$$

The term y is the distance from the beam's neutral axis and $b(y)$ is the width of the beam at that distance from the neutral axis. The similarity between classical and peridynamic moment formulations in eqs. (5.7a) and (5.7b) suggests a possible formulation for the weighting function:

$$\omega(\xi) = |\xi| b(y) \quad \text{at} \quad y = \frac{\xi}{\delta} \frac{t}{2}. \quad (5.8)$$

This weight function analogizes the relative contributions of bond pairs of different lengths to the relative contributions of fibers at different distances from the centerline. An example for a rectangular beam is illustrated in fig. 5.6. For an I beam with height h_{beam} , width w_{beam} , web height

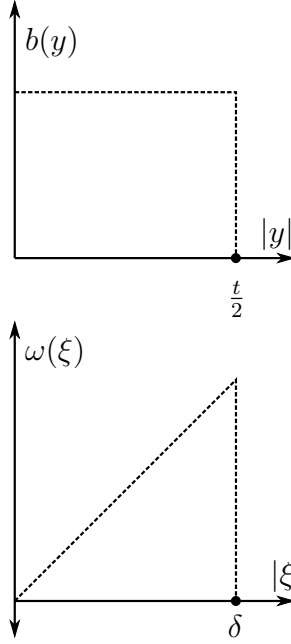


Figure 5.6: Weight function for a beam of rectangular cross-section

h_{web} , and web width w_{web} , substituting the beam profile

$$b(y) = \begin{cases} w_{\text{web}} & \text{if } |y| \leq \frac{h_{\text{web}}}{2}, \\ w_{\text{beam}} & \text{if } \frac{h_{\text{web}}}{2} < |y| \leq \frac{h_{\text{beam}}}{2}, \\ 0 & \text{otherwise,} \end{cases}$$

into eq. (5.8) gives the weight function

$$\omega(\xi) = \begin{cases} |\xi|w_{\text{web}} & \text{if } |\xi| \leq \delta \frac{h_{\text{web}}}{h_{\text{beam}}}, \\ |\xi|w_{\text{beam}} & \text{if } \delta \frac{h_{\text{web}}}{h_{\text{beam}}} < |\xi| \leq \delta, \\ 0 & \text{otherwise,} \end{cases}$$

and is illustrated in fig. 5.7. While this weighting function offers no advantages over a uniform weight function in the case of the linearly elastic beam, it offers a way to model advancing plasticity.

In a deformed elastic perfectly-plastic beam, axial fibers are still stretched in proportion to their

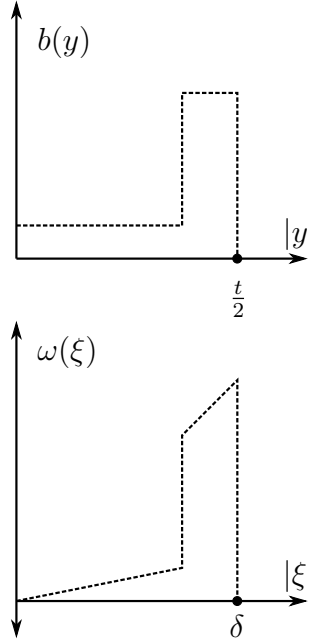


Figure 5.7: Weight function for an I-beam

distance from the neutral axis, but the relationship $\sigma = E\epsilon = Ey\kappa$ only holds for $|\epsilon| = |y\kappa| < \epsilon_c$. For greater stretches, the relationship becomes $\sigma = \pm E\epsilon_c$. To model this behavior, consider a bond pair with similar behavior: for angular deformation less than some critical angle, the model behaves as previously described, but the magnitude of the force remains constant above a critical deformation according to

$$|\underline{\mathbf{T}}\langle\xi\rangle| = \begin{cases} \alpha\omega(\xi) \frac{\sin(\theta(\underline{\mathbf{Y}}\langle\xi\rangle, \underline{\mathbf{Y}}\langle-\xi\rangle))}{|\underline{\mathbf{Y}}\langle\xi\rangle|} & \text{if } \theta < \theta_c, \\ \alpha\omega(\xi) \frac{\sin(\theta_c)}{|\underline{\mathbf{Y}}\langle\xi\rangle|} & \text{if } \theta \geq \theta_c. \end{cases} \quad (5.9)$$

To determine the critical angle θ_c , we let the onset of plasticity in pairs of the longest bonds to coincide with the onset of plasticity in the fibers at the top and bottom surfaces of the classical beam. For small curvatures $\Delta\theta = \xi\kappa \implies \Delta\theta_c = \frac{2\delta\epsilon_c}{t}$. For curvatures $|\kappa| > \kappa_c = \frac{2\epsilon_c}{t}$, the radius within which bonds are in the elastic region is $\delta_e = \delta \frac{\kappa_c}{\kappa}$, and parallels the distance from the beam

centerline that fibers are in the elastic region $y_e = \frac{t}{2} \frac{\kappa_c}{\kappa}$.

$$M_{\text{classical}} = 2 \int_0^{y_e} Eb(y)y^2 \kappa dy + 2 \int_{y_e}^{\frac{t}{2}} Eb(y)\epsilon_c y dy ,$$

$$M_{\text{PD}} = 2 \int_0^{\delta_e} \alpha \omega(\xi) \xi^2 \kappa d\xi + 2 \int_{\delta_e}^{\delta} \alpha \omega(\xi) \Delta \theta_c \xi d\xi .$$

Of course, as long as the force is independent of history, this model only represents a nonlinear elastic material. By keeping track of the plastic deformation $\theta^p(\xi) = \theta - \theta_c$ of each bond-pair, and applying it as an offset, we can reproduce the hysteresis associated with elastic-perfectly-plastic deformation.

More simply, we can model a brittle material by setting the force to zero for bond pairs exceeding a critical angle,

$$|\underline{\mathbf{T}}(\xi)| = \begin{cases} \alpha \omega(\xi) \frac{\sin(\theta(\underline{\mathbf{Y}}(\xi), \underline{\mathbf{Y}}(-\xi)))}{|\underline{\mathbf{Y}}(\xi)|} & \text{if } \theta < \theta_c , \\ 0 & \text{if } \theta \geq \theta_c , \end{cases} \quad (5.10)$$

and additionally recording bond pairs that have exceeded their critical angle and permanently setting their influence, i.e. ω , to zero.

5.3 Bond Pair Plate in Bending

The next case we will analyze is the extension of the bond pair beam model to fig. 5.8, a flat plate in the xy plane, with displacement w in the z -direction. Much of the material in this section can also be found in [55].

5.3.1 Energy Equivalence

As with the beam model, we determine an appropriate choice of α so that our peridynamic model will have an equivalent strain energy density to a classical Kirckhoff plate in the *local limit*. We will begin with the assumptions from Kirckhoff plate theory: straight lines normal to the mid-surface remain both straight and normal to the deformed mid-surface, and the plate thickness does

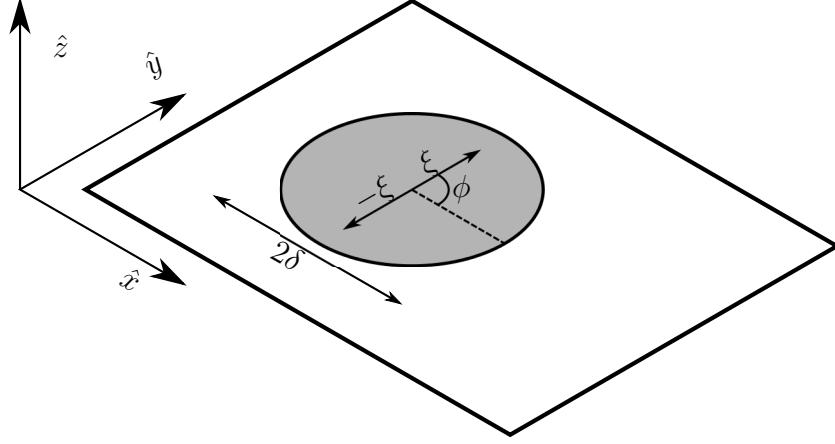


Figure 5.8: Illustration of a bond pair on a plate.

not change with deformation. As with the Euler beam energy equivalence, we will start with the original assumptions from Kirchhoff-Love plate theory of small displacements and rotations, but they will not constrain the validity of the model for larger displacements and rotations. For small vertical displacements we have

$$\theta(\underline{\mathbf{Y}}\langle \underline{\boldsymbol{\xi}} \rangle, \underline{\mathbf{Y}}\langle -\underline{\boldsymbol{\xi}} \rangle) \approx \pi - \frac{w(\mathbf{x} + \underline{\boldsymbol{\xi}}) - 2w(\mathbf{x}) + w(\mathbf{x} - \underline{\boldsymbol{\xi}})}{|\underline{\boldsymbol{\xi}}|}, \quad (5.11)$$

where w is the vertical displacement of material point. Taking $\underline{\boldsymbol{\xi}} = \xi(\cos(\phi), \sin(\phi))$ in cartesian coordinates and momentarily assuming continuous displacements for the sake of comparison, we use a Taylor series to expand the right-hand-side of eq. (5.11) about $\xi = 0$

$$\theta(\underline{\mathbf{Y}}\langle \underline{\boldsymbol{\xi}} \rangle, \underline{\mathbf{Y}}\langle -\underline{\boldsymbol{\xi}} \rangle) \approx \pi - \frac{\xi}{2} (\cos^2(\phi)\kappa_1 + \sin^2(\phi)\kappa_2 + 2\sin(\phi)\cos(\phi)\kappa_3) + \mathcal{O}(\xi^3), \quad (5.12)$$

with

$$\kappa_1 = \frac{\partial^2 w}{\partial x_1^2}, \quad \kappa_2 = \frac{\partial^2 w}{\partial x_2^2}, \quad \kappa_3 = \frac{\partial^2 w}{\partial x_1 \partial x_2}.$$

Substituting eq. (5.12) into the equation for the strain energy density of a single bond-pair,

$$\begin{aligned}
w &= \omega(\underline{\xi})\alpha [1 + \cos(\theta(\underline{\mathbf{Y}}\langle\underline{\xi}\rangle, \underline{\mathbf{Y}}\langle-\underline{\xi}\rangle))] , \\
&= \omega(\underline{\xi})\alpha \frac{\xi^2}{8} (\kappa_1^2 \cos^4(\phi) + \kappa_2^2 \sin^4(\phi) + 2\kappa_1\kappa_2 \cos^2(\phi) \sin^2(\phi) + 4\kappa_3^2 \cos^2(\phi) \sin^2(\phi) \\
&\quad + 4\kappa_1\kappa_3 \cos^3(\phi) \sin(\phi) + 4\kappa_2\kappa_3 \cos(\phi) \sin^3(\phi)) + \mathcal{O}(\xi^4) .
\end{aligned}$$

If we use a weighting function $\omega(\underline{\xi}) = \omega(\xi)$ and assume that the ω plays the role of a localization kernel, i.e. $\omega = 0 \ \forall \ \xi > \delta$, the resulting strain energy density, W , for any material point in the peridynamic plate is

$$\begin{aligned}
W &= \alpha \int_0^\delta \int_0^{2\pi} w \ \xi d\phi d\xi , \\
&= \alpha \frac{3\pi}{8} \left(\kappa_1^2 + \kappa_2^2 + \frac{2}{3}\kappa_1\kappa_2 + \frac{4}{3}\kappa_3^2 \right) \int_0^\delta \omega(\xi) \xi^3 d\xi + \mathcal{O}(\delta^6) .
\end{aligned}$$

Equating W with the classical Kirchhoff plate strain-energy density, Ω , and taking the limit as $\delta \rightarrow 0$ we can solve for α

$$\begin{aligned}
\lim_{\delta \rightarrow 0} W &= \Omega , \\
\alpha \frac{3\pi}{8} m \left(\kappa_1^2 + \kappa_2^2 + \frac{2}{3}\kappa_1\kappa_2 + \frac{4}{3}\kappa_3^2 \right) &= \left[\frac{\mu h^3}{12(1-\nu)} (\kappa_1^2 + \kappa_2^2 + 2\nu\kappa_1\kappa_2 + 2(1-\nu)\kappa_3^2) \right]_{\nu=1/3} , \\
\alpha &= \frac{2\mu h^3}{3m} , \tag{5.13}
\end{aligned}$$

with

$$m = \int_0^\delta \int_0^{2\pi} \omega(\xi) \xi^2 \xi d\phi d\xi ,$$

where μ is the shear modulus, h is the thickness of the plate, and we have evaluated the classical Kirchhoff strain-energy at a Poisson ratio of $1/3$ in order to solve for alpha as a constant. Because α is inversely proportional to m , the energy does not change with varying choices for ω and δ . It should be noted that the restriction $\nu = 1/3$ is the same imposed by the use of a bond based

peridynamic model for in-plane deformation of a 2D peridynamic plate. We will show an extension to this model that removes this restriction in Section 5.4.

5.3.2 Combining Bending and Extension Models

The bond-pair bending model does not resist in-plane stretching or shear deformation because these deformations preserve the angles between opposite bonds. If these behaviors are expected in combination with bending, a useful model must resist both in-plane and transverse deformations. To create a plate model that also resists these deformations, i.e. a flat shell, we combine the bond-pair model with a two-dimensional version of the original bond-based linearly-elastic peridynamic solid model from [64]. In this model, individual bonds act as springs resisting changes in length;

$$\underline{\mathbf{T}}\langle \boldsymbol{\xi} \rangle = \beta (|\underline{\mathbf{Y}}\langle \boldsymbol{\xi} \rangle| - |\boldsymbol{\xi}|) \frac{\underline{\mathbf{Y}}\langle \boldsymbol{\xi} \rangle}{|\underline{\mathbf{Y}}\langle \boldsymbol{\xi} \rangle|}. \quad (5.14)$$

By matching the energy of a 2D material in shear deformation, we can relate β to the shear modulus and thickness of the shell. Following the example of [66], we begin with a 2D material under pure in-plane shear. In Einstein notation, the strain energy of this material is

$$W_C = \mu h \epsilon_{ij}^d \epsilon_{ij}^d,$$

$$\begin{aligned} W_{PD} &= \frac{\beta}{2} \int_A \omega(\boldsymbol{\xi}) (|\underline{\mathbf{Y}}\langle \boldsymbol{\xi} \rangle| - |\boldsymbol{\xi}|)^2 dA_{\boldsymbol{\xi}}, \\ &= \frac{\beta}{2} \int_A \omega(\boldsymbol{\xi}) \frac{\epsilon_{ij} \xi_i \xi_j}{|\boldsymbol{\xi}|} \frac{\epsilon_{kl} \xi_k \xi_l}{|\boldsymbol{\xi}|} dA_{\boldsymbol{\xi}}, \\ &= \frac{\beta}{2} \epsilon_{ij}^d \epsilon_{kl}^d \int_A \frac{\omega(\boldsymbol{\xi})}{|\boldsymbol{\xi}|^2} \xi_i \xi_j \xi_k \xi_l dA_{\boldsymbol{\xi}}, \end{aligned}$$

where ϵ^d is the deviatoric strain tensor. To evaluate the integral we will exploit the symmetry properties. With $i, j, k, l = 1, 2$. For a circular $\omega(\boldsymbol{\xi}) = \omega(|\boldsymbol{\xi}|)$, combinations of $\{i, j, k, l\}$ with an odd number of each index, such as $\{1, 1, 1, 2\}$ or $\{2, 1, 2, 2\}$, will result in odd powers of sine and

cosine and integrate to 0.

$$\begin{aligned}
m &= \int_A \omega(\xi) |\xi|^2 dA_\xi, \\
W_{PD}^d &= \frac{\beta m}{16} [3(\epsilon_{11}\epsilon_{11} + \epsilon_{22}\epsilon_{22}) + (\epsilon_{11}\epsilon_{22} + \epsilon_{12}\epsilon_{12} + \epsilon_{12}\epsilon_{21} + \epsilon_{21}\epsilon_{12} + \epsilon_{21}\epsilon_{21} + \epsilon_{22}\epsilon_{11})], \\
&= \frac{\beta m}{16} \epsilon_{ij}^d \epsilon_{kl}^d (\delta_{ij}\delta_{kl} + \delta_{ik}\delta_{jl} + \delta_{il}\delta_{jk}), \\
&= \frac{\beta m}{8} \epsilon_{ij}^d \epsilon_{ij}^d \implies \\
\beta &= \frac{8 \mu h}{m}.
\end{aligned}$$

Having calibrated the bond-extension model to the shear modulus for a case of pure in-plane shear, applying a different uniform strain (such as might result from uniaxial tension) reveals the bond-based model to result in a one-parameter linearly-elastic model with Poisson's ratio $\nu = 1/3$.

Combining the bending and extension models allows for the description of more complex behaviors, particularly the stiffening effect of in-plane tension on the transverse bending of a shell. Consider a single bond-pair in the combined model shown in Fig. 5.9. As the two sides are pulled

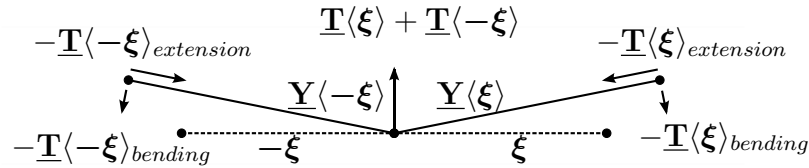


Figure 5.9: The Hybrid Model Combines Bending and Extension Components

apart, the magnitude of the extension force in each bond increases, and the magnitude of the bending force decreases. At the same time, the angle at which the extension force acts decreases, and the angle of action for the bending force increases. For small amounts of bending and reasonable stretches, increased tension in the direction of the bond pair results in increased restorative force.

5.4 Extension to arbitrary Poisson ratio

Although many materials have Poisson ratios of $\nu \approx 1/3$, it is nonetheless desirable to extend the model to materials with arbitrary Poisson ratios. For isotropic, linearly elastic models of solid materials, Silling et al. extended the peridynamic material model to arbitrary material parameters in [66] by decomposing the deformation into isotropic and deviatoric components. In the absence of plastic deformation, we need only find the difference between the strain energy of a deformed bond-based plate and the strain energy of an elastic plate with Poisson's ratio $\nu \neq 1/3$. The difference is a function of the isotropic strain in two dimensions, θ_{2D}

$$\begin{aligned} W^* &= \frac{\mu h}{2} \left(\frac{3\nu - 1}{1 - \nu} \right) \theta_{2D}^2, \\ \theta_{2D} &= \frac{2}{m} \int_A \omega(\boldsymbol{\xi}) |\boldsymbol{\xi}| (|\underline{\mathbf{Y}}(\boldsymbol{\xi})| - |\boldsymbol{\xi}|) dA_{\boldsymbol{\xi}}, \\ W_{\text{total}} &= \frac{\mu h}{2} \left(\frac{3\nu - 1}{1 - \nu} \right) \theta_{2D}^2 + \frac{4\mu h}{m} \int_A \omega(\boldsymbol{\xi}) (|\underline{\mathbf{Y}}(\boldsymbol{\xi})| - |\boldsymbol{\xi}|)^2 dA_{\boldsymbol{\xi}}. \end{aligned}$$

This is to be expected because the bond-based model was calibrated to the shear strain energy, leaving discrepancies proportional to the isotropic strain energy that fall to 0 as Poisson's ratio approaches $\nu = 1/3$.

This decomposition method inspires a similar approach to our plate model. To perform the same extension for the plate model in bending, we find the error in the 1-parameter strain energy for $\nu \neq 1/3$

$$\begin{aligned} W^* &= \frac{\mu h^3}{12(1 - \nu)} (\kappa_1^2 + \kappa_2^2 + 2\nu\kappa_1\kappa_2 + 2(1 - \nu)\kappa_3^2) \\ &\quad - \frac{\mu h^3}{12(1 - \frac{1}{3})} \left(\kappa_1^2 + \kappa_2^2 + \frac{2}{3}\nu\kappa_1\kappa_2 + 2(1 - \frac{1}{3})\kappa_3^2 \right), \\ W^* &= 2\mu \frac{h^3}{12} \frac{3\nu - 1}{1 - \nu} \left(\frac{\kappa_1 + \kappa_2}{2} \right)^2. \end{aligned}$$

The discrepancy in energy is proportional to the square of average curvature, $\frac{\kappa_1 + \kappa_2}{2}$, which we will also refer to as the isotropic curvature. The isotropic curvature can be envisioned as the portion of

the deformation that resembles a hemispherical bowl. The remainder of the bending deformation, that which is left when the isotropic curvature is subtracted out, resembles a saddle. This remaining component is the deviatoric deformation, and both components are shown in fig. 5.10. Note that the orientation of the deviatoric bending will change depending on the particular curvature being decomposed, while the isotropic curvature will only change in scale. A complete decomposition of

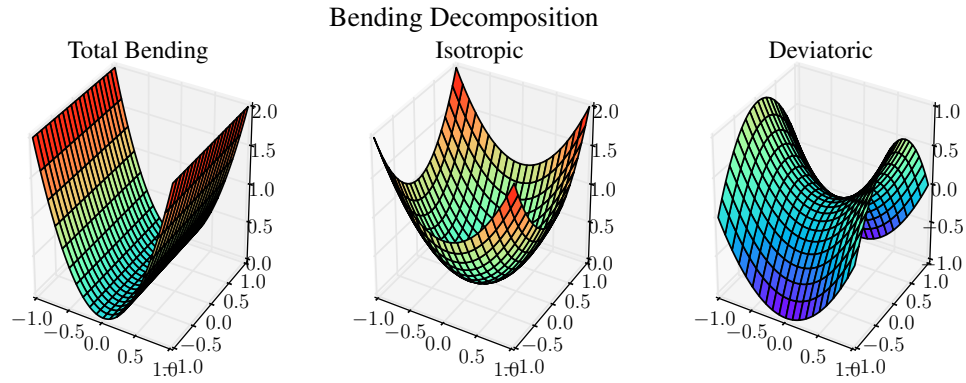


Figure 5.10: Bending Deformation Decomposed into Isotropic and Deviatoric Portions

bending energy into isotropic and deviatoric components as performed by Fischer in [24] produces a far more complex model and is unnecessary at this time. For a single bond pair we can represent the curvature vector along the bond pair as

$$\kappa_{\hat{\xi}} = \frac{\underline{\mathbf{Y}}\langle \xi \rangle + \underline{\mathbf{Y}}\langle -\xi \rangle}{|\xi|^2}.$$

For large rotations, we can define an average curvature vector $\bar{\kappa}$. This leads us to model the average curvature as

$$\begin{aligned} \bar{\kappa} &= \frac{1}{m} \int_0^\delta \int_0^{2\pi} \omega(\xi) \frac{\underline{\mathbf{Y}}\langle \xi \rangle + \underline{\mathbf{Y}}\langle -\xi \rangle}{\xi^2} \xi d\phi d\xi, \\ m &= \int_0^\delta \int_0^{2\pi} \omega(\xi) \xi d\phi d\xi. \end{aligned}$$

The weighting function $\omega(\xi)$ performs the same function as in the previous section. We can rewrite

the energy discrepancy in terms of $\bar{\kappa}$.

$$W^* = 2\mu \frac{h^3}{12} \frac{3\nu - 1}{1 - \nu} \bar{\kappa}^2.$$

We can take the Fréchet derivative (details in A) to produce a correction force vector state

$$\underline{\mathbf{T}}^*(\boldsymbol{\xi}) = \frac{8\mu}{m} \frac{h^3}{12} \frac{3\nu - 1}{1 - \nu} \frac{\omega(\boldsymbol{\xi})}{\xi^2} \bar{\kappa}, \quad (5.15)$$

that is not directly dependent on the deformation of a single bond pair. Instead, eq. (5.15) represents a bond-length dependent “pressure” applied to every pair of bonds extending from a node. This “pressure” is proportional to the curvature vector at that node. A weighting function $\omega(\boldsymbol{\xi}) = |\boldsymbol{\xi}|$ can ensure that the integral expression for force at a point is convergent. This extra term that is dependent on the bending of all the pairs around a material point means that the extension is not properly a *bond-pair* model. Instead, it would be more accurate to call it a *bond-multiple* model, in which the bond forces and energies are functions of the relationship between a family of bonds. In either the continuous or discrete cases, this model extension requires the additional step of evaluating the isotropic curvature at each point, but the increased complexity of the extended model captures in the local limit the behavior of a two-parameter elastic material plate.

Chapter 6: NUMERICAL SIMULATION

The models developed in chapter 5 are all based on a continuum material containing an infinite number of points. The model parameters and behaviors are defined by integrals over length or area, and only make sense if properties are defined continuously. This is not to say that the properties themselves need be continuous, but they cannot be defined only at a finite number of points. While such models are mathematically convenient, they are less convenient for performing many engineering problems. For the analysis of these problems, it is useful to have a discretized version of the model that can be evaluated from the properties of a finite number of peridynamic nodes that represent the continuous feature.

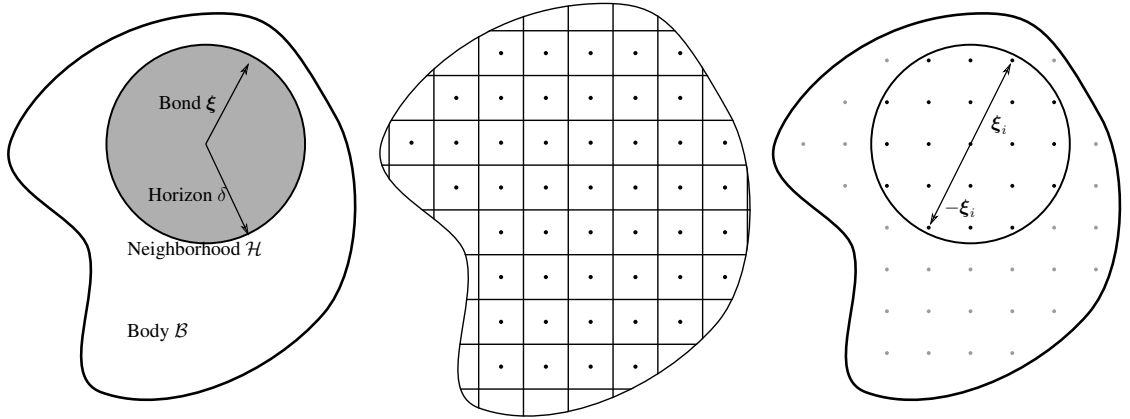


Figure 6.1: Translating Continuum Peridynamics to a Discrete Domain

Discretizing the continuous domain of interest as illustrated in fig. 6.1 is a straightforward task. First, the entire domain is divided into small, non-overlapping subdomains. Ideally, these subdomains are regular in size and compact in shape, and it is important that the largest dimension of a subdomain be similar to the smallest dimension as well as significantly smaller than the peridynamic horizon.

A peridynamic node is then placed at the centroid of each subdomain. This node has no volume (is a zero-dimensional point), but it does have mass equal to the mass of the material in the subdomain. After the nodes are placed, neighborhoods are constructed. The neighborhood of the node at \mathbf{x}_i consists of all the nodes \mathbf{x}_j for whom $|\mathbf{x}_j - \mathbf{x}_i|$ is smaller than the horizon. As the number

of nodes in each neighborhood increases, the material represented by the nodes in a neighborhood will converge to the material within the horizon in the continuous domain. At the same time, the integrals of well-behaved functions over neighborhood regions in the continuous model can be approximated by weighted sums of the same functions evaluated at the discrete nodes in a neighborhood. This is the key to translating the continuous peridynamic model into a more practical discrete version.

6.1 Discretized Bond Pair Beam

Discretizing the bond-pair model is primarily matter of exchanging integrals for sums,

$$\begin{aligned} w(\xi_i) &= \omega(\xi_i) \alpha [1 + \cos(\theta(\underline{\mathbf{Y}}\langle \xi_i \rangle, \underline{\mathbf{Y}}\langle -\xi_i \rangle))] , \\ &\approx \omega(\xi_i) \frac{\alpha}{2} \left(\frac{v(\mathbf{x} + \xi_i) - 2v(\mathbf{x}) + v(\mathbf{x} - \xi_i)}{\xi_i} \right)^2 , \end{aligned}$$

in which ξ_i is the i^{th} bond emanating from the point \mathbf{x} to each of the n points within distance δ of point \mathbf{x} .

$$\begin{aligned} \alpha &= \frac{c \Delta x}{m}; \quad c = EI; \quad m = \sum_{i=1}^n \omega(\xi_i) \xi_i^2 \implies \\ W &= \Delta x \sum_{i=1}^n \frac{EI}{2} \omega(\xi_i) \left(\frac{v(\mathbf{x} + \xi_i) - 2v(\mathbf{x}) + v(\mathbf{x} - \xi_i)}{\xi_i} \right)^2 . \end{aligned} \quad (6.1)$$

Discretization of the original model results in the equation of motion,

$$\begin{aligned} \rho(\mathbf{x}) \ddot{\mathbf{u}}(\mathbf{x}) &= \mathbf{f}(\mathbf{x}) + \sum_i \omega(\xi_i) \left\{ \frac{\alpha(\mathbf{x})}{|\mathbf{p}_i|} \frac{\mathbf{p}_i}{|\mathbf{p}_i|} \times \left[\frac{\mathbf{p}_i}{|\mathbf{p}_i|} \times \frac{\mathbf{q}_i}{|\mathbf{q}_i|} \right] \right. \\ &\quad \left. - \frac{\alpha(\mathbf{x} + \xi_i)}{|\mathbf{p}_i|} \frac{(-\mathbf{p}_i)}{|\mathbf{p}_i|} \times \left[\frac{(-\mathbf{p}_i)}{|\mathbf{p}_i|} \times \frac{\mathbf{r}_i}{|\mathbf{r}_i|} \right] \right\} , \end{aligned} \quad (6.2)$$

with

$$\begin{aligned}\mathbf{p}_i &= \boldsymbol{\xi}_i + \mathbf{u}(\mathbf{x} + \boldsymbol{\xi}_i) - \mathbf{u}(\mathbf{x}) , \\ \mathbf{q}_i &= -\boldsymbol{\xi}_i + \mathbf{u}(\mathbf{x} - \boldsymbol{\xi}_i) - \mathbf{u}(\mathbf{x}) , \\ \mathbf{r}_i &= \boldsymbol{\xi}_i + \mathbf{u}(\mathbf{x} + 2\boldsymbol{\xi}_i) - \mathbf{u}(\mathbf{x} + \boldsymbol{\xi}_i) ,\end{aligned}$$

and for small displacements and rotations in a uniform beam,

$$\begin{aligned}\rho(\mathbf{x})\ddot{v}(\mathbf{x}) &= f(\mathbf{x}) \\ &+ \alpha \sum_i 2\omega(\xi_i) \left(\frac{v(\mathbf{x} - 2\boldsymbol{\xi}_i) - 4v(\mathbf{x} - \boldsymbol{\xi}_i) + 6v(\mathbf{x}) - 4v(\mathbf{x} + \boldsymbol{\xi}_i) + v(\mathbf{x} + 2\boldsymbol{\xi}_i)}{\boldsymbol{\xi}_i^2} \right) .\end{aligned}$$

It is worth noting the similarity between this expression and a finite-difference fourth derivative of displacement, a result expected from Euler beam theory. This discretization requires that nodes be evenly spaced along the entire beam, otherwise the displacement $v(\mathbf{x} - \boldsymbol{\xi}_i)$ is ill-defined. For this reason, the discretization does not allow for areas of higher and lower “resolution”.

6.2 Discretized Bond Pair Plate

As with the beam, discretizing the bond-pair model is primarily matter of exchanging integrals for sums;

$$\begin{aligned}\alpha &= \frac{c (\Delta x)^2}{m}; \quad c = \frac{\mu}{(1 - \nu)} \frac{h^3}{12}; \quad m = \sum_{i=1}^n \omega(\boldsymbol{\xi}_i) \boldsymbol{\xi}_i^2 \implies \\ W &= (\Delta x)^2 \sum_{i=1}^n \omega(\boldsymbol{\xi}_i) \frac{\mu}{2(1 - \nu)} \frac{h^3}{12} \left(\frac{w(\mathbf{x} + \boldsymbol{\xi}_i) - 2w(\mathbf{x}) + w(\mathbf{x} - \boldsymbol{\xi}_i)}{|\boldsymbol{\xi}_i|} \right)^2 .\end{aligned} \tag{6.3}$$

Discretization of the 1-parameter bending model results in the same equation of motion as for the beam model (eq. 6.2).

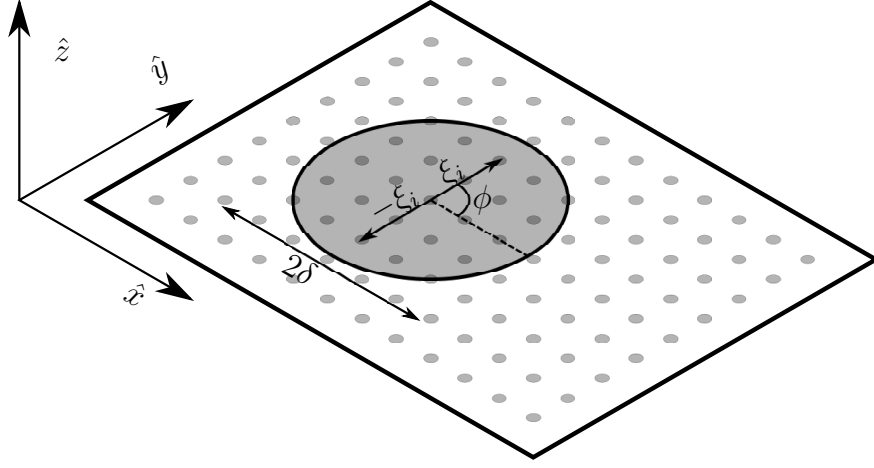


Figure 6.2: Discretized peridynamic plate with illustrated bond pair

Implementing the 2-parameter model requires finding the isotropic curvature at each point.

$$\begin{aligned}\bar{\kappa}(\mathbf{x}) &= \frac{1}{m} \sum_i \omega(\xi_i) \frac{\mathbf{p}_i + \mathbf{q}_i}{\xi_i^2}, \\ m(\mathbf{x}) &= \sum_i \omega(\xi_i), \\ \alpha^{\text{iso}}(\mathbf{x}) &= \frac{4\mu}{m} \frac{h^3}{12} \frac{3\nu - 1}{1 - \nu} (\Delta x)^2, \\ f^{\text{iso}}(\mathbf{x}) &= \sum_j \left\{ \left[\alpha^{\text{iso}}(\mathbf{x}) \bar{\kappa}(\mathbf{x}) - \alpha^{\text{iso}}(\mathbf{x} + \xi_j) \bar{\kappa}(\mathbf{x} + \xi_j) \right] \frac{\omega(\xi_j)}{\xi_j^2} \right\}.\end{aligned}$$

As with the discretized beam, the discretization of the bond-pair plate (fig. 6.2) must be absolutely regular. Discretizing the bond-pair model as proposed above requires that nodes be evenly spaced, Δx , throughout the entire plate, otherwise the displacement $w(\mathbf{x} - \xi_i)$ is undefined. For this reason, the discretization does not allow for areas of higher and lower “resolution”. This restriction, while inconvenient in the 1D case, is fairly restricting for plate analysis. An extension to this discretization that would allow changing mesh resolution will require interpolation between the nodes.

6.3 Numerical Model Extensions

6.3.1 Curved Shapes

On a curved surface, the location of the point $x - \xi$ might be off of the surface entirely. One method of applying the bond-pair model to curved surfaces is through the use of “virtual” points. These points have no mass and do not have families of peridynamic neighbors, they only allow the definition of bond pairs that are straight in the undeformed configuration. In the simplest method,

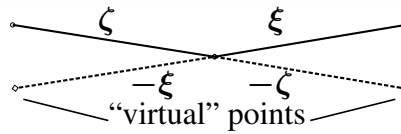


Figure 6.3: Virtual Points Allow Straight Pairs on Curved Surfaces

each virtual point is located just above or below a real point in the model. In this case, properties such as displacement are taken to be the same as for the nearby real point. Because the virtual

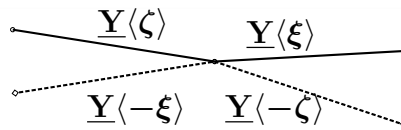


Figure 6.4: Virtual Points Take the Displacement of Nearby Real Points

point has no mass is not part of any other bond pairs, it cannot be assigned a force. Instead, the force on a virtual point resulting from deformation of a bond pair is instead applied to the nearest real points. This results in a straightforward extension of the bending model from flat plates (and beams) to features that have curvatures that are small over the peridynamic horizon.

6.3.2 Irregular Discretization

A curved surface is not the only reason to implement virtual points, and even many curved surfaces do not allow for regular discretization. When discretization is irregular, due to three-dimensional curvature, irregular shapes, or a need for increased resolution in some areas, there are necessarily points at which there is no real point at the location of $\mathbf{x} - \boldsymbol{\xi}$. An example of changing mesh density resulting in a need for interpolation can be found in fig. 6.5, which shows a small family of nodes at the edge of a change in discretization coarseness. Note that, while bonds p_2 and q_2 form

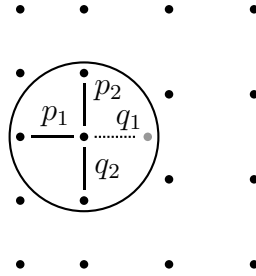


Figure 6.5: Virtual Points Pair Up Unpaired Neighbors

a perfect bond pair, there is no bond exactly opposite p_1 . To solve this, we add a virtual point to create a bond, q_1 , that will form a pair with p_1 . Because this point is not part of the discretization, it has no mass, and its properties must be determined from the properties of the surrounding nodes.

An easy method of determining properties (such as displacement) at virtual nodes is to use a weighted average. For an irregular straight beam, determining the values of properties at virtual points is simple. To determine the value of a property at point C , we used a weighted average of the values of that property at the nearest two real points, A and B . The weight value w_B of B is determined to make a linear interpolation (or extrapolation) using the x -coordinates of the nearest

two real points.

$$W_B = -\frac{C_x - A_x}{A_x - B_x},$$

$$W_A = 1 - w_B.$$

The problem becomes a little more complicated for curved beams, but we can tackle it by projecting the virtual point onto the line between the two nearest real points. The weighting function is then computed according to

$$\overline{AC'} = \frac{\overline{AB}}{|\overline{AB}|} \left(\frac{\overline{AB}}{|\overline{AB}|} \cdot \overline{AC} \right),$$

$$\overline{BC'} = \frac{\overline{BA}}{|\overline{BA}|} \left(\frac{\overline{BA}}{|\overline{BA}|} \cdot \overline{BC} \right),$$

$$W_B = \begin{cases} \frac{|\overline{AC'}|}{|\overline{AB}|} & \text{if } |\overline{BC'}| \leq |\overline{AB}|, \\ -\frac{|\overline{AC'}|}{|\overline{AB}|} & \text{otherwise,} \end{cases}$$

$$W_A = 1 - W_B.$$

Determining properties at virtual points is more difficult in plate and shell models. One method of generating useful weights that is relatively robust is barycentric interpolation. We start by finding the three (non-colinear) real nodes closest to the location of the virtual node, A, B, and C. Next, we find the signed areas of the triangles ABC, ABX, BCX, and CAX, with X being the virtual node. The weight of node A is the area ratio between BCX and ABC, the weight of node B is the ratio of areas CAX and ABC, and the weight of node C is the ratio of areas ABX to ABC. Using signed areas allows the weights to be negative to extrapolate properties of a virtual node outside of ABC. Because these weights are calculated from the initial positions of the node, they can be stored for swift evaluation of properties at virtual nodes.

With the properties of the virtual points determined, the model can be evaluated in the same manner as the uniformly discretized models of the previous papers. Where forces are calculated

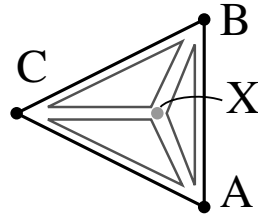


Figure 6.6: Barycentric interpolation is based on the relative areas of sub triangles

to act on a virtual node, those forces are redistributed to the supporting real nodes according to the weight each point has in the interpolation. Barycentric interpolation is linear and therefore exactly reproduces the linear displacement fields in fig. 6.7, including extrapolation well outside the interpolation points (all of which are within the square with corners (0,0) and (1,1)). Unfortunately, as fig. 6.8 demonstrates, barycentric interpolation is not exact for quadratic surfaces. The difference between the quadratic surface and the linear interpolation decreases with denser discretization as the curvature of the surface between interpolation points decreases, as demonstrated in fig. 6.8. This method therefore requires that the curvature of the surface be small relative to the peridynamic horizon to ensure accurate virtual node properties.

The same method of virtual nodes also allows the modeling of curved surfaces, in which the perfect opposite of a bond may not lie near but not on the surface of the plate or shell. As long as the curvature of the surface is small (at the scale of the peridynamic horizon), each resulting virtual nodes will be nearly in the plane formed by its nearest neighbors. Finding the weights of the surrounding nodes is performed just as in the planar case, except that the areas are formed between the projection of the virtual node location X onto the plane formed by A, B, and C.

To compute the weight of node A in the interpolation of properties at virtual node X, let \vec{AB} represent the vector from node A to node B, and use

$$\hat{W}_A = \frac{B - X}{2} \cdot \left[\vec{BC} \times \left(\frac{\vec{BC} \times \vec{BA}}{|\vec{BC} \times \vec{BA}|} \right) \right]. \quad (6.4)$$

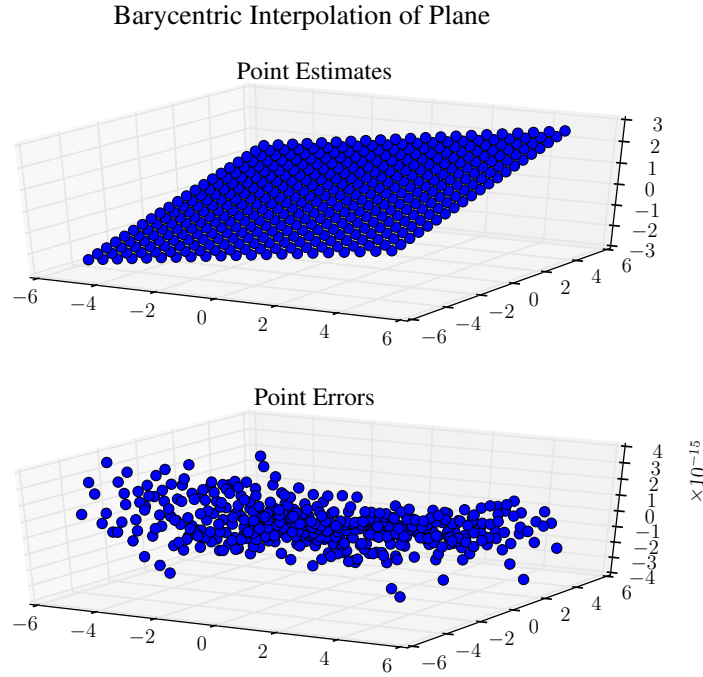


Figure 6.7: Barycentric estimate and error for plane interpolation

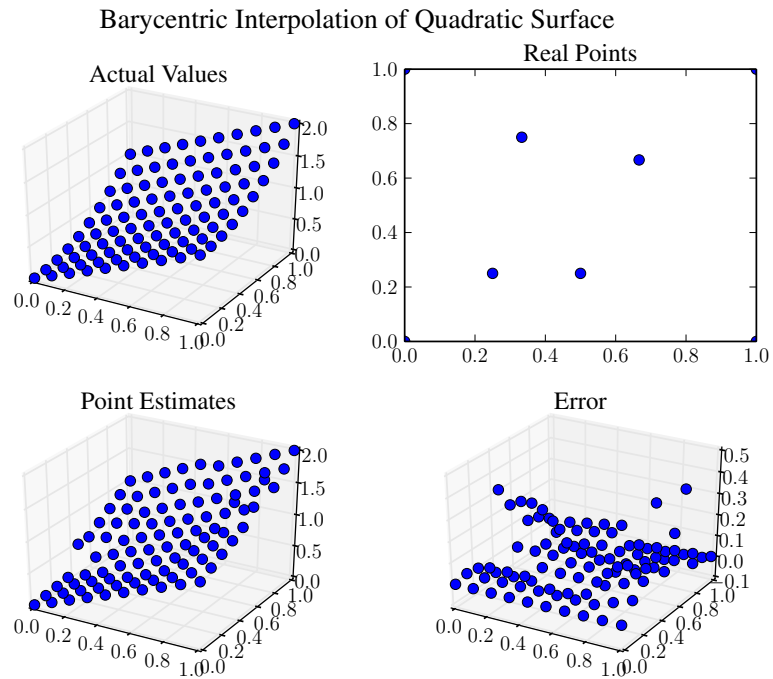


Figure 6.8: Barycentric estimate and error for quadratic surface

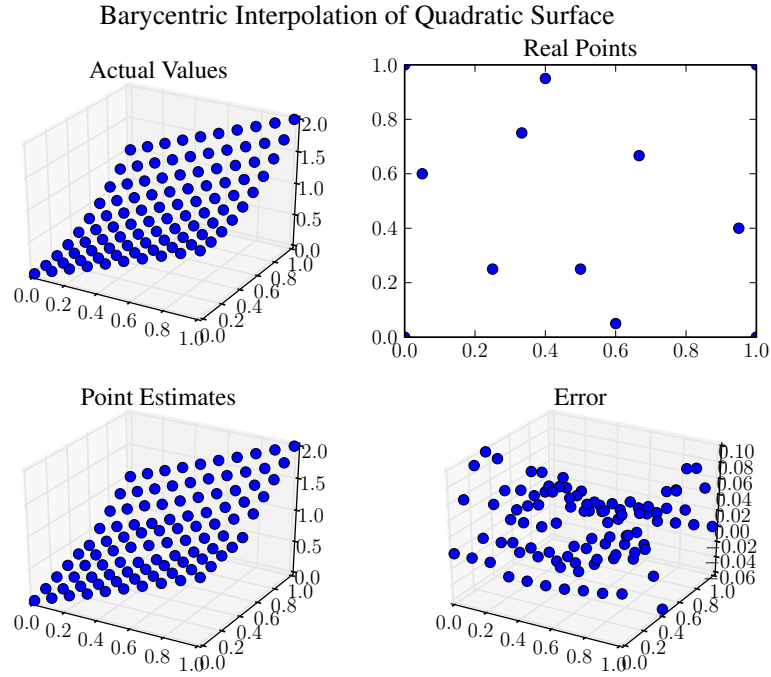


Figure 6.9: Barycentric estimate improves with denser discretization

After finding \hat{W}_B and \hat{W}_C in similar fashion,

$$W_A = \frac{\hat{W}_A}{\hat{W}_A + \hat{W}_B + \hat{W}_C}. \quad (6.5)$$

If the projection of X onto the plane defined by A , B , and C lies outside the triangle ABC , one or two of W_A , W_B and W_C will be negative, though they will still sum to 1.

6.3.3 Extended Discretization

With the addition of virtual points and the incorporation of irregular discretizations, it is necessary to reformulate the discretized bending model. The bond pair coefficients at point \mathbf{x} of a beam in bending (eq. (6.1)) become

$$\alpha_i = \frac{c l(\mathbf{x}) l(\mathbf{x} + \boldsymbol{\xi}_i)}{m}, \quad c = EI, \quad m = \sum_{i=1}^n \omega(\boldsymbol{\xi}_i) \xi_i^2 l(\mathbf{x} + \boldsymbol{\xi}_i),$$

with $l(\mathbf{x})$ and $l(\mathbf{x} + \boldsymbol{\xi}_i)$ representing the lengths of beam represented by the nodes at (\mathbf{x}) and $(\mathbf{x} + \boldsymbol{\xi}_i)$. Similarly, the plate coefficients from eq. (6.3) become

$$\alpha_i = \frac{c A(\mathbf{x})A(\mathbf{x} + \boldsymbol{\xi}_i)}{m}, \quad c = \frac{\mu}{(1 - \nu)} \frac{h^3}{12}, \quad m = \sum_{i=1}^n \omega(\boldsymbol{\xi}_i) \boldsymbol{\xi}_i^2 A(\mathbf{x} + \boldsymbol{\xi}_i),$$

with $A(\mathbf{x})$ and $A(\mathbf{x} + \boldsymbol{\xi}_i)$ representing the areas represented by the nodes at (\mathbf{x}) and $(\mathbf{x} + \boldsymbol{\xi}_i)$. Note that for both plate and beam, the value of α now varies between bonds.

6.4 “Boundary” Conditions

Because peridynamic models result in long range forces, it is not sufficient to apply boundary conditions to nodes on the relevant boundary; nodes near the boundary must be considered as well.

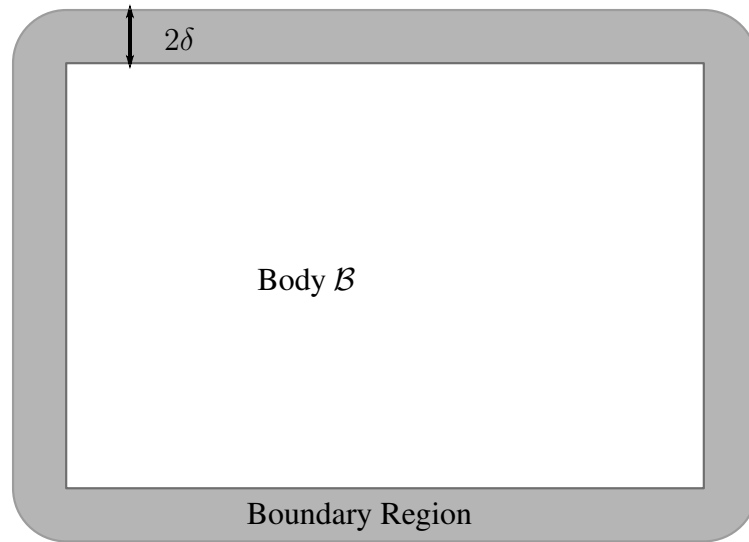


Figure 6.10: The boundary of a peridynamic model is a region of nonzero thickness

For the peridynamic beam we consider simple supports or rollers, and fixed or clamped supports. Simply-supported beams are easy to model because only displacement is constrained. To add a roller support to the peridynamic beam, it suffices to constrain the movement of the nearest peridynamic node in the appropriate degree(s) of freedom. Simulating a “clamped” end condition

is a little less intuitive. The most basic way to simulate a clamped end is to extend the beam 2δ , or twice the horizon, into the clamp. The displacement of all of those nodes is set to zero, or whatever value is appropriate for a displaced or rotated clamp. In classical mechanics, a clamped end can be described with a symmetry condition, but the two are not peridynamically equivalent. Because the classical beam is a local model, material at a clamp cannot “see” distant material, so there is no way to distinguish between a beam end that is clamped and one that is bent symmetrically over an appropriate sawhorse.

The loads we apply to the peridynamic beam include applied moments, point loads and distributed loads. Distributed forces may be applied as expected to nodes in the loaded region. Point forces may often be applied directly to the nearest node, or to the nodes immediately surrounding the point of application. Point moments must also be considered more carefully because the peridynamic models in this work, like most peridynamic models, do not consider rotational degrees of freedom for peridynamic nodes. Rather, material rotation is the result of the relative translational displacement of multiple nodes. It is therefore impossible to apply a moment to a single peridynamic point. Instead, moments may be applied as force couples to the bonds attached to the peridynamic node nearest the location of the desired moment. For example, if we want to apply a moment M at point \mathbf{x} , whose n neighboring points \mathbf{x}'_i are connected to \mathbf{x} in the undeformed configuration by bonds ξ_i . For an evenly discretized beam, we may distribute the moments by

$$M_i = M \frac{\omega(\xi_i)}{\sum_{j=1}^n \omega(\xi_j)},$$

and apply them to the corresponding bonds by adding forces

$$\mathbf{F}_i = M_i \times \frac{\underline{\mathbf{Y}}\langle \xi_i \rangle}{|\underline{\mathbf{Y}}\langle \xi_i \rangle|^2}$$

to each point \mathbf{x}_i and subtracting them from the force at \mathbf{x} .

Support configurations are similar for two-dimensional models. Each node along a simply-

supported edge is constrained in one or more directions. As with the beam model, clamped edges are implemented by extending the surface into the clamp. Line and pressure loads are treated normally.

6.5 Numerical Solution Method

This project uses Trilinos, a collection of open software libraries, or packages, from Sandia National Labs, including:

- Epetra and EpetraExt - provide efficient parallel data structures, particularly vectors and sparse matrices
- Isorropia - provides load balancing, partitioning, and matrix coloring
- NOX - a collection of large-scale nonlinear system solver utilities
- PyTrilinos - a python interface providing Python wrappers for many Trilinos packages, and offering compatibility between `numpy.ndarrays` and `Epetra.MultiVectors` [61]

The nature of discrete peridynamic models results in large numbers of parallelizable computations. Efficient parallelization is achieved using Epetra data structures for distributed variables. Model force evaluations are coded in Python, making extensive use of the optimized routines in the NumPy and SciPy packages operating on the distributed Epetra objects. To obtain quasistatic solutions, problems are coded into NOX objects and solved using NOX nonlinear solvers. Preliminary analysis was performed using a Newton Method solver on an iMac with a 3.1GHz Intel Core i7 processor and 16GB RAM, using 1-4 cores. Later work also performed on Shamu, a High-Performance Computing cluster at UTSA, and Stampede, a High-Performance Computing cluster at UT Austin. The nature of the Trilinos packages and the structure of the code allow for more extensive parallel computation without major code changes.

For all but the simplest loading conditions, analytical solutions to boundary condition problems become complicated. As load conditions and material behavior become more complex, there are

no analytical solutions. For comparison, equivalent models are created and analyzed in Abaqus 6.12 to verify simple cases.

6.6 Results

6.6.1 Straight Beam Results

The simplest test case for this model is a linear-elastic beam with a square profile. These models represent beams that are 1cm thick and 1cm wide, with a bulk modulus $k = 37.5\text{GPa}$ and Poisson's ratio $\nu = 1/3$. Each is loaded transversely with a load of 0.0833N , except for fig. 6.13, which shows a beam loaded with a moment of $0.0833\text{N}\cdot\text{m}$. In beams simulating inelastic behavior, the critical strain of the material is set to $\varepsilon_c = 0.001$. The elastic cases are compared to analytical solutions of the Euler beam equation with appropriate boundary conditions. Even a coarse discretization successfully reproduces the shape of the elastically deformed, simply-supported beam shown in fig. 6.11 deformed under uniform load. Other load types are also possible; figs. 6.12 and 6.13

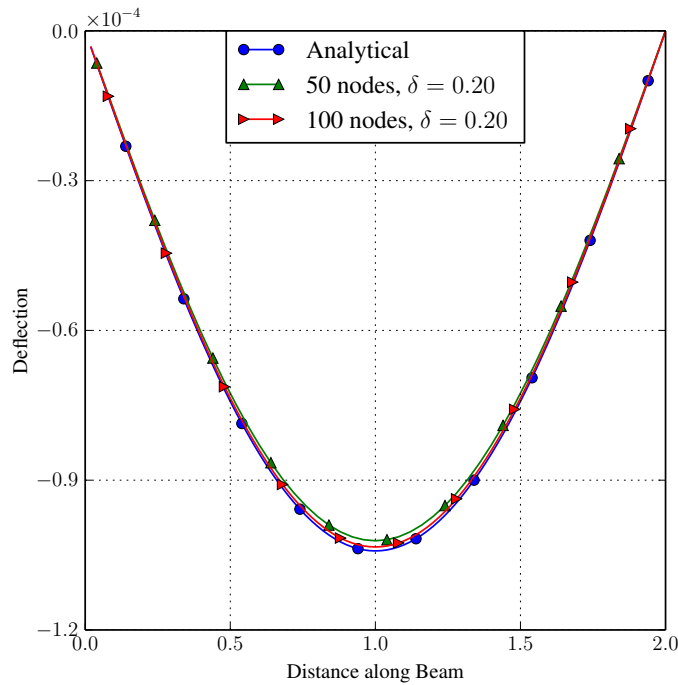


Figure 6.11: The uniform-load elastic beam is accurately modeled with few nodes

demonstrate simply-supported elastic beams with a point load and a point moment, respectively.

It is more difficult to accurately reproduce the behavior of a clamped-end beam. It is evident

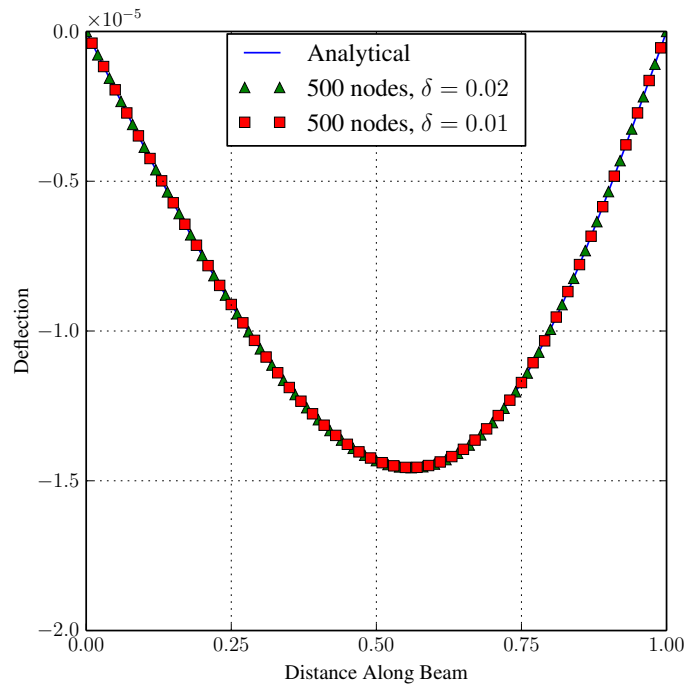


Figure 6.12: Simply Supported Beam with Point Load

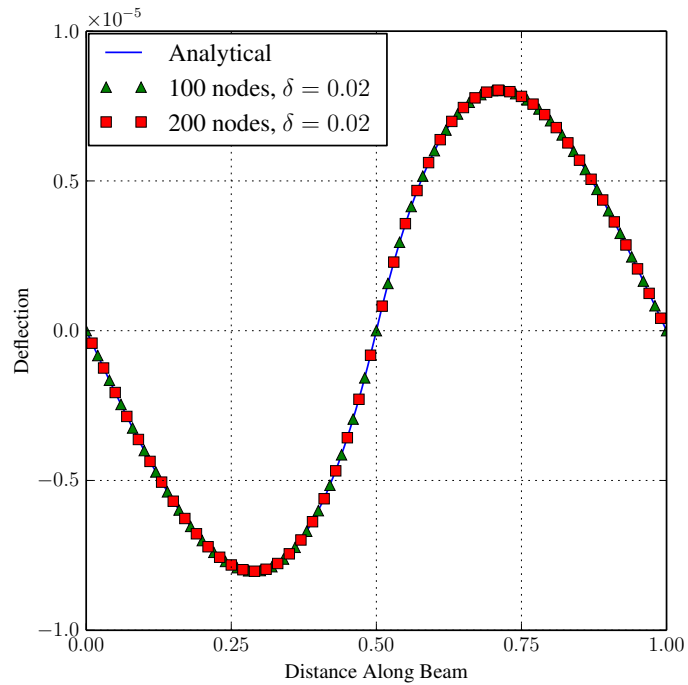


Figure 6.13: Simply Supported Beam with Point Moment at Center

from figs. 6.14 and 6.15 that the clamped end constraint requires far more nodes and a smaller horizon to reproduce the results of a classical elastic model. Figure 6.16 shows a cantilever beam with one clamped end and one free end, deflecting under a uniformly distributed load.

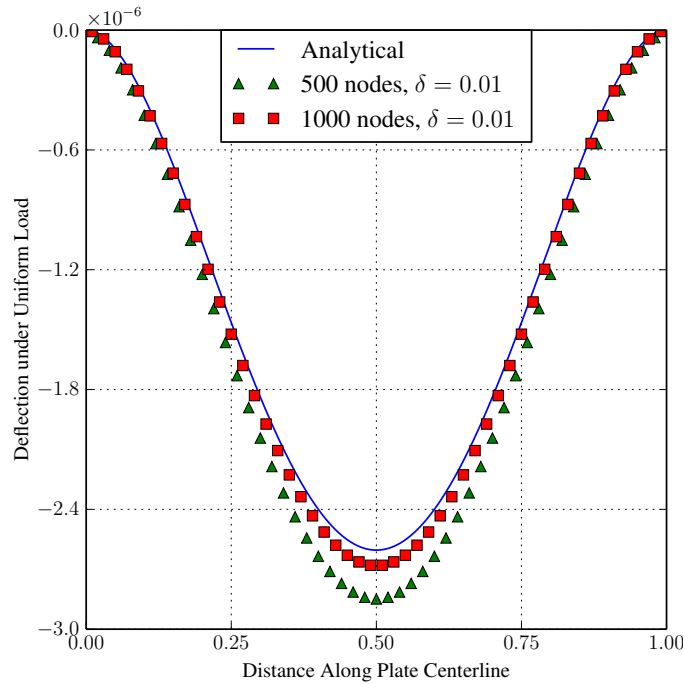


Figure 6.14: The clamped condition requires finer discretization

As an elastic-perfectly-plastic beam exceeds the elastic limit of its material, plastic zones begin to grow on the top and bottom of the beam's cross section. This behavior is mimicked by the plasticity of the longest bond-pairs described in eq. (5.9), producing the results shown in fig. 6.17. To evaluate plastic beam behavior, plastic beam models with identical material properties are created and analyzed in Abaqus 6.12 to verify simple cases. To accurately capture this phenomenon and model beam plasticity, a finer discretization is required.

A material that is plastically deformed does not return to its original state when unloaded. For a beam in bending, the residual deformations can be seen in a beam that has been loaded beyond the onset of plastic deformation and then unloaded. The Abaqus model retains slightly more than $\frac{1}{10}$ of its loaded displacement after being completely unloaded. This result is observed in the

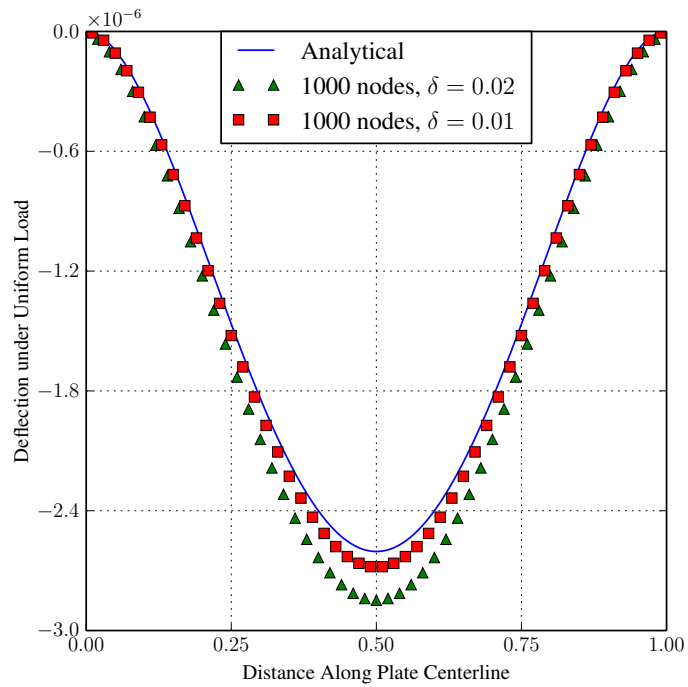


Figure 6.15: The clamped condition requires a smaller horizon

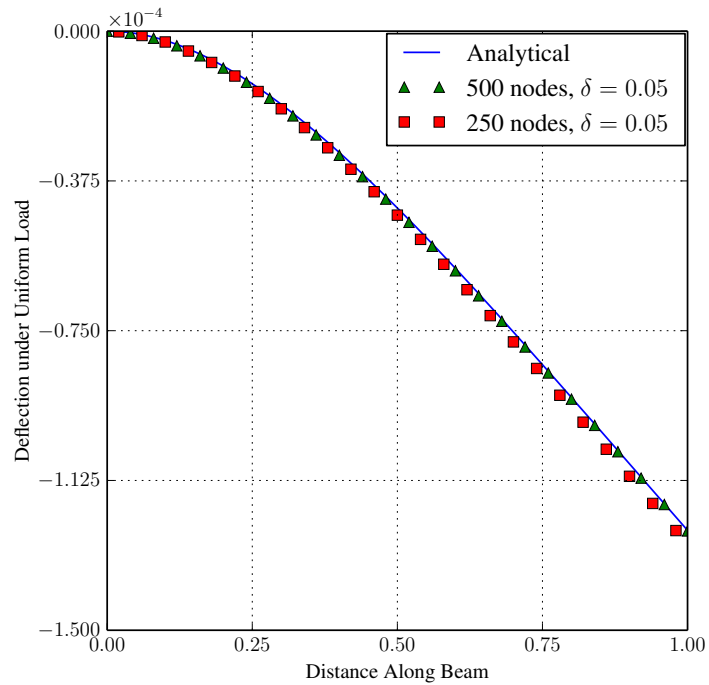


Figure 6.16: Uniformly Loaded Cantilever Beam

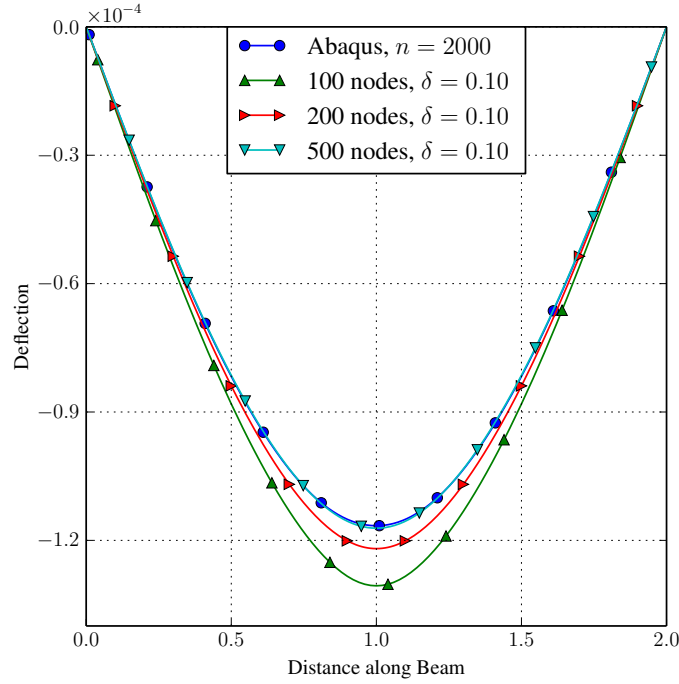


Figure 6.17: The elastic perfectly-plastic beam requires finer discretization

bond-pair plasticity model, shown in figs. 6.18 and 6.19. Accurate residual deformation modeling requires both a relatively small horizon and a fairly large number of nodes. While this makes for a computationally expensive model in this case, it allows for implementation of more complex plasticity models without additional expense; a plasticity model that includes softening is no more effort to implement, and would result in damage fields that depend on the peridynamic horizon, not on the density of the discretization. Because the peridynamic horizon is ideally a material property, this has the effect of regularizing the solution. Implementing a strain-softening plasticity model in a finite element beam would, by contrast, result in the localization of plasticity into one element and depend strongly on the choice of discretization.

It is more difficult to verify the brittle material model described by eq. (5.10) because brittle failure is unstable. When a crack begins, moment is transferred to other bond pairs, and failure progresses until every pair of bonds surrounding a node are broken, creating a hinge at that node. This is borne out by the results in fig. 6.20, in which “Nodal Health” represents the fraction of

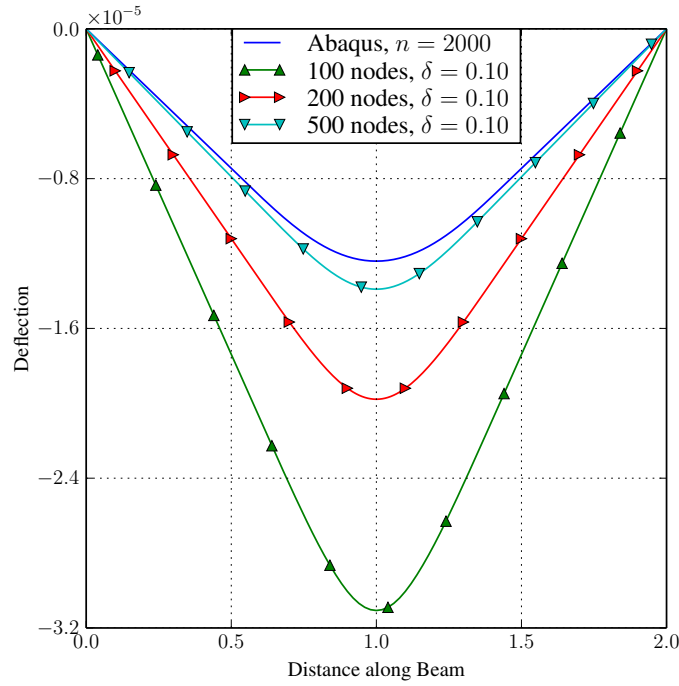


Figure 6.18: The need for fine discretization is even more apparent when representing residual plastic deformation

bond-pairs about each node that have never exceeded their critical angle and therefore have not failed.

Unlike a local model, partial failure is observed at nodes near the plastic hinge, as pairs of bonds that straddle the hinge are broken. This is an important feature of peridynamics; as in the plastic beam, the damaged region of the brittle beam depends on the peridynamic horizon rather than on the density of the discretization. In a finite element model, damage will occur between elements or within a single element. Either way, mesh refinement will eventually result in damage localization to an infinitely small damage region.

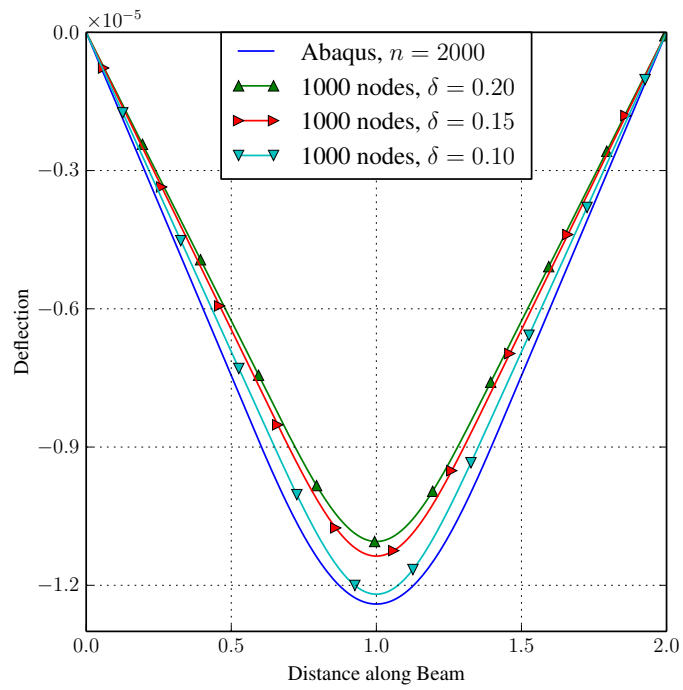


Figure 6.19: Accurately modeling residual plastic deformation also requires a small horizon

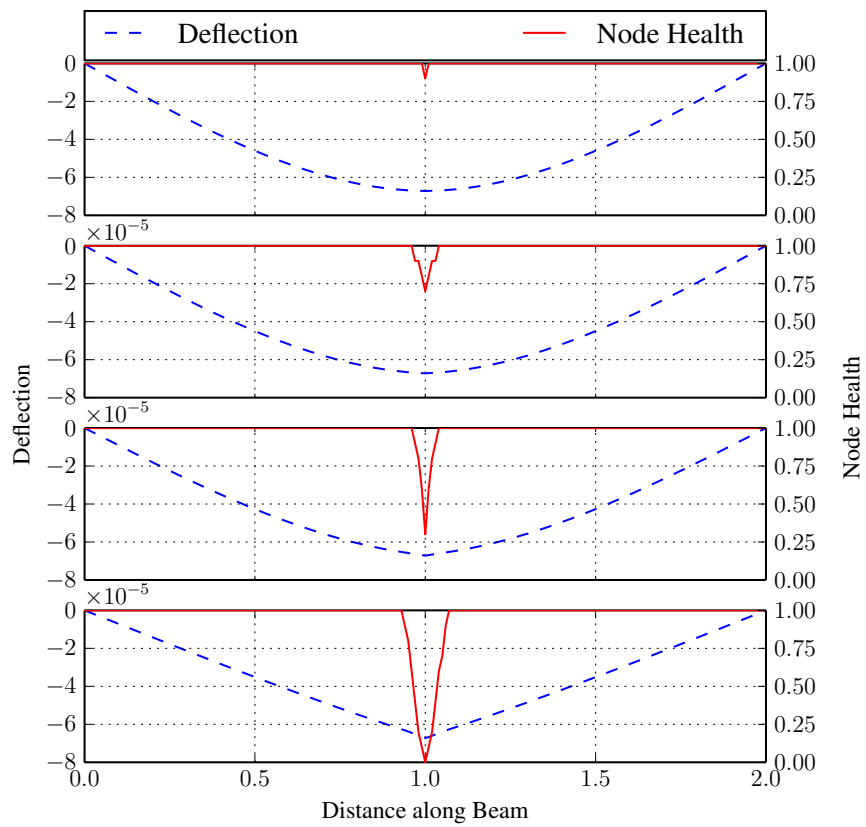


Figure 6.20: A brittle beam with prescribed center displacement

6.6.2 Flat Plate Results

The simplest test case for the 2D model is a linear-elastic 1m by 1m plate that is simply-supported on all 4 sides with a uniform transverse pressure load on the entire surface between the supports. The plates in this section have a shear modulus $k = 37.5\text{GPa}$, and unless otherwise noted, a Poisson's ratio of $\nu = 1/3$. The elastic plates are all loaded with a total transverse force of 937.5N. As expected from an energy-equivalent model, the slice along the plate's centerline shown in fig. 6.21 demonstrates good agreement between the static deflection predicted by the bond-pair model and that of classical linear elasticity as the horizon length shrinks. This convergence only continues to a minimum horizon, below which the discretized equation of motion (eq. (6.2)) ceases to accurately approximate the continuous integral formulation (eqs. (4.1) and (5.1)). The minimum horizon size depends on the discretization; it appears that three times the node spacing is sufficient, but that a horizon that is only twice the node spacing is insufficient. The difference is evident in fig. 6.22, which also shows that results are insensitive to fineness of discretization once the minimum horizon criterion is met. Accurate results require a denser discretization than is the case for the elastic beams from previous work. Figure 6.23 illustrates the model converging to the analytical solution as the discretization is made finer and the horizon shrinks.

The test case for the hybrid model is a similar simply-supported square plate with an additional in-plane tension load along two opposing sides. An analytical solution for this combination of uniform transverse pressure and in-plane edge tension can be found in Timoshenko's book [74]. As is mechanically intuitive, increasing in-plane tension results in decreasing transverse displacement, while the opposite is true for compressive edge loading. Normalized to the the maximum displacement of a transversely-loaded plate with no in-plane edge loads, the results in fig. 6.24 show that the hybrid model does a good job of simulating the impact of in-plane tension on maximum transverse deflection. The bond-multiple plate model is motivated by the desire to extend the bending model to an arbitrary Poisson's ratio, so the obvious test for this model is the same as for the bond-pair model. When compared to analytical predictions, fig. 6.25 demonstrates the

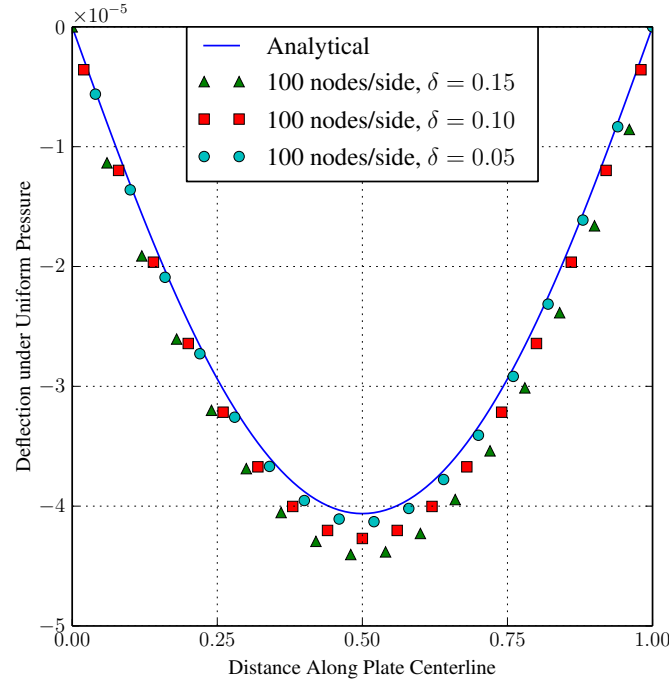


Figure 6.21: The Bond-Pair Model Converges on Accurate Plate Deflection with Smaller Horizons

bond-multiple model's ability to simulate plates with Poisson's ratios that depart significantly from the bond-pair limitation of $\nu = 1/3$.

Unlike the brittle beam, failure in a brittle plate need not progress unstably. To demonstrate the behavior of this model, a controlled-displacement double-torsion fracture test was simulated with the bond-pair model using a critical strain $\varepsilon_c = 0.001$. A good review of the double-torsion test is available in [63]. Figure 6.26 shows the setup of a double torsion fracture test. This test is particularly useful because it results in a bending crack whose growth is not unstable. The two sides of the cracked plate act as torsion springs; as the crack grows longer, the torsion springs grow longer as well, and correspondingly softer. The overall result is that, even though the plate's resistance to bending decreases as the crack grows, growth is stable until the crack nears the far side of the plate. The simple qualitative results are shown in fig. 6.27, colored by the fraction of failed bond pairs around each node. For each successive displacement load, the stable progression of the damaged region extends further into the plate. The relationship between load displacement

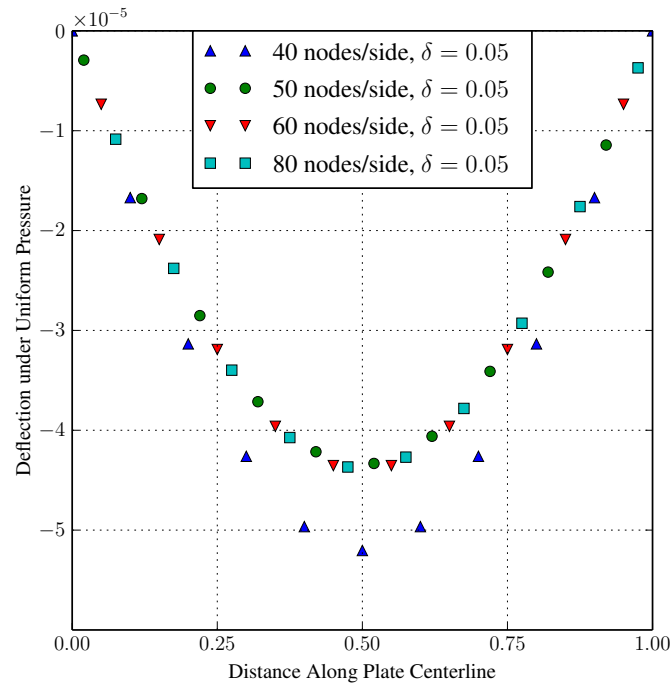


Figure 6.22: Horizon Must Include Sufficient Nodes

and crack length is consistent with a plane-stress mode I fracture toughness around $17\text{GPa}\sqrt{\text{m}}$. As with the brittle beam, the region within one horizon of the crack shows partial damage.

In the double-torsion plate, the crack is expected to progress straight across the plate. A more interesting failure pattern can be found if the displacement is applied to only one of the two sides of the pre-crack. In a “single torsion” cracked plate, the crack path is expected to curve, and this result can be seen in fig. 6.28.

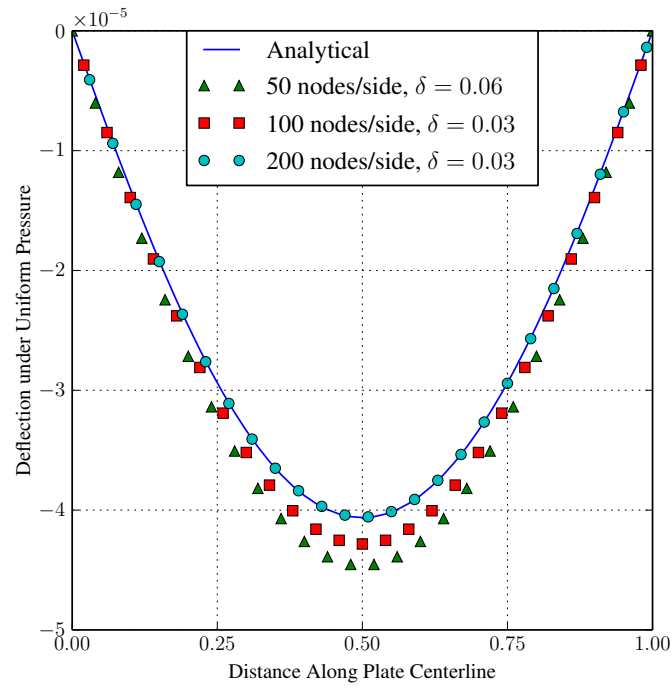


Figure 6.23: The Bond-Pair Model Converges on Accurate Plate Deflection with Finer Discretization

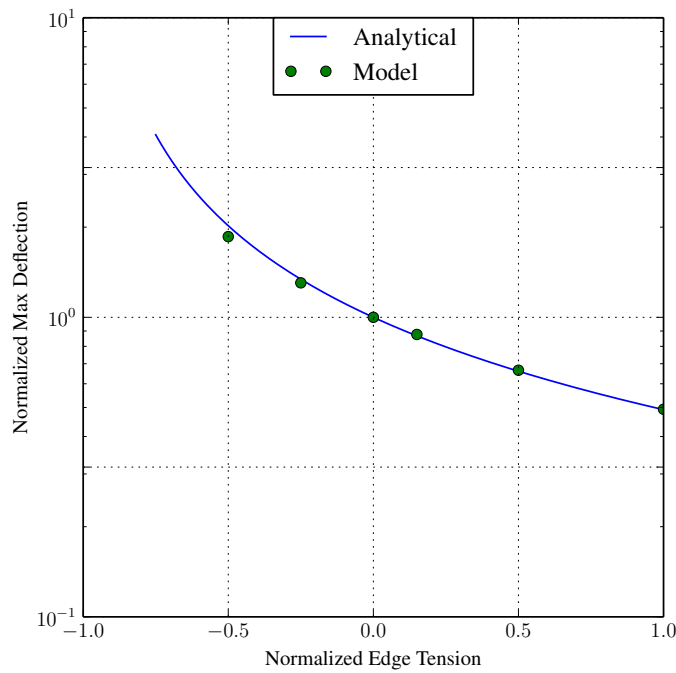


Figure 6.24: The Combined Model Accurately Captures the Influence of In-Plane Tension

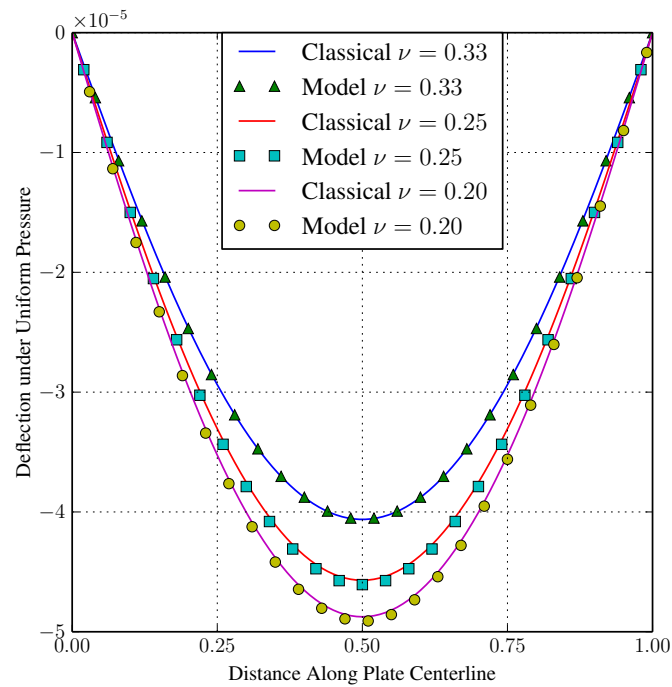


Figure 6.25: The Extended Model Matches for Arbitrary Poisson's Ratio

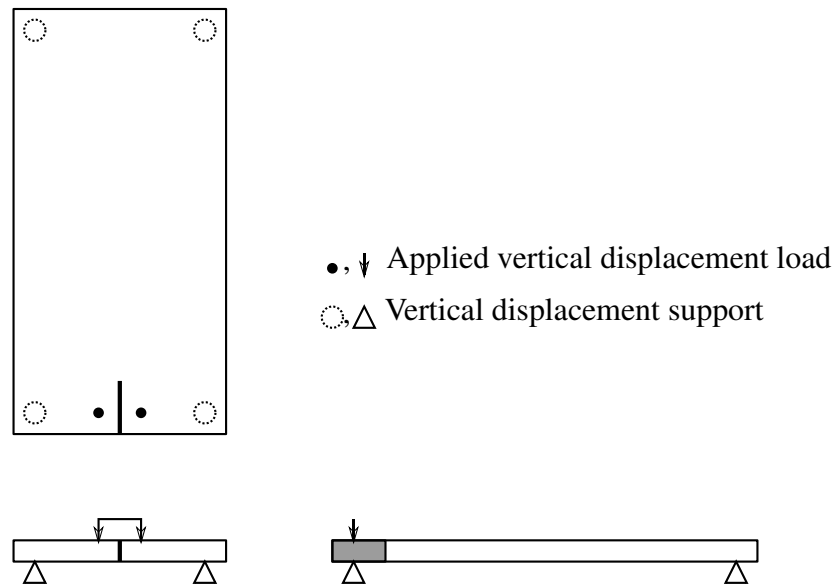


Figure 6.26: Simple Double Torsion Setup

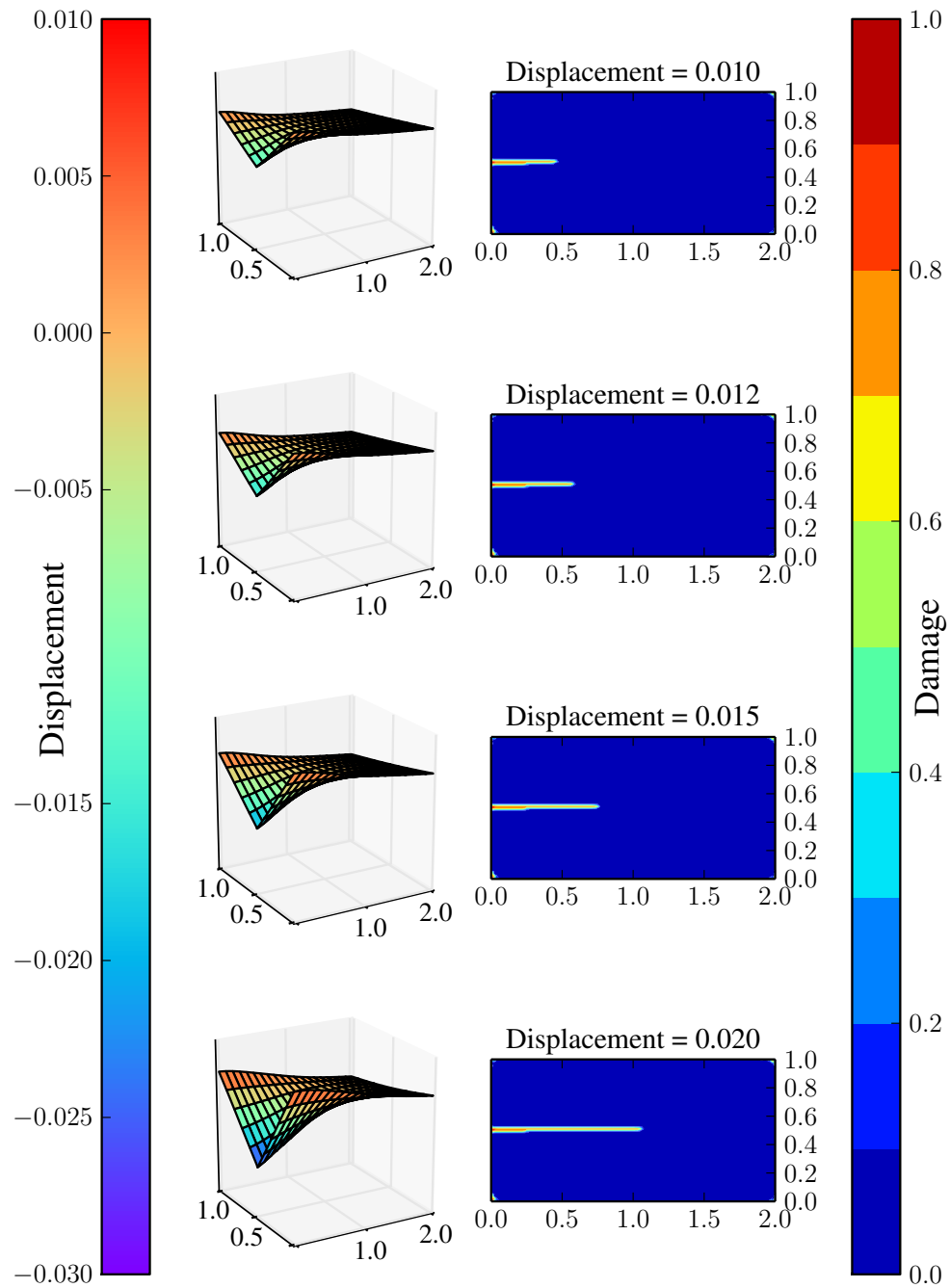


Figure 6.27: Crack Progression in Double Torsion Brittle Plate

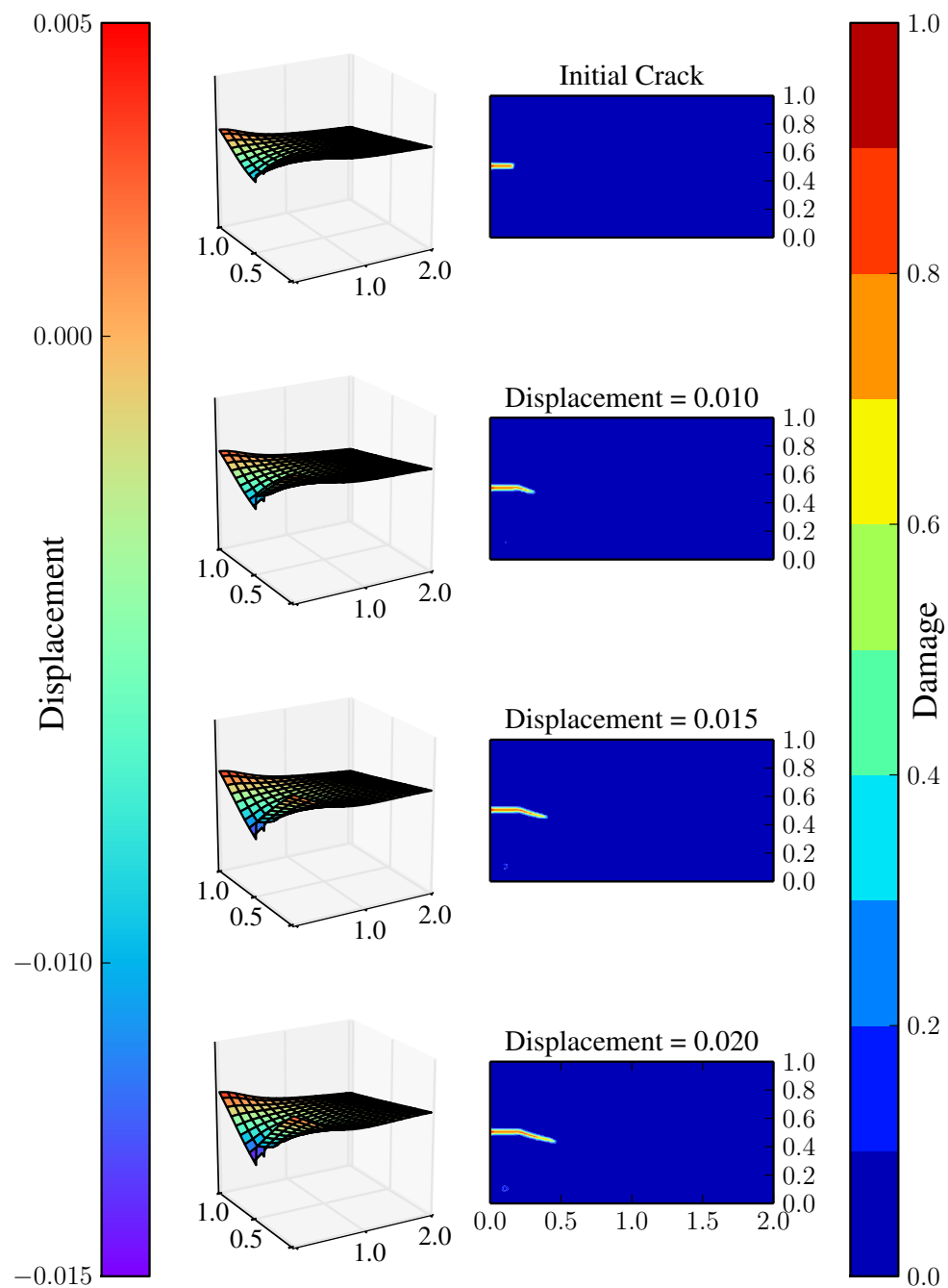


Figure 6.28: Crack Progression in Single Torsion Brittle Plate

6.6.3 Irregular Discretization Results

While it is simple to discretize the shapes examined thus far so that bonds pair up nicely, that is tougher to do for most shapes we are interested in analyzing. To combine the analytical simplicity of the previous shapes with a demonstration of the ability to handle irregular shapes, we discretize simple shapes in an irregular fashion. The first is a return to the simply-supported beam under uniform load. Figure 6.29 shows that the irregularly-discretized beam has the same deflection under uniform load as the regular discretization.

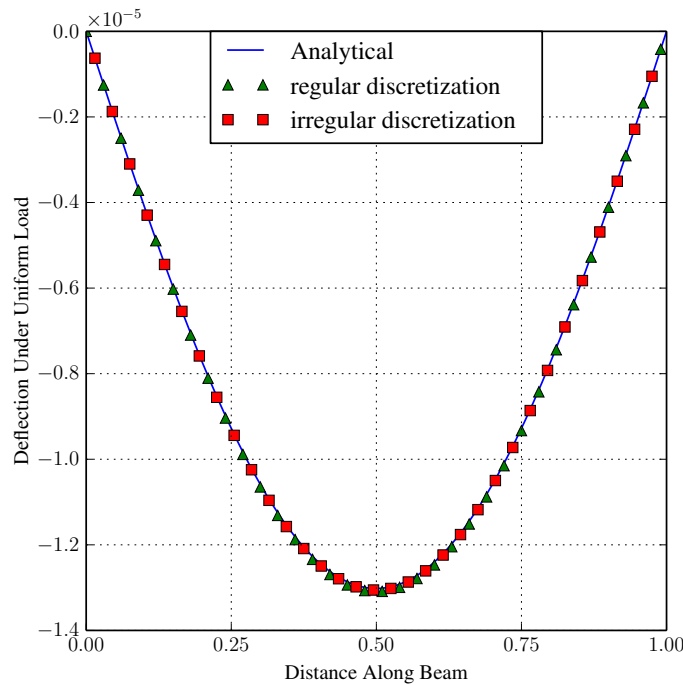


Figure 6.29: Irregular Beam

An example of a regularly-discretized plate is shown in fig. 6.30, while an irregularly discretized plate is shown in fig. 6.31. To use this plate in a peridynamic simulation, we reduce each element to a single node at the element's centroid with volume equal to the volume of the element.

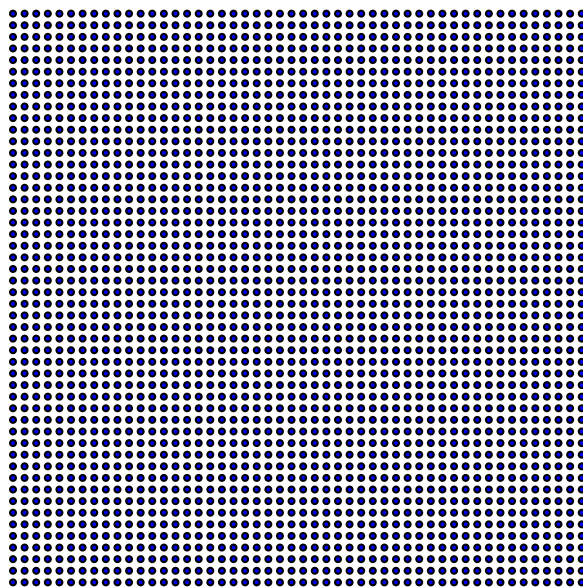


Figure 6.30: The regular plate discretization allows pairing of opposite bonds between nodes

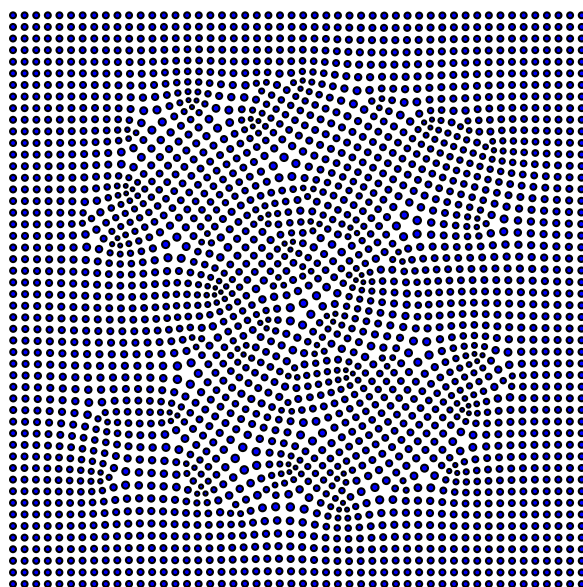


Figure 6.31: The irregular plate discretization requires virtual points to form bond pairs

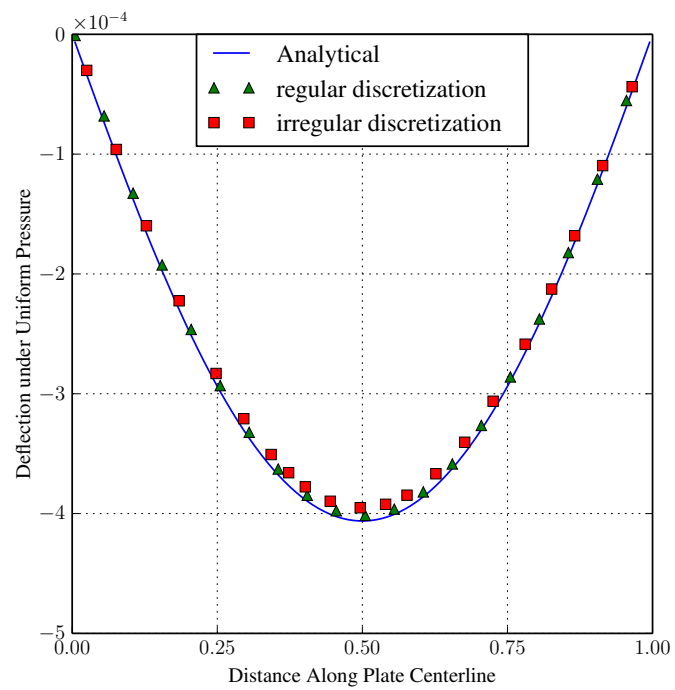


Figure 6.32: Virtual Points Allow for Irregular Discretizations

6.6.4 Curved Surface Results

To test the virtual point method for curved surfaces, we start with the simple case illustrated in fig. 6.33 of a ring in bending with a beam cross section. Like the straight beam, the curved beam is 0.01m in both width and thickness, with shear modulus $k = 37.5\text{Gpa}$ and Poisson's ratio $\nu = 1/3$. This 1m-diameter ring is subjected to a point load of 0.0833N. A real-life example of this type of problem would be a proving ring used for force measurements. The plots in figs. 6.34

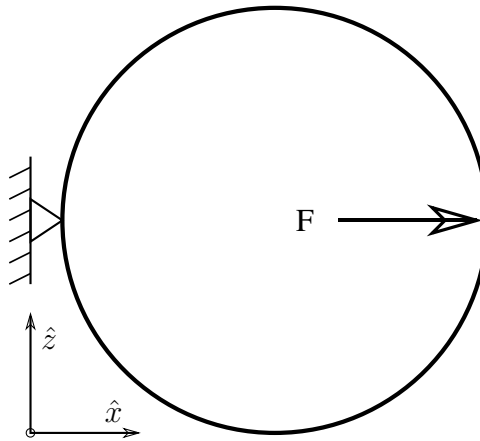


Figure 6.33: Proving Ring Setup

and 6.35 show that convergence to the classical elastic solution is more a function of the shrinking horizon size than of denser discretization, though the discretization must be dense enough to allow sufficient nodes in each neighborhood.

Similarly, the use of virtual points in the simulation of curved plates and shells can be examined by starting with the ring model depicted in fig. 6.36. This ring is 1m in diameter, 0.01m thick, and 0.25m wide. The ring is loaded in the same manner as the beam-based ring, but with a line load with total magnitude 937.5N. In cross-section, the ring looks like fig. 6.33.

Figure 6.37 demonstrates that, as with the curved beam, the curved shell requires a dense discretization to model. This is mostly as a consequence of requiring a small horizon. Surfaces with less curvature are less constrained.

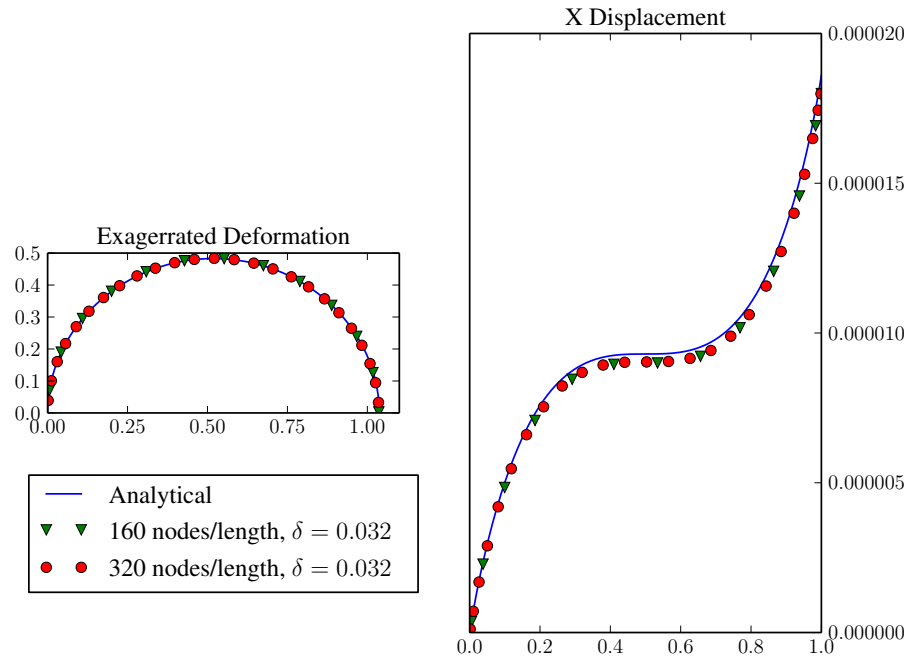


Figure 6.34: A Beam-based Proving Ring in Varying Discretizations

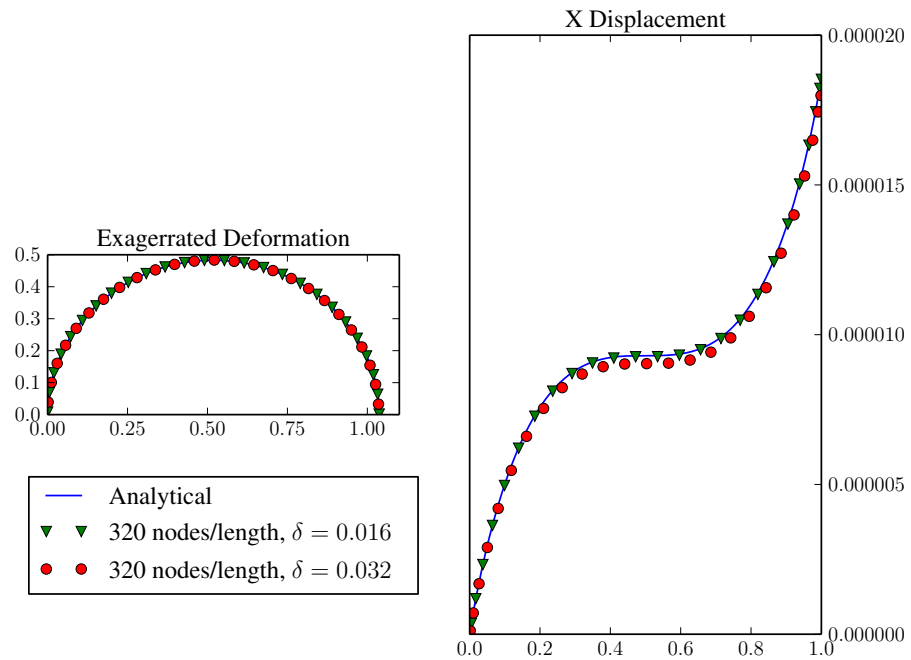


Figure 6.35: Horizon Convergence in the Beam-based Proving Ring



Figure 6.36: Discretization of a 3D Proving Ring

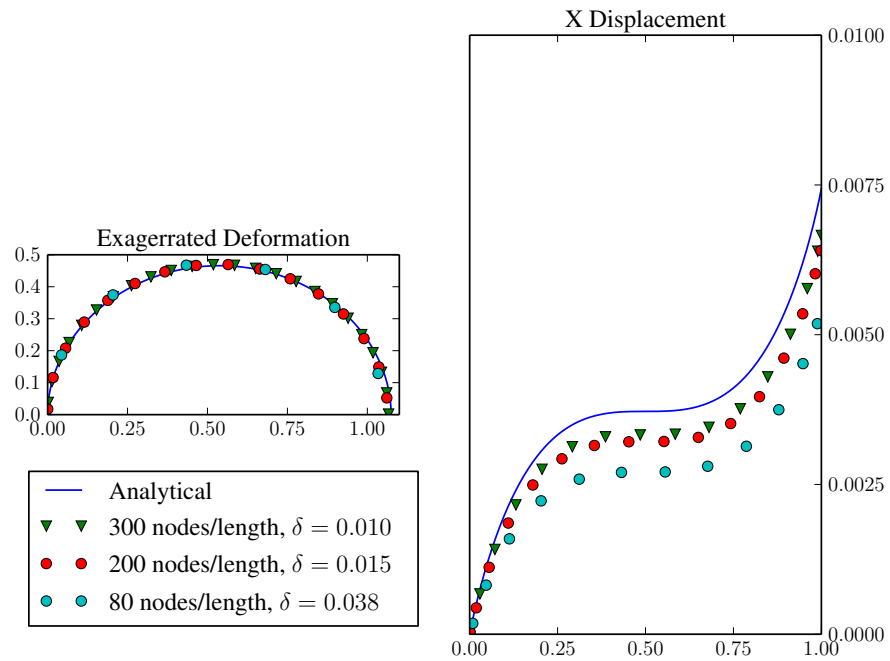


Figure 6.37: Plate-based Proving Ring

Chapter 7: CONCLUSION

This work develops what we believe to be the first state-based peridynamic thin feature models. These models allow for the simulation of bending in peridynamic beams, plates, and shells. They are verified by comparing their strain energies to the strain energy of classical models for small homogenous deformations, which are matched for both Euler-Bernoulli beams and for Kirchhoff-Love plates as the peridynamic horizon approaches zero. In addition to matching linear elastic models for these structures, it has been shown that the peridynamic models also match with Eringen-style gradient elasticity as the horizon decreases.

The bond-pair version of the bending model resists only bending deformation and is limited to plates with Poisson's ratios $\nu = 1/3$. To simulate loading incorporating forces both in-plane and transverse to the beam or plate, the pure bending model was combined with a conventional peridynamic model for in-plane deformation. The result is a hybrid bending-extension model. The Poisson's ratio limitation was overcome by decomposing bending deformation into isotropic and deviatoric components, allowing for a bond-multiple isotropic bending correction to the deformation energy. With this correction, the deformation energy was shown to match that of a Kirchhoff-Love plate for any (valid) Poisson's ratio.

To further extend the utility of the model, a reformulation was developed to gracefully include curved and irregularly discretized areas. By adding virtual points at locations where no nodes is present, the bond-pair model can be applied to regions where bonds are not initially organized into equal and opposite pairs. This includes curved surfaces, where a virtual point may be added slightly above or below the surface, as well as irregularly discretized regions in which virtual points may be added between peridynamic nodes.

Code was written to evaluate both beam and plate models for a variety of support configurations, load configurations, and materials. Although many problems of interest result in purely transverse deformation, both mathematical models and computer code are fully 3D. The nature of peridynamic models results in large but easily parallelizable problems. The code was writ-

ten with this in mind, and scales easily to large problems on multiple machines. Simulations run with the developed models provide results in agreement with conventional methods for several support configurations, including simply-supported, clamped, and free end conditions. Good agreement was also reached for applied displacements, moments, and both point and distributed loading conditions. The proposed damage model successfully reproduces the impact of nonlinear elasticity on deformation of a rectangular beam, and the framework is laid to allow application of the same model to a variety of beam cross sections. Brittle fracture results for both beam and plate simulations are also consistent with expectation. A single-torsion plate demonstrates the peridynamic advantages of natural crack path development without the need to predict direction of propagation. The hybrid bending-extension model resists transverse, in-plane, and combined deformation, allowing it to successfully reproduce the stiffening effect of adding in-plane tension to a transversely-loaded plate. With the bond-multiple correction, the extended model demonstrated the effect of varying Poisson's ratio on plate bending. Because it was inspired by a similar decomposition used in extension models, the same procedure can be used for combined in-plane and transverse deformations. Implementation of the virtual point extension greatly increases the practical utility of the model, a fact demonstrated by accurate simulations of the displacements of irregularly discretized plates and beams. Finally, the addition of virtual points allows application to curved features, as demonstrated by successful simulation of beam and plate based rings.

The state-based nature of these models allows them to resist bending as a basic deformation mode, in a way that is fundamentally different from previous peridynamic models, both 3D solid and thin-feature. While the examples in this work focus on conventional elastic and inelastic behavior, treating bending as a basic deformation opens the possibility of modeling thin features whose resistance to bending is not simply a function of stresses that vary through the thickness to produce a moment, and suggests a wide variety of possible applications: Graphene sheets are only one atom thick, so their bending behavior cannot be the result of through-thickness variation in stress. Some biological membranes resist isotropic bending but not deviatoric stresses. Highly-structured metamaterials may also have bending properties that cannot be derived solely from bulk

solid properties.

Peridynamic modeling is a technique that is swiftly growing in popularity, especially among those concerned with the propagation of material failure. The bending behavior of thin features is a critical part of many engineering analyses that has been largely out of reach for reasonably-sized peridynamic models. These peridynamic bending models extend the domain of problems to which peridynamic modeling can be applied.

There are many directions in which the models developed in this work can be improved upon. While the results presented here are both illustrative and persuasive, they do not represent a mathematically rigorous demonstration of the convergence properties of the bending models, and future work focusing specifically on discretization and convergence issues would be valuable. Both the plastic and brittle material models developed in this work are proofs of concepts, demonstrating the capabilities of peridynamics and the new bending models. It will be necessary to develop a thermodynamically consistent failure model before using this model to make predictions regarding failure propagation, especially when rapid progression is expected. Ideally, the material parameters of such a model could be determined from existing datasets and material parameters.

Because directional composites are a popular material choice for thin features, it would be worthwhile to extend the bending models to simulate non-isotropic plates. Other useful avenues of inquiry include combining these 2D models with peridynamic solid models to analyze features comprised of both thick and thin parts.

Appendix A: FRÉCHET DERIVATIVE

A.1 Definition

The derivative of a function of a state is defined by Silling in [66] as follows:

Let Ψ be a function of a state, $\Psi(\cdot) : \mathcal{A}_m \rightarrow \mathcal{L}_n$. Suppose there exists a state-valued function denoted $\nabla\Psi \in \mathcal{A}_{m+n}$ such that for any $\underline{\mathbf{A}} \in \mathcal{A}_m$ and any $\Delta\underline{\mathbf{A}} \in \mathcal{A}_m$,

$$\Psi(\underline{\mathbf{A}} + \Delta\underline{\mathbf{A}}) = \Psi(\underline{\mathbf{A}}) + \nabla\Psi(\underline{\mathbf{A}}) \bullet \Delta\underline{\mathbf{A}} + o(||\Delta\underline{\mathbf{A}}||). \quad (\text{A.1})$$

Then Ψ is said to be *differentiable* and $\nabla\Psi$ is called the *Frechet derivative* of Ψ .

This is a fairly straightforward way of defining a derivative with respect to a state. Because the force vector-state and deformation vector-state are work conjugate, the force vector-state can be determined by taking the Fréchet derivative of energy with respect to the deformation vector-state.

A.2 Bond-Pair Force

For the bond-pair model, we derive the bond force function from the bond-pair energy function

$$\begin{aligned} \underline{\mathbf{T}}\langle\xi\rangle &= \nabla w(\underline{\mathbf{Y}}\langle\xi\rangle) \\ w &= \omega(\xi) \alpha \left[1 + \cos\left(\theta\left(\underline{\mathbf{Y}}\langle\xi\rangle, \underline{\mathbf{Y}}\langle-\xi\rangle\right)\right) \right] \\ w(\underline{\mathbf{Y}}\langle\xi\rangle + \Delta\underline{\mathbf{Y}}\langle\xi\rangle) &= \omega(\xi) \alpha \left[1 + \cos\left(\theta\left(\underline{\mathbf{Y}}\langle\xi\rangle + \Delta\underline{\mathbf{Y}}\langle\xi\rangle, \underline{\mathbf{Y}}\langle-\xi\rangle\right)\right) \right] \\ \nabla w(\underline{\mathbf{Y}}\langle\xi\rangle) \bullet \Delta\underline{\mathbf{Y}}\langle\xi\rangle &= w(\underline{\mathbf{Y}}\langle\xi\rangle + \Delta\underline{\mathbf{Y}}\langle\xi\rangle) - w(\underline{\mathbf{Y}}\langle\xi\rangle) \\ &= \omega(\xi) \alpha \sin\left(\theta\left(\underline{\mathbf{Y}}\langle\xi\rangle, \underline{\mathbf{Y}}\langle-\xi\rangle\right)\right) \left[\theta\left(\underline{\mathbf{Y}}\langle\xi\rangle + \Delta\underline{\mathbf{Y}}\langle\xi\rangle, \underline{\mathbf{Y}}\langle-\xi\rangle\right) - \theta\left(\underline{\mathbf{Y}}\langle\xi\rangle, \underline{\mathbf{Y}}\langle-\xi\rangle\right) \right] \\ \left[\theta\left(\underline{\mathbf{Y}}\langle\xi\rangle + \Delta\underline{\mathbf{Y}}\langle\xi\rangle, \underline{\mathbf{Y}}\langle-\xi\rangle\right) - \theta\left(\underline{\mathbf{Y}}\langle\xi\rangle, \underline{\mathbf{Y}}\langle-\xi\rangle\right) \right] &= \frac{\Delta\underline{\mathbf{Y}}\langle\xi\rangle}{|\underline{\mathbf{Y}}\langle\xi\rangle|} \bullet \hat{\theta}\left(\underline{\mathbf{Y}}\langle\xi\rangle, \underline{\mathbf{Y}}\langle-\xi\rangle\right) \end{aligned}$$

To determine the $\hat{\theta}$ direction vector, we must construct a vector that is normal to $\underline{\mathbf{Y}}\langle\xi\rangle$ and that is in the plane containing both $\underline{\mathbf{Y}}\langle\xi\rangle$ and $\underline{\mathbf{Y}}\langle-\xi\rangle$. The cross product of $\underline{\mathbf{Y}}\langle\xi\rangle$ and $\underline{\mathbf{Y}}\langle-\xi\rangle$ is a vector normal to that plane, so any vector normal to that cross product will be in the correct plane. Therefore, the vector $\underline{\mathbf{Y}}\langle\xi\rangle \times [\underline{\mathbf{Y}}\langle\xi\rangle \times \underline{\mathbf{Y}}\langle-\xi\rangle]$ is both normal to $\underline{\mathbf{Y}}\langle\xi\rangle$ and is in the plane containing both $\underline{\mathbf{Y}}\langle\xi\rangle$ and $\underline{\mathbf{Y}}\langle-\xi\rangle$. Normalizing gives us the $\hat{\theta}$ direction vector:

$$\hat{\theta}(\underline{\mathbf{Y}}\langle\xi\rangle, \underline{\mathbf{Y}}\langle-\xi\rangle) = \frac{\underline{\mathbf{Y}}\langle\xi\rangle \times [\underline{\mathbf{Y}}\langle\xi\rangle \times \underline{\mathbf{Y}}\langle-\xi\rangle]}{|\underline{\mathbf{Y}}\langle\xi\rangle||\underline{\mathbf{Y}}\langle\xi\rangle||\underline{\mathbf{Y}}\langle-\xi\rangle|\sin(\theta(\underline{\mathbf{Y}}\langle\xi\rangle, \underline{\mathbf{Y}}\langle-\xi\rangle))}$$

We combine all of these to get the expression for bond force found in eq. (5.1).

$$\underline{\mathbf{T}}\langle\xi\rangle = \omega(\xi) \frac{-\alpha}{|\underline{\mathbf{Y}}\langle\xi\rangle||\underline{\mathbf{Y}}\langle\xi\rangle|} \times \left[\frac{\underline{\mathbf{Y}}\langle\xi\rangle}{|\underline{\mathbf{Y}}\langle\xi\rangle|} \times \frac{\underline{\mathbf{Y}}\langle-\xi\rangle}{|\underline{\mathbf{Y}}\langle-\xi\rangle|} \right]$$

A.3 Isotropic Bending Correction

To derive the bending “pressure” force, we start with the isotropic energy discrepancy

$$W^* = 2\mu \frac{h^3}{12} \frac{3\nu - 1}{1 - \nu} \bar{\kappa}^2.$$

with

$$\begin{aligned} \bar{\kappa}(\underline{\mathbf{Y}}) &= \frac{1}{m} \int_0^\delta \int_0^{2\pi} \omega(\xi) \frac{\underline{\mathbf{Y}}\langle\xi\rangle + \underline{\mathbf{Y}}\langle-\xi\rangle}{\xi^2} \xi d\phi d\xi \\ &= \frac{2}{m} \int_0^\delta \int_0^{2\pi} \omega(\xi) \frac{\underline{\mathbf{Y}}\langle\xi\rangle}{\xi^2} \xi d\phi d\xi \end{aligned}$$

Because $\bar{\kappa}$ is itself a vector-state, we will need to begin with the change in $\bar{\kappa}$ with respect to $\underline{\mathbf{Y}}$ and carry the result through to find the change in W^* .

$$\begin{aligned}\bar{\kappa}(\underline{\mathbf{Y}} + \Delta \underline{\mathbf{Y}}) &= \frac{2}{m} \int_0^\delta \int_0^{2\pi} \omega(\xi) \frac{\underline{\mathbf{Y}}\langle \xi \rangle + \Delta \underline{\mathbf{Y}}\langle \xi \rangle}{\xi^2} \xi d\phi d\xi \\ &= \bar{\kappa}(\underline{\mathbf{Y}}) + \frac{2}{m} \int_0^\delta \int_0^{2\pi} \omega(\xi) \frac{\Delta \underline{\mathbf{Y}}\langle \xi \rangle}{\xi^2} \xi d\phi d\xi\end{aligned}$$

$$\begin{aligned}W^*(\underline{\mathbf{Y}} + \Delta \underline{\mathbf{Y}}) &= 2\mu \frac{h^3}{12} \frac{3\nu - 1}{1 - \nu} [\bar{\kappa}(\underline{\mathbf{Y}} + \Delta \underline{\mathbf{Y}})]^2 \\ &= 2\mu \frac{h^3}{12} \frac{3\nu - 1}{1 - \nu} \left\{ \bar{\kappa}(\underline{\mathbf{Y}}) \cdot \bar{\kappa}(\underline{\mathbf{Y}}) \right. \\ &\quad \left. + \frac{4}{m} \int_0^\delta \int_0^{2\pi} \omega(\xi) \frac{\Delta \underline{\mathbf{Y}}\langle \xi \rangle \cdot \bar{\kappa}(\underline{\mathbf{Y}})}{\xi^2} \xi d\phi d\xi \right. \\ &\quad \left. + \frac{2}{m} \int_0^\delta \int_0^{2\pi} \omega(\xi) \frac{\Delta \underline{\mathbf{Y}}\langle \xi \rangle \cdot \Delta \underline{\mathbf{Y}}\langle \xi \rangle}{\xi^2} \xi d\phi d\xi \right\} \\ &= W^*(\underline{\mathbf{Y}}) + 2\mu \frac{h^3}{12} \frac{3\nu - 1}{1 - \nu} \frac{4}{m} \frac{\omega(\xi)}{\xi^2} \bar{\kappa}(\underline{\mathbf{Y}}) \bullet \Delta \underline{\mathbf{Y}} + o(||\Delta \underline{\mathbf{Y}}||) \\ \nabla W^*(\underline{\mathbf{Y}}) &= \underline{\mathbf{T}}^*\langle \xi \rangle = \frac{8\mu}{m} \frac{h^3}{12} \frac{3\nu - 1}{1 - \nu} \frac{\omega(\xi)}{\xi^2} \bar{\kappa}\end{aligned}$$

This demonstrates the bond-length dependent “pressure” applied to each point in the neighborhood of a point with average curvature $\bar{\kappa}$.

Appendix B: NOTATION

Peridynamics is a new field, and different authors use a variety of notations to represent a variety of concepts. Although chosen to be as consistent as possible with other authors, the following notation is therefore not portable to other works.

Table B.1: Peridynamic Notation

Notation	Meaning
A	area
b	beam width
\mathbf{b}	body force vector
c	bond stiffness
D	plate flexural rigidity
E	Young's modulus
\underline{e}	bond stretch
\underline{e}^i	isotropic portion of bond stretch
\underline{e}^d	deviatoric portion of bond stretch
F	applied force
\mathbf{F}	deformation gradient tensor
$\bar{\mathbf{F}}$	approximated deformation gradient tensor
\mathbf{f}	force vector
f^{iso}	isotropic bending “pressure”
\mathcal{H}	neighborhood
I	second moment of area
K	Eringen's nonlocal modulus
k	bulk modulus
\mathbf{K}	shape tensor

Table B.1: Continued

Notation	Meaning
l	beam length represented by node (1D)
M	moment
m	peridynamic normalization constant
\mathcal{O}	order notation
p	pressure
p	distributed pressure load (2D)
\mathbf{P}	first Piola-Kirchhoff stress tensor
$\mathbf{p}, \mathbf{q}, \mathbf{r}$	deformed bond vectors
q	distributed load (1D)
s	bond stretch
t	thickness
\mathbf{t}	Eringen nonlocal stress
t_{1D}	1D Eringen nonlocal stress
$\underline{\mathbf{T}}$	force vector state
$\underline{\mathbf{T}}^*$	correction force vector state
\mathbf{u}	displacement vector
V	shear force
v	displacement in \hat{y} direction
w	displacement in \hat{z} direction
w	bond energy, bond-pair energy
W	strain or deformation energy density
W^*	energy discrepancy
$\hat{x}, \hat{y}, \hat{z}$	coordinate vectors
\mathbf{x}, \mathbf{q}	undeformed location vectors

Table B.1: Continued

Notation	Meaning
\mathbf{y}	deformed location vector
\mathbf{Y}	deformation vector state
α	peridynamic bending stiffness
α^{iso}	isotropic bending stiffness
δ	horizon
Δx	distance between nodes in regular discretization
ϵ	uniaxial strain
$\boldsymbol{\epsilon}$	strain tensor
ϵ_c	critical strain
ϵ^d	deviatoric strain
θ	bond-pair angle
θ_c	critical angle
θ_{3D}, θ_{2D}	dilation
κ	beam curvature
$\bar{\kappa}$	nonlocal curvature
$\bar{\boldsymbol{\kappa}}$	vector isotropic curvature
$\kappa_x = \kappa_{xx} = \kappa_1 = \frac{\partial^2 w}{\partial x^2}$	Plate Curvatures
$\kappa_y = \kappa_{yy} = \kappa_2 = \frac{\partial^2 w}{\partial y^2}$	
$\kappa_{xy} = \kappa_3 = \frac{\partial^2 w}{\partial x \partial y}$	
μ	shear modulus
ν	Poisson's ratio
$\boldsymbol{\xi}, \boldsymbol{\zeta}$	undeformed bond vectors
$\boldsymbol{\xi}_i$	i -th of n vectors $\boldsymbol{\xi}_1$ to $\boldsymbol{\xi}_n$
ξ_i	i -th component of vector $\boldsymbol{\xi}$

Table B.1: Continued

Notation	Meaning
ξ	magnitude of vector ξ
ρ	density
ρ	radius of curvature
σ_{1D}	1D local stress
σ	Cauchy stress tensor
(τl)	scale parameter
ϕ	beam deflection angle
ϕ	bond orientation angle
Ω	undeformed body
Ω	classical strain energy density function
ω	weight function

BIBLIOGRAPHY

- [1] R Ansari, S Sahmani, and B Arash. Nonlocal plate model for free vibrations of single-layered graphene sheets. *Physics Letters A*, 375(1):53–62, 2010.
- [2] Douglas N Arnold. An interior penalty finite element method with discontinuous elements. *SIAM journal on numerical analysis*, 19(4):742–760, 1982.
- [3] E. Askari, F. Bobaru, RB Lehoucq, ML Parks, SA Silling, and O. Weckner. Peridynamics for multiscale materials modeling. In *Journal of Physics: Conference Series*, volume 125, page 012078. IOP Publishing, 2008.
- [4] Zdenek P Bazant and Ta-Peng Chang. Nonlocal finite element analysis of strain-softening solids. *Journal of engineering mechanics*, 113(1):89–105, 1987.
- [5] Zdenek P Bazant and Gilles Pijaudier-Cabot. Nonlocal continuum damage, localization instability and convergence. *Journal of Applied Mechanics*, 55(2):287–293, 1988.
- [6] Ted Belytschko and Tom Black. Elastic crack growth in finite elements with minimal remeshing. *International journal for numerical methods in engineering*, 45(5):601–620, 1999.
- [7] W Benz and E Asphaug. Simulations of brittle solids using smooth particle hydrodynamics. *Computer physics communications*, 87(1):253–265, 1995.
- [8] Florin Bobaru. Influence of van der waals forces on increasing the strength and toughness in dynamic fracture of nanofibre networks: a peridynamic approach. *Modelling and Simulation in Materials Science and Engineering*, 15(5):397, 2007.
- [9] Florin Bobaru and Monchai Duangpanya. The peridynamic formulation for transient heat conduction. *International Journal of Heat and Mass Transfer*, 53(19):4047–4059, 2010.

- [10] Nathaniel Burch and Richard Lehoucq. Classical, nonlocal, and fractional diffusion equations on bounded domains. *International Journal for Multiscale Computational Engineering*, 9(6), 2011.
- [11] J Burghardt, R Brannon, and J Guilkey. A nonlocal plasticity formulation for the material point method. *Computer Methods in Applied Mechanics and Engineering*, 225:55–64, 2012.
- [12] N Challamel and C M Wang. The small length scale effect for a non-local cantilever beam: a paradox solved. *Nanotechnology*, 19(34):345703, 2008.
- [13] RJ Cheng and Kim Meow Liew. Analyzing two-dimensional sine–gordon equation with the mesh-free reproducing kernel particle ritz method. *Computer methods in applied mechanics and engineering*, 245:132–143, 2012.
- [14] Gianluca Cusatis, Andrea Mencarelli, Daniele Pelessone, and James Baylot. Lattice discrete particle model (ldpm) for failure behavior of concrete. ii: Calibration and validation. *Cement and Concrete Composites*, 33(9):891–905, 2011.
- [15] Gianluca Cusatis, Daniele Pelessone, and Andrea Mencarelli. Lattice discrete particle model (ldpm) for failure behavior of concrete. i: Theory. *Cement and Concrete Composites*, 33(9):881–890, 2011.
- [16] Kaushik Dayal and Kaushik Bhattacharya. Kinetics of phase transformations in the peridynamic formulation of continuum mechanics. *Journal of the Mechanics and Physics of Solids*, 54(9):1811–1842, 2006.
- [17] Paul N Demmie and Stewart A Silling. An approach to modeling extreme loading of structures using peridynamics. *Journal of Mechanics of Materials and Structures*, 2(10):1921–1945, 2007.

- [18] John Dolbow, Nicolas Moës, and Ted Belytschko. Modeling fracture in mindlin–reissner plates with the extended finite element method. *International Journal of Solids and Structures*, 37(48):7161–7183, 2000.
- [19] WH Duan and CM Wang. Exact solutions for axisymmetric bending of micro/nanoscale circular plates based on nonlocal plate theory. *Nanotechnology*, 18(38):385704, 2007.
- [20] Etienne Emmrich and Olaf Weckner. Analysis and numerical approximation of an integro-differential equation modeling non-local effects in linear elasticity. *Mathematics and Mechanics of Solids*, 12(4):363–384, 2007.
- [21] A Cemal Eringen. On differential equations of nonlocal elasticity and solutions of screw dislocation and surface waves. *Journal of Applied Physics*, 54(9):4703–4710, 1983.
- [22] A.C. Eringen and DGB Edelen. On nonlocal elasticity. *International Journal of Engineering Science*, 10(3):233–248, 1972.
- [23] XJ Fang, QD Yang, BN Cox, and ZQ Zhou. An augmented cohesive zone element for arbitrary crack coalescence and bifurcation in heterogeneous materials. *International Journal for Numerical Methods in Engineering*, 88(9):841–861, 2011.
- [24] Thomas M Fischer. Bending stiffness of lipid bilayers. iii. gaussian curvature. *Journal de Physique II*, 2(3):337–343, 1992.
- [25] John Foster, Stewart A. Silling, and Weinong Chen. An energy based failure criterion for use with peridynamic states. *International Journal for Multiscale Computational Engineering*, 9(6):675–988, 2011.
- [26] JT Foster, SA Silling, and WW Chen. Viscoplasticity using peridynamics. *International Journal for Numerical Methods in Engineering*, 81(10):1242–1258, 2010.

- [27] JW Foulk, DH Allen, and KLE Helms. Formulation of a three-dimensional cohesive zone model for application to a finite element algorithm. *Computer methods in applied mechanics and engineering*, 183(1):51–66, 2000.
- [28] Thomas-Peter Fries and Ted Belytschko. The extended/generalized finite element method: an overview of the method and its applications. *International Journal for Numerical Methods in Engineering*, 84(3):253–304, 2010.
- [29] Walter Gerstle, Nicolas Sau, and Stewart Silling. Peridynamic modeling of concrete structures. *Nuclear engineering and design*, 237(12):1250–1258, 2007.
- [30] PC Guan, JS Chen, Y Wu, H Teng, J Gaidos, K Hofstetter, and M Alsaleh. Semi-lagrangian reproducing kernel formulation and application to modeling earth moving operations. *Mechanics of Materials*, 41(6):670–683, 2009.
- [31] PC Guan, SW Chi, JS Chen, TR Slawson, and MJ Roth. Semi-lagrangian reproducing kernel particle method for fragment-impact problems. *International Journal of Impact Engineering*, 38(12):1033–1047, 2011.
- [32] M Holl, S Loehnert, and P Wriggers. An adaptive multiscale method for crack propagation and crack coalescence. *International Journal for Numerical Methods in Engineering*, 93(1):23–51, 2013.
- [33] Michael J Hunsweck, Yongxing Shen, and Adrián J Lew. A finite element approach to the simulation of hydraulic fractures with lag. *International Journal for Numerical and Analytical Methods in Geomechanics*, 37(9):993–1015, 2013.
- [34] B. Kilic, A. Agwai, and E. Madenci. Peridynamic theory for progressive damage prediction in center-cracked composite laminates. *Composite Structures*, 90(2):141–151, 2009.
- [35] Bahattin Kilic and Erdogan Madenci. Prediction of crack paths in a quenched glass plate by using peridynamic theory. *International journal of fracture*, 156(2):165–177, 2009.

- [36] E. Kröner. Elasticity theory of materials with long range cohesive forces. *International Journal of Solids and Structures*, 3(5):731–742, 1967.
- [37] Shaofan Li, Wei Hao, and Wing Kam Liu. Numerical simulations of large deformation of thin shell structures using meshfree methods. *Computational Mechanics*, 25(2-3):102–116, 2000.
- [38] Weizhou Li and Thomas Siegmund. An analysis of crack growth in thin-sheet metal via a cohesive zone model. *Engineering Fracture Mechanics*, 69(18):2073–2093, 2002.
- [39] David John Littlewood. Simulation of dynamic fracture using peridynamics, finite element modeling, and contact. Technical report, Sandia National Laboratories, 2010.
- [40] Wing Kam Liu, Sukky Jun, and Yi Fei Zhang. Reproducing kernel particle methods. *International journal for numerical methods in fluids*, 20(8-9):1081–1106, 1995.
- [41] Éamonn Ó Máirtín, Guillaume Parry, Glenn E Beltz, and J Patrick McGarry. Potential-based and non-potential-based cohesive zone formulations under mixed-mode separation and over-closure—part ii: Finite element applications. *Journal of the Mechanics and Physics of Solids*, 63:363–385, 2014.
- [42] Bertrand Maurel and Alain Combescure. An sph shell formulation for plasticity and fracture analysis in explicit dynamics. *International journal for numerical methods in engineering*, 76(7):949–971, 2008.
- [43] J Patrick McGarry, Éamonn Ó Máirtín, Guillaume Parry, and Glenn E Beltz. Potential-based and non-potential-based cohesive zone formulations under mixed-mode separation and over-closure. part i: Theoretical analysis. *Journal of the Mechanics and Physics of Solids*, 63:336–362, 2014.

- [44] Jens Markus Melenk and Ivo Babuska. The partition of unity finite element method: basic theory and applications. *Computer methods in applied mechanics and engineering*, 139(1):289–314, 1996.
- [45] M Memar Ardestani, B Soltani, and Sh Shams. Analysis of functionally graded stiffened plates based on fsdt utilizing reproducing kernel particle method. *Composite Structures*, 112:231–240, 2014.
- [46] Y. Mikata. Analytical solutions of peristatic and peridynamic problems for a 1d infinite rod. *International Journal of Solids and Structures*, 2012.
- [47] J.A. Mitchell. A nonlocal, ordinary, state-based plasticity model for peridynamics. Technical report, Sandia National Laboratories, 2011.
- [48] John A Mitchell. A non-local, ordinary-state-based viscoelasticity model for peridynamics. Technical report, Tech. Report SAND2011-8064, Sandia National Laboratories, 2011.
- [49] Nicolas Moes, John Dolbow, and T Belytschko. A finite element method for crack growth without remeshing. *Int. J. Numer. Meth. Engng*, 46:131–150, 1999.
- [50] T Mohammadnejad and AR Khoei. Hydro-mechanical modeling of cohesive crack propagation in multiphase porous media using the extended finite element method. *International Journal for Numerical and Analytical Methods in Geomechanics*, 37(10):1247–1279, 2013.
- [51] Joe J Monaghan. Smoothed particle hydrodynamics. *Reports on progress in physics*, 68(8):1703, 2005.
- [52] John A Nairn. Material point method calculations with explicit cracks. *Computer Modeling in Engineering and Sciences*, 4(6):649–664, 2003.
- [53] A Needleman. A continuum model for void nucleation by inclusion debonding. *Journal of applied mechanics*, 54(3):525–531, 1987.

- [54] James O’Grady and John T Foster. Peridynamic beams: A non-ordinary, state-based model. *International Journal of Solids and Structures*, 51(18):3177–3183, September 2014.
- [55] James O’Grady and John T Foster. Peridynamic plates and flat shells: A non-ordinary, state-based model. *International Journal of Solids and Structures*, In Publication.
- [56] Michael Ortiz, Yves Leroy, and Alan Needleman. A finite element method for localized failure analysis. *Computer Methods in Applied Mechanics and Engineering*, 61(2):189–214, 1987.
- [57] Mario Di Paola, Giuseppe Failla, and Massimiliano Zingales. Mechanically based nonlocal euler-bernoulli beam model. *Journal of Nanomechanics and Micromechanics*, 4(1), 2014.
- [58] SC Pradhan and T Murmu. Small scale effect on the buckling of single-layered graphene sheets under biaxial compression via nonlocal continuum mechanics. *Computational Materials Science*, 47(1):268–274, 2009.
- [59] Junuthula Narasimha Reddy. *Theory and analysis of elastic plates and shells*. CRC press, 2007.
- [60] A. Sadeghirad, R. M. Brannon, and J. Burghardt. A convected particle domain interpolation technique to extend applicability of the material point method for problems involving massive deformations. *International Journal for Numerical Methods in Engineering*, 86(12):1435–1456, 2011.
- [61] M. Sala, W. Spitz, and M. Heroux. PyTrilinos: High-performance distributed-memory solvers for Python. *ACM Transactions on Mathematical Software (TOMS)*, 34(2), March 2008.
- [62] Henning Sauerland and Thomas-Peter Fries. The stable xfem for two-phase flows. *Computers & Fluids*, 87:41–49, 2013.

- [63] A Shyam and E Lara-Curzio. The double-torsion testing technique for determination of fracture toughness and slow crack growth behavior of materials: a review. *Journal of materials science*, 41(13):4093–4104, 2006.
- [64] S.A. Silling. Reformulation of elasticity theory for discontinuities and long-range forces. *Journal of the Mechanics and Physics of Solids*, 48(1):175–209, 2000.
- [65] S.A. Silling. A coarsening method for linear peridynamics. *International Journal for Multi-scale Computational Engineering*, 9(6):609, 2011.
- [66] SA Silling, M. Epton, O. Weckner, J. Xu, and E. Askari. Peridynamic states and constitutive modeling. *Journal of Elasticity*, 88(2):151–184, 2007.
- [67] SA Silling and RB Lehoucq. Peridynamic theory of solid mechanics. *Advances in Applied Mechanics*, 44:73–168, 2010.
- [68] Stewart A Silling and Ebrahim Askari. A meshfree method based on the peridynamic model of solid mechanics. *Computers & Structures*, 83(17):1526–1535, 2005.
- [69] STEWART A Silling, M Zimmermann, and R Abeyaratne. Deformation of a peridynamic bar. *Journal of Elasticity*, 73(1-3):173–190, 2003.
- [70] Stewart Andrew Silling and Florin Bobaru. Peridynamic modeling of membranes and fibers. *International Journal of Non-Linear Mechanics*, 40(2):395–409, 2005.
- [71] Volker Springel. Smoothed particle hydrodynamics in astrophysics. *Annual Review of Astronomy and Astrophysics*, 48:391–430, 2010.
- [72] Deborah Sulsky and Howard L Schreyer. Axisymmetric form of the material point method with applications to upsetting and taylor impact problems. *Computer Methods in Applied Mechanics and Engineering*, 139(1):409–429, 1996.
- [73] Michael Taylor and David J Steigmann. A two-dimensional peridynamic model for thin plates. *Mathematics and Mechanics of Solids*, 2013.

- [74] Stephen Timoshenko, Sergius Woinowsky-Krieger, and S Woinowsky. *Theory of plates and shells*, volume 2. McGraw-hill New York, 1959.
- [75] MR Tupek, JJ Rimoli, and R Radovitzky. An approach for incorporating classical continuum damage models in state-based peridynamics. *Computer Methods in Applied Mechanics and Engineering*, 2013.
- [76] R Vignjevic, N Djordjevic, S Gemkow, T De Vuyst, and J Campbell. Sph as a nonlocal regularisation method: Solution for instabilities due to strain-softening. *Computer Methods in Applied Mechanics and Engineering*, 277:281–304, 2014.
- [77] T.L. Warren, S.A. Silling, A. Askari, O. Weckner, M.A. Epton, and J. Xu. A non-ordinary state-based peridynamic method to model solid material deformation and fracture. *International Journal of Solids and Structures*, 46(5):1186–1195, 2009.
- [78] O. Weckner and R. Abeyaratne. The effect of long-range forces on the dynamics of a bar. *Journal of the Mechanics and Physics of Solids*, 53(3):705–728, 2005.
- [79] O. Weckner, G. Brunk, M.A. Epton, S.A. Silling, and E. Askari. Green’s functions in non-local three-dimensional linear elasticity. *Proceedings of the Royal Society A: Mathematical, Physical and Engineering Science*, 465(2111):3463–3487, 2009.
- [80] Z Wieckowski. The material point method in large strain engineering problems. *Computer methods in applied mechanics and engineering*, 193(39):4417–4438, 2004.
- [81] Youcai Wu, Joseph M Magallanes, and John E Crawford. Fragmentation and debris evolution modeled by a point-wise coupled reproducing kernel/finite element formulation. *International Journal of Damage Mechanics*, page 1056789514520797, 2014.
- [82] Yongning Xie and Gang Wang. A stabilized iterative scheme for coupled hydro-mechanical systems using reproducing kernel particle method. *International Journal for Numerical Methods in Engineering*, 2014.

- [83] J. Xu, A. Askari, O. Weckner, and S. Silling. Peridynamic analysis of impact damage in composite laminates. *Journal of Aerospace Engineering*, 21:187, 2008.
- [84] Jin Xu, Chi King Lee, and KH Tan. An xfem plate element for high gradient zones resulted from yield lines. *International Journal for Numerical Methods in Engineering*, 93(12):1314–1344, 2013.

AFOSR Deliverables Submission Survey

Response ID:6565 Data

1.

1. Report Type

Final Report

Primary Contact E-mail

Contact email if there is a problem with the report.

jtfoster@austin.utexas.edu

Primary Contact Phone Number

Contact phone number if there is a problem with the report

5124716972

Organization / Institution name

The University of Texas at Austin

Grant/Contract Title

The full title of the funded effort.

(YIP 13) - Predictive simulation of material failure using peridynamics

Grant/Contract Number

AFOSR assigned control number. It must begin with "FA9550" or "F49620" or "FA2386".

FA9550-13-1-0145

Principal Investigator Name

The full name of the principal investigator on the grant or contract.

John T. Foster

Program Manager

The AFOSR Program Manager currently assigned to the award

James Fillerup

Reporting Period Start Date

04/01/2013

Reporting Period End Date

03/31/2016

Abstract

Peridynamics is a nonlocal formulation of continuum mechanics in which forces are calculated as integral functions of displacement fields rather than spatial derivatives. The peridynamic model has major advantages over classical continuum mechanics when displacements are discontinuous, such as in the case of material failure. While multiple peridynamic material models capture the behavior of solid materials, not all structures are conveniently analyzed as solids. Finite Element Analysis often uses 1D and 2D elements to model thin features that would otherwise require a great number of 3D elements, but peridynamic thin features remain underdeveloped despite great interest in the engineering community. This work develops nonordinary state-based peridynamic models for the simulation of thin features. Beginning from an example nonordinary state-based model, lower dimensional peridynamic models of plates, beams, and shells are developed and validated against classical models. These peridynamic models are extended to incorporate brittle and plastic material failure, compounding the peridynamic advantages of discontinuity handling with the computational simplicity of reduced-dimension features. These models will allow peridynamic modeling of complex structures such as aircraft skin that may experience damage from internal forces or external impacts.

DISTRIBUTION A: Distribution approved for public release.

Distribution Statement

This is block 12 on the SF298 form.

Distribution A - Approved for Public Release

Explanation for Distribution Statement

If this is not approved for public release, please provide a short explanation. E.g., contains proprietary information.

SF298 Form

Please attach your [SF298](#) form. A blank SF298 can be found [here](#). Please do not password protect or secure the PDF. The maximum file size for an SF298 is 50MB.

[AFD-070820-035_final.pdf](#)

Upload the Report Document. File must be a PDF. Please do not password protect or secure the PDF. The maximum file size for the Report Document is 50MB.

[AFOSR_Final_Report.pdf](#)

Upload a Report Document, if any. The maximum file size for the Report Document is 50MB.

Archival Publications (published) during reporting period:

J.T. O'Grady and J.T. Foster. A meshfree method for bending and failure in non-ordinary peridynamic shells. Computational Mechanics, 57(6):921–929, June 2016. doi:10.1007/s00466-016-1269-z.

J.T. O'Grady and J.T. Foster. Peridynamic plates and flat shells: A non-ordinary state-based model. International Journal of Solids and Structures, 51(25–26):4572–4579, 2014. doi:10.1016/j.ijsolstr.2014.09.003.

J.T. O'Grady and J.T. Foster. Peridynamic beams: A non-ordinary state-based model. International Journal of Solids and Structures, 51(18):3177–3183, 2014. doi: 10.1016/j.ijsolstr.2014.05.014.

2. New discoveries, inventions, or patent disclosures:

Do you have any discoveries, inventions, or patent disclosures to report for this period?

No

Please describe and include any notable dates

Do you plan to pursue a claim for personal or organizational intellectual property?

Changes in research objectives (if any):

None

Change in AFOSR Program Manager, if any:

None

Extensions granted or milestones slipped, if any:

None

AFOSR LRIR Number

LRIR Title

Reporting Period

Laboratory Task Manager

Program Officer

Research Objectives

Technical Summary

Funding Summary by Cost Category (by FY, \$K)

	Starting FY	FY+1	FY+2
Salary			
Equipment/Facilities			
Supplies			
Total			

Report Document

Report Document - Text Analysis

Report Document - Text Analysis

Appendix Documents

2. Thank You

E-mail user

Jul 21, 2016 14:16:21 Success: Email Sent to: jtfoster@austin.utexas.edu